Centre Énergie Matériaux Télécommunications

NEAR-FIELD IMAGING VIA LOCALIZED SURFACE PLASMON RESONANCE ENHANCED GOLD PHOTOLUMINESCENCE

Par
Jiawei Zhang

Thèse présentée pour l'obtention du grade de
Philosophiae Doctor (Ph.D.)
en sciences de l'énergie et des matériaux (INRS-EMT)

Jury d'évaluation

Président du jury et examinateur interne	Prof. Shuhui Sun INRS-EMT, Canada
Examinateur externe	Prof. Eva Hemmer University of Ottawa, Canada
Examinateur externe	Prof. Dongfeng Xue Shenzhen Institute of Advanced Technology, Chinese Academy of Sciences, China
Directeur de recherche	Prof. Andreas Ruediger INRS-EMT, Canada

ACKNOWLEDGEMENTS

"The days that make us happy make us wise."

That's a quote from Poet Laureate, John Masefield, which came to mind as I'm sitting in front of the desk right now composing this acknowledgement for my thesis. I have always tried to imagine what it might feel like when I write the acknowledgements which signifies the soon to come ending of my PhD study, yet never have I ever thought it would be this much peace I'm bathing in right now. Looking back at this journey, I have encountered numerous people, come and go. I feel the necessity to highlight some of them, to put my gratitude into words.

First and foremost, I am, and will always be grateful to my supervisor, Prof. Andreas Ruediger, who gave me this precious opportunity. With his warmth in personality, sometimes weird wittiness, rigorous academic attitude, he has always been a beam of light with such brilliance shining upon and guiding me throughout my PhD study. Thanks to him, I have gained more confidence, challenged myself outside my comfort zone, achieved personal goals. Overall, he has made this journey possible and much less arduous. As an old Chinese saying goes, a teacher for day, a father for life. I will remember him with the utmost awe and respect, for now and ever.

I would also like to express my gratitude to my jury members, Prof. Shuhui Sun, Prof. Eva Hemmer and Prof. Dongfeng Xue, for their invested time and effort as the jury committee. In particular, I would like to express my most sincere gratitude to Prof. Dongfeng Xue, for recommending me to Andreas as a PhD candidate 6 years ago, as well as offering systematic training from his research group in Changchun Institute of Applied Chemistry, Chinese Academy of Sciences, which prepared me for the transition from an undergraduate student to a PhD candidate.

I would also like to thank all members of the Nanophotonics group, past and current. Especially Dr. Julien Plathier, with whom I learnt the complete operation process of TERS system; Dr. Gitanjali Kolhatkar, for all the scientific discussions as well as correcting my manuscripts; Dr. Azza Hadj Youssef, for being such a good colleague and friend, for helping me with the French translation for part of my thesis, and more importantly thanks a lot for your "magic" STO sample.

I would also like to thank my friends, Serge, Kasi and Wenbo, for making my life outside the lab vivid and entertaining, and always being there for me whenever and wherever. Our long walks, cups of bubble tea, nights of chats, trips to bars and restaurants, are some of the highlights of my life in Montréal.

Last but not the least, I would like to express my gratitude to my parents, Yan and Shouchen. My dearest mum and dad, your unconditional love has enabled me to become the person I am today. Thanks to you I have had the chance to catch a glimpse of the manifestation of true love. Regardless of my ups and downs, you have always been there. You are my shield, my wings my forever source of security. I love the two of you, even though I don't say it often enough. Thank you mum and dad for everything, big or small, important or trivial.

I am both proud and glad that I have chosen this journey. I have since long understood that there exists not the perfect choice. Emphasizing too much on the significance of the chosen journey drastically undermines the purpose of living. I could be doing a million different things in a million parallel universes. However, I have no regrets in the journey I have chosen, nor interests in other possibilities, the "I could'ves". I thus thank myself for acknowledging and accepting my mediocracy and limits with peace yet never stopped to aim higher, for thriving in a foreign land far away from home, for carrying on with the weight from the past and standing strong, for becoming ever more hard-working, resilient, righteous and prudent throughout this journey.

I am wiser today than when I first started this journey, because I have been happy. I have been happy because I'm blessed to having all of you in my life. For that I will forever be in debt, and from the deepest of my heart, I wish all of you all the best for your journeys in life.

RÉSUMÉ

Le développement rapide des nanosciences et des nanotechnologies a considérablement favorisé la compréhension ainsi que la conception et le contrôle précis des propriétés des matériaux à l'échelle nanométrique, ce qui conduit finalement au développement de nouveaux matériaux et dispositifs fonctionnels. L'un des principaux problèmes à résoudre dans ces domaines d'étude est la détection et la caractérisation des matériaux et de leurs propriétés à l'échelle nanométrique. Dans ce contexte, la spectroscopie Raman exaltée par effet de pointe (TERS), une nouvelle technique de caractérisation qui combine la sensibilité chimique de la spectroscopie Raman conventionnelle avec la haute résolution spatiale de la microscopie à sonde de balayage (SPM), a démontré sa capacité à obtenir la topographie et les informations spectrales correspondantes de divers types d'échantillons simultanément avec une sélectivité et une sensibilité élevées et une résolution spatiale bien inférieure à la limite de diffraction.

La nanoantenne, c'est-à-dire la pointe de balayage fonctionnalisée, est l'élément central du TERS, car c'est le principal composant utilisé pour surmonter la limite de diffraction en tant que source de l'amplification. Elle assure également l'exaltation du signal et détermine la résolution spatiale. La nanoantenne a donc été le centre d'intérêt de ces deux dernières décennies qui ont vu le TERS passer d'une technique réservée à un groupe de chercheurs hautement spécialisés à une technique disponible commercialisée. De nombreux progrès ont été réalisés dans l'identification des propriétés plasmoniques (et autres) des pointes TERS et une série de procédures ont vu le jour au fil du temps pour produire des pointes TERS plasmoniques avec une reproductibilité moyenne à bonne en or ou en argent. En pratique, la production de meilleures nanoantennes plasmoniques, la compréhension de leurs propriétés et leur évaluation de manière rapide et pratique sont autant d'étapes essentielles pour faire progresser les techniques d'imagerie plasmonique, y compris celle du TERS.

Dans la première partie de ce travail, j'ai développé une nouvelle recette pour la fabrication de pointes TERS en argent avec une faible contamination et une bonne reproductibilité en me basant sur la technique de gravure électrochimique. Cette nouvelle recette est nettement plus facile et plus rentable que les procédés de gravure conventionnels pour la fabrication de pointes d'argent actives TERS.

Dans la deuxième partie de ce travail, je me suis concentré sur l'étude du signal d'émission intrinsèque de la pointe en or, qui peut être attribué à la photoluminescence (PL) de l'or amplifiée par la résonance plasmonique de surface localisée (LSPR). J'ai développé une technique *in-situ* pour l'évaluation de la propriété plasmonique de la pointe Au TERS, qui s'est avérée fiable, efficace et qui peut être facilement adoptée dans toutes les mesures TERS indépendamment de la configuration du système ou du type de pointe Au utilisé. En particulier, étant donné que la courbe LSPR peut être extraite du signal de la pointe, sa position peut être utilisée pour l'imagerie réfractive en champ proche, car les changements de l'indice de réfraction effectif local près du sommet de la pointe induisent des changements détectables de la position LSPR. J'ai identifié une influence de la topographie de l'échantillon sur la position du LSPR. Avec les travaux précédents de notre groupe, nous avons démontré la dépendance entre la position du LSPR et l'indice de réfraction effectif, ce qui peut être adopté comme une nouvelle technique d'imagerie en champ proche.

Dans la troisième partie de ce travail, j'ai identifié que la composition locale et la topographie du matériau influencent également l'intensité du LSPR, et j'ai démontré expérimentalement que l'intensité du LSPR fournit également un contraste significatif pour l'imagerie en champ proche à haute résolution, ajoutant ainsi à l'instrumentation optique une véritable résolution nanométrique pour la science des surfaces.

Mots clés

Spectroscopie Raman exaltée par effet de pointe; microscopie en champ proche amplifiée par les plasmons, résonance de plasmon de surface localisée; luminescence de l’or; permittivité optique; indice de réfraction; imagerie en champ proche.

ABSTRACT

The rapid development in nanoscience and nanotechnology has significantly promoted the understanding as well as the design and precise control of the nanoscale material properties, and eventually leads to developing novel functional materials and devices. One of the primary issues in need to be addressed in such fields of study is the detection and characterization of material and its properties at the nanoscale. In this context, tip-enhanced Raman spectroscopy (TERS), a novel characterization technique which combines the chemical sensitivity of conventional Raman spectroscopy with the high spatial resolution of scanning probe microscopy (SPM), has demonstrated its capability to obtain topography and its corresponding spectral information from various types of samples simultaneously with high selectivity, sensitivity, and a spatial resolution far below diffraction limit.

The nanoantenna, i.e. the functionalized scanning tip, is the core element of TERS, as it is the main component which is used to overcome the diffraction limit as the source of the enhancement. It also provides the enhancement of the signal and also determines the spatial resolution. The nanoantenna has therefore been the center of interest over the past two decades that have seen TERS evolve from a niche technique reserved to a group of highly specialized researchers to a commercially available technique. A lot of progress has been achieved in the identification of the plasmonic (and additional) properties of TERS tips and while a series of procedures have emerged over time to produce TERS tips with fair to good reproducibility for plasmonic tips made of either gold or silver. In practice, producing better plasmonic nanoantennas, understanding their properties and assessing them in a fast and convenient way are all critical milestones in order to further advance plasmonic-enhanced imaging techniques including TERS.

In the first part of this work, I have developed a new recipe for silver TERS tip manufacturing with low contamination and good reproducibility by means of electrochemical etching. In comparison, this new recipe is significantly easier and more cost-efficient than conventional etching processes for the fabrication of TERS active silver tips.

In the second part of this work, I have focused on the study of an intrinsic gold tip emission signal, which can be assigned to the localized surface plasmon resonance (LSPR) enhanced Au photoluminescence (PL). I have developed an *in-situ* technique for the evaluation of Au TERS tip plasmonic property, which has been proven to be reliable, efficient and which can be readily adopted in any TERS measurements regardless of the system setup or the type of Au tip in use. In particular, given that the LSPR curve can be extracted from the tip signal, its position can be used for near-field refractive imaging, as changes in local effective refractive index near the tip apex induce detectable changes to the LSPR position. I have identified a sample topography influence on the LSPR position. Together with previous works from our group, we have demonstrated the dependence of LSPR position and effective refractive index, which can be adopted as a novel near-field imaging technique. In the third part of this work, I have identified that local material composition and topography also influence the LSPR intensity, and demonstrated experimentally that the LSPR intensity also provides meaningful contrast for high resolution near-field imaging thus adding to the optical instrumentation with true nanoscale resolution for surface science.

Keywords

Tip-enhanced Raman spectroscopy; Plasmon-enhanced near-field microscopy, Localized surface plasmon resonance; Gold luminescence; optical permittivity; refractive index; near-field Imaging

OBJECTIVES

1. Development of a new reproducible silver TERS tip fabrication process via electrochemical etching which does not rely on any additional divices (such as a cut-off circuit) to cope with the issue of over-etching.
2. Identifying an in-situ procedure to qualitatively assess gold TERS tip plasmonic properties through intrinsinc gold TERS tip signal (namely LSPR enhanced gold PL).
3. Development of physical near-field imaging in TERS configuration through intrinsinc gold TERS tip signal (namely LSPR enhanced gold PL), as well as identifying sample material composition and local topography influence on tip plasmonic properties such as plasmon position and intensity.

SOMMAIRE RÉCAPITULATIF

Imagerie en champ proche de la photoluminescence de l’or amplifiée par résonance de plasmon de surface localisée

1.1 La spectroscopie Raman

Les nanosciences et les nanotechnologies, comme leur nom l'indique, se concentrent principalement sur la synthèse, la caractérisation, l'étude et les applications des matériaux nanostructurés caractérisés par au moins une dimension de l'ordre du nanomètre (1-100 nm).[1] Il est largement reconnu que lorsque la taille d'un matériau diminue, ses propriétés chimiques, physiques, biologiques, etc. changent radicalement par rapport à celles des matériaux à l'échelle atomique (moléculaire) ou en vrac. En outre, l'effet de surface, l'effet quantique, etc. deviennent également plus importants dans ces systèmes à l'échelle nanométrique. Le développement des nanosciences et des nanotechnologies a jusqu'à présent favorisé la compréhension, la conception et le contrôle précis des propriétés des matériaux à l'échelle nanométrique, ce qui a permis de développer de nouveaux matériaux et dispositifs fonctionnels. Ces domaines de recherche, notamment la nanobiologie, la nano-optique, la nanoélectronique et la nanomécanique, ont suscité beaucoup d'intérêt et d'attention et ont déjà fait l'objet de nombreux travaux.

L'un des principaux problèmes à résoudre dans le cadre du développement rapide des nanosciences et des nanotechnologies est la détection et la caractérisation des matériaux et de leurs propriétés à l'échelle nanométrique. Les techniques de spectroscopie optique conventionnelles, telles que la spectroscopie Raman et la spectroscopie infrarouge, sont capables de détecter les spectres d'émission, d'absorption ou de diffusion des substances, et l'analyse des caractéristiques spectrales permet d'obtenir facilement des informations sur la structure et la dynamique moléculaire de l'échantillon mesuré. En outre, les techniques de spectroscopie optique conventionnelles sont sensibles et peuvent également être réalisées in situ. Elles bénéficient également d'une relative simplicité d'utilisation et présentent généralement peu de restrictions en ce qui concerne la préparation de l'échantillon et l'environnement de travail. Si l'on prend l'exemple de la spectroscopie Raman conventionnelle en champ lointain, elle est déjà devenue un outil courant de caractérisation au laboratoire et son application a été largement adoptée, tant sur le plan qualitatif que quantitatif, dans de nombreux domaines tels que l'industrie pharmaceutique, la géologie et la minéralogie, les matériaux en carbone, les semi-conducteurs, les sciences de la vie et bien d'autres encore.

Pour la diffusion Raman, le photon émis a une énergie différente $\mathrm{h}(\nu_0 \pm \Delta\nu)$ de celle du photon incident $\mathrm{h}\nu_0$. Dans le cas de la diffusion Raman Stokes, l'état final a une énergie inférieure de $\mathrm{h}(\nu_0 - \Delta\nu)$, un phonon est généré alors que dans le cas de la diffusion Raman Anti-Stokes, l'état final a une énergie supérieure $\mathrm{h}(\nu_0 + \Delta\nu)$, et un phonon est absorbé. Par conséquent, le décalage Raman, donné par la différence d'énergie entre l'état initial et l'état final, est déterminé par la structure et les propriétés du système de diffusion et est capable de refléter distinctement les différentes vibrations et rotations intrinsèques de la structure atomique de l'échantillon étudié. En d'autres termes, le décalage Raman est une "empreinte digitale" unique d'une structure moléculaire particulière. Les décalages Raman sont généralement donnés en unités proportionnelles à l'énergie par:

$$\Delta\nu = \frac{1}{\lambda_0} - \frac{1}{\lambda_{scatter}} \qquad 1$$

où λ_0 est la longueur d'onde de la lumière incidente et $\lambda_{scatter}$ est la longueur d'onde de la lumière Raman diffusée. La figure 1 est le diagramme de Jablonski, qui représente le niveau d'énergie du processus de diffusion Rayleigh, la diffusion Raman avec un décalage Stokes et la diffusion Raman avec un décalage anti-Stokes.

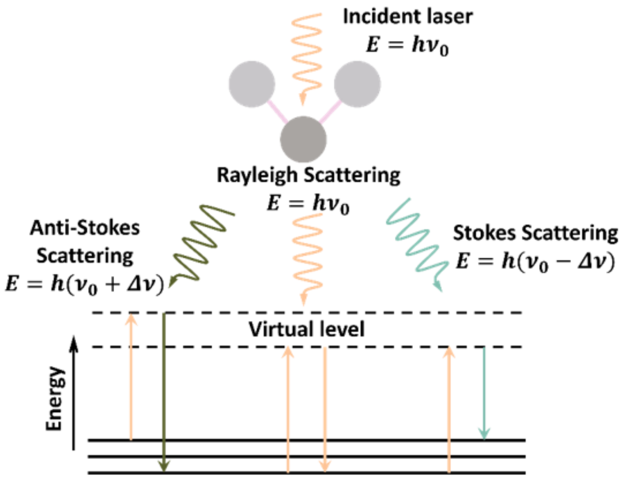

Figure 1: Diagramme de Jablonski du niveau d'énergie de la diffusion Rayleigh, la diffusion Raman avec un décalage Stokes et la diffusion Raman avec un décalage anti-Stokes.

Cependant, la résolution spatiale de la spectroscopie optique conventionnelle, telle que la spectroscopie Raman, est fortement limitée par la limite de diffraction optique, ce qui rend difficile, voire impossible dans certains cas, de répondre aux besoins de détection et de caractérisation à l'échelle nanométrique. La diffraction de la lumière se produit lorsqu'elle est diffusée par un objet dont la taille est inférieure ou comparable à celle de la longueur d'onde de la lumière incidente. Au cours du processus de diffusion, chaque point de la diffusion agit comme un nouvel émetteur de lumière, créant ainsi un motif d'interférence dans le champ lointain. Dans le cas du processus de diffraction, une figure de diffraction avec des maxima et des minima d'interférence est générée dans le champ lointain en raison du déphasage relatif. Pour la figure de diffraction générée par une source lumineuse ponctuelle, la région brillante au centre (maximum) ainsi que le premier anneau concentrique de plus faible intensité (minimum) qui l'entoure sont appelés le disque d'Airy. La diffraction de la lumière régit la limite de résolution de tous les dispositifs optiques, qui est définie comme une distance minimale r à laquelle deux points de diffusion peuvent être facilement distingués. Cette limite optique peut être estimée par les critères d'Abbe ou de Rayleigh et est donnée par:[2,3]

$$r \simeq 0.61\frac{\lambda}{NA} \tag{2}$$

où NA est l'ouverture numérique de l'objectif. r peut être approximé en pratique à 0,61λ. Comme le montre la figure 2, deux points ne sont optiquement séparés que si l'intensité qui se chevauche n'est pas supérieure à 74% du maximum (Imax).[4]

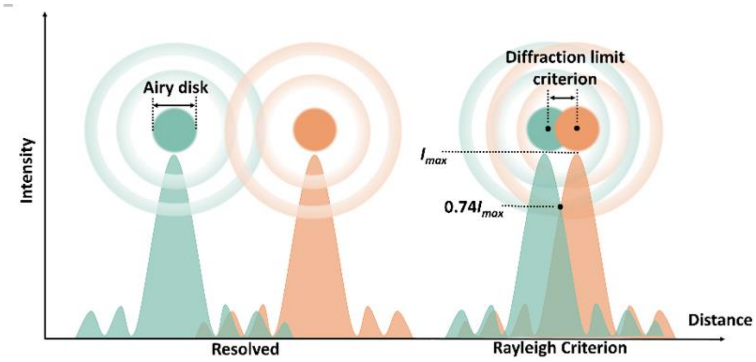

Figure 2: Diagrammes d'Airy de deux sources lumineuses ponctuelles successives, ils sont séparées pour finir par être optiquement résolues jusqu'à atteindre le critère de Rayleigh pour la limite de diffraction.

Afin d'améliorer la résolution optique limitée par la limite de diffraction, et au lieu d'augmenter de la NA, il est possible d'adopter des sources lumineuses de plus courte longueur d'onde. Par exemple, les faisceaux d'électrons, les faisceaux d'ions et les rayons X dont la longueur d'onde est beaucoup plus courte que celle de la lumière visible et qui ont été utilisés pour la détection et la caractérisation de divers systèmes d'échantillons. Les techniques correspondantes comprennent la microscopie électronique à balayage (MEB), la microscopie électronique à transmission (MET), la spectroscopie de perte d'énergie des électrons (EELS) et d'autres méthodes. Cependant, par rapport aux techniques classiques de spectroscopie optique, les processus physiques des méthodes citées dessus sont relativement compliqués, les techniques basées sur les électrons nécessitent généralement des conditions de vide et les informations obtenues sont souvent difficiles à analyser sans une connaissance préalable de l'échantillon étudié. De plus, en raison de la diminution de la longueur d'onde incidente qui entraîne un apport d'énergie plus important, l'environnement opérationnel ainsi que la préparation de l'échantillon deviennent plus exigeants, et les échantillons sont plus susceptibles d'être endommagés pendant les mesures.

1.2 L'optique en champ proche

Dans ce contexte, le concept d'optique en champ proche a été introduit pour faire face aux problèmes mentionnés dans le paragraphe précédent. Avec des recherches plus poussées, il a été démontré que le critère de Rayleigh n'est valable que pour le champ optique lointain, où la distance d entre les objets mesurés est beaucoup plus grande que la longueur d'onde incidente λ. Lorsque d commence à diminuer, nous atteignons une région où l'approximation du champ lointain n'est plus valable, et où les ondes EM évanescentes deviennent plus dominantes dans leur contribution au champ global. Pour un émetteur à l'échelle nanométrique (ou une antenne optique), la transition du champ EM du champ lointain au champ proche est illustrée à la figure 3.[5]

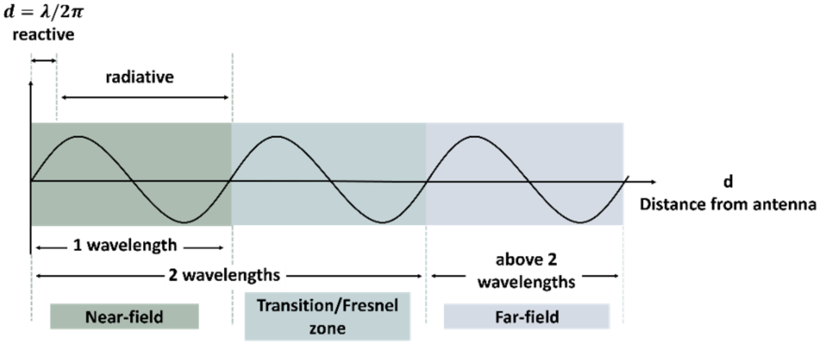

Figure 3: Transition du champ électromagnétique EM du champ lointain au champ proche en fonction de la distance d à une nano-antenne.

En 1984, Pohl et al. et Lewis et al. ont atteint indépendamment une résolution de détection optique au-delà de la limite de diffraction dans le domaine visible, ouvrant ainsi un nouveau chapitre dans la recherche sur l'optique en champ proche.[6,7] Ces techniques optiques ont été appelées "microscopie optique à balayage en champ proche" (SNOM) ou microscopie optique à balayage en champ proche (NSOM). Actuellement, deux types de SNOM sont le plus souvent adoptés en fonction des types de sondes (antenne) utilisés. En mode ouverture (aperture-

SNOM), également appelé collection SNOM (c-SNOM), une fibre optique pointue est utilisée, tandis que le SNOM sans ouverture (aSNOM), également appelé scattering-SNOM, implique l'utilisation d'une sonde ultra-pointue. En particulier, l'aSNOM permet de surmonter le dilemme technique de l'équilibre entre la transmission de la lumière et la taille de l'ouverture afin de maximiser la résolution spatiale dans le cas de l'aperture-SNOM. Actuellement, l'aSNOM permet une haute résolution spatiale bien inférieure à 10 nm.[8] Cependant, l'intensité du signal de champ proche diffusé par la sonde est extrêmement faible. Il peut également être supplanté par un signal de fond relativement fort. Par conséquent, l'un des principaux défis de l'aSNOM est de détecter efficacement et d'extraire ensuite les informations de champ proche intégrées dans les signaux détectés.[9] Jusqu'à présent, les applications actuelles de l'aSNOM sont généralement dédiées à l'étude de la spectroscopie Raman dans le domaine visible dans lequel les propriétés plasmoniques jouent un rôle important, comme la spectroscopie Raman en surface (SERS) et la spectroscopie Raman exaltée par effet de pointe (TERS).

1.3 Spectroscopie Raman exaltée par effet de pointe

La TERS est une nouvelle technique de caractérisation qui combine la sensibilité chimique de la spectroscopie Raman classique avec la haute résolution spatiale de la SPM. Dans une expérience TERS typique, une nanoparticule plasmonique unique a été utilisée pour le renforcement du champ E en tant qu'antenne optique.[10] Un plasmon est une quasi-particule qui représente la quantification des oscillations du plasma. En d'autres termes, il s'agit des oscillations collectives de la densité du gaz d'électrons libres. Les plasmons se trouvent le plus souvent dans les métaux, car les électrons y sont fortement délocalisés. À l'intérieur des métaux, les plasmons sont appelés plasmons massifs (figure 4 (a)). Les plasmons qui sont confinés à une interface entre le métal et le diélectrique sont appelés plasmons de surface (SP). L'importance des SP en nanophotonique réside dans leur capacité à se coupler avec des photons incidents dans certaines conditions (qui seront discutées en détail dans les sections suivantes), ce qui formera des polaritons de plasmons de surface (SPP) qui se propagent (figure 4 (b)). En principe, les SPP sont des champs électromagnétiques évanescents améliorés qui se propagent le long de l'interface métal-diélectrique et qui diminuent exponentiellement de la frontière vers l'environnement.[11,12] Lorsqu'une nanoparticule de dimension inférieure à la longueur d'onde couple ses oscillations électroniques de surface avec des photons incidents pour former des plasmons de surface, au lieu de se propager comme dans le cas des SPP, ces SP sont fortement localisés et liés à la surface de la nanoparticule, connus sous le nom de plasmons de surface localisés (LSP) (figure 4 (c)). Lorsque les photons incidents atteignent la fréquence de résonance plasmonique de la nanoparticule, l'oscillation cohérente des électrons libres devient en phase avec le champ EM diffusé. Dans cette condition, une résonance de plasmons de surface localisée (LSPR), telle qu'illustrée à la figure 5, est générée et l'amélioration du champ électromagnétique atteint son maximum.[13]

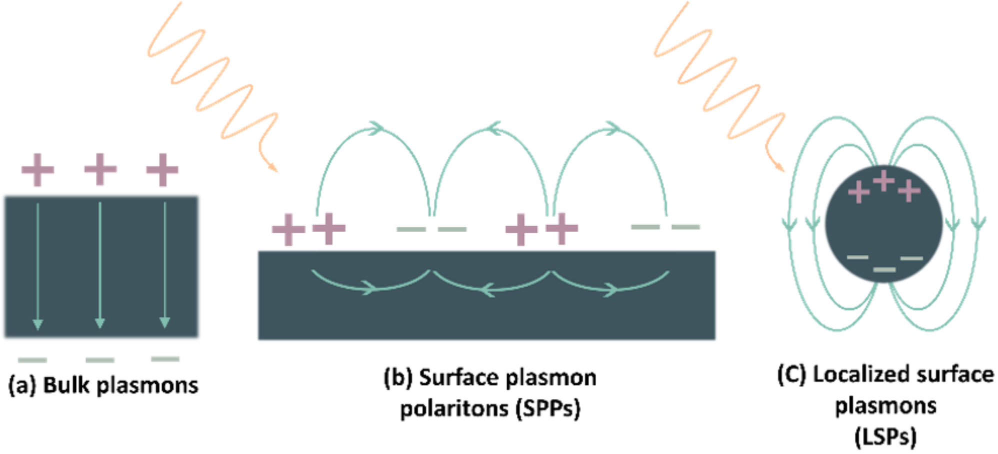

Figure 4: (a) plasmon massif à l'intérieur du métal (b) polaritons de plasmon de surface (SPP) qui se propageant le long de l'interface métal-diélectrique et (c) plasmons de surface localisés (LSPR) confinés au voisinage immédiat d'une nanoparticule métallique de dimension inférieure à la longueur d'onde.

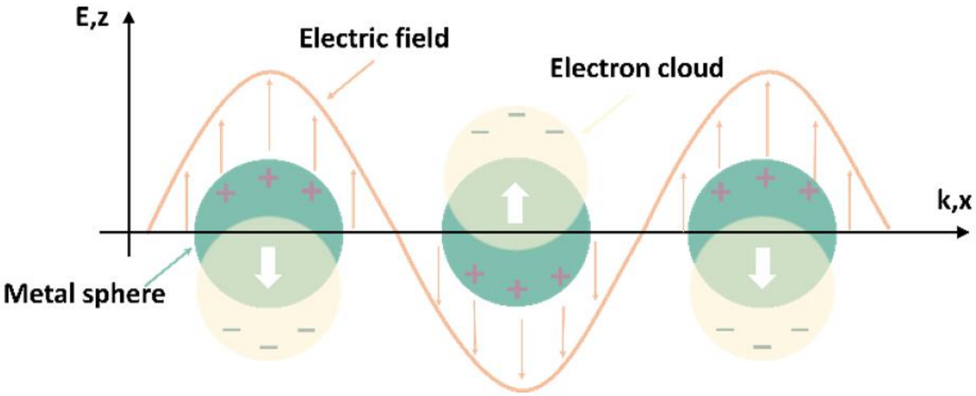

Figure 5: Illustration de l'excitation du LSP sur des nanosphères métalliques par un champ électrique externe. Le déplacement du nuage d'électrons libres entraîne un moment dipolaire.

Comme nous pouvons le voir sur la figure 5, le champ E externe conduit à un déplacement du nuage d'électrons libres de la sphère métallique, ce qui entraîne un moment dipolaire induit $\vec{p}$ donné par :

$$\vec{p} = \vec{E} \cdot \alpha \qquad 3$$

Dans laquelle $\alpha(\lambda)$ est la polarisabilité dipolaire dans l'approche quasistatique:[14]

$$\alpha = 4\pi\varepsilon_0 r^3 \frac{\varepsilon_{sphere} - \varepsilon_d}{\varepsilon_{sphere} + 2\varepsilon_d} \tag{4}$$

avec ε_{sphere} la permittivité relative de la sphère métallique, ε_d la permittivité relative du milieu diélectrique. Dans le domaine optique, ε_{sphere} est approximé par le modèle de Drude introduit dans les sections précédentes comme:

$$\varepsilon_{sphere} = \varepsilon(\omega) = 1 - \frac{\omega_p^2}{\omega^2 + i\Gamma\omega} \tag{5}$$

Dans l'équation, $\frac{\varepsilon_{sphere} - \varepsilon_d}{\varepsilon_{sphere} + 2\varepsilon_d}$ est appelé la réponse optique, ou facteur g, qui est une mesure de l'éxaltation du champ E. La résonance de la nanosphère métallique se situe à $\omega_{\text{resonance}}$ lorsque $\frac{\varepsilon_{sphere} - \varepsilon_d}{\varepsilon_{sphere} + 2\varepsilon_d}$ est maximisé, c'est-à-dire lorsque :

$$\varepsilon_{sphere} + 2\varepsilon_d = 0 \tag{6}$$

Pour les particules métalliques sphéroïdales, la résonance ω_ peut être déterminée à partir de:

$$\omega_{\text{resonance}} = \sqrt{\omega_p^2 \Big/ 1 + \left(\frac{l+1}{1}\varepsilon_d\right)} \tag{7}$$

Dans lequel l est un facteur de forme allant de 1 pour les sphères et ∞ pour les aiguilles.[15,16] Par exemple, dans le cas où le milieu environnant est le vide dont ε_d est égal à 1, la $\omega_{\text{resonance}}$ d'une particule métallique sphérique est :

$$\omega_{\text{resonance}} = \sqrt{\frac{\omega_p^2}{3}} \tag{8}$$

Lorsqu'une particule métallique (quelle que soit sa forme) est excitée par la lumière incidente à ω_$_{\text{résonance}}$, l'oscillation collective des électrons libres qui en résulte est connue sous le nom la résonance de plasmon de surface localisée (RPSL).[17] L'excitation de la RPSL est la clé de l'amélioration significative des champs électromagnétiques, qui conduit à la diffusion Raman de surface (SERS), à la diffusion Raman exaltée par effet de pointe (TERS) ainsi qu'à diverses autres techniques de spectroscopie en champ proche induit par plasmons.[18,19] En outre, le potentiel des nanoparticules d'or et d'argent en tant que capteurs de petit volume, ultra-sensibles et sans marqueur basés sur la SERS a attiré beaucoup d’attention dans des études récentes, en particulier dans le domaine de la biodétection.

2 Évaluation des propriétés plasmoniques de la pointe TERS

Au cours d'une expérience typique de TERS avec des pointes en or qui sont le plus souvent choisies pour leur stabilité chimique, un faisceau laser d'une certaine longueur d'onde correspondant au LSPR attendu est focalisé près de l'apex d'une pointe, qui présente un spectre détectable qui lui est propre; un spectre typique enregistré sur une pointe en or est illustré à la figure 6. Le nombre d'onde auquel cette courbe de forme lorentzienne atteint son maximum est appelé position du pic.[20-24] Le spectre observé du signal de la pointe résulte de deux contributions majeures: la première étant la photoluminescence de la pointe en or, qui est une propriété intrinsèque de l'or pouvant être attribuée aux transitions d-sp inter-bandes de l'or,[25] et la seconde étant la résonance de plasmon de surface localisée (LSPR) étant donné qu'elle est excitée par le laser incident. La RPLS renforce à son tour le PL de l'or, ce qui conduit à un PL de la pointe de l'or renforcé par la RPLS, qui est le signal de la pointe que nous détectons pendant l'expérience. Au cours d'une expérience TERS typique où une pointe d'or est utilisée comme nanoantenne, le laser incident est focalisé à l'apex de la pointe afin de générer la LSPR et de créer un signal de champ proche optique. Lorsque le LSPR est induit au sommet de la pointe, avant d'atterrir sur l'échantillon étudié, un signal de pointe est détectable dans le spectromètre. Ce signal est le PL de l'or amplifié par la LSPR, et a la forme d'une large courbe Lorentzienne.

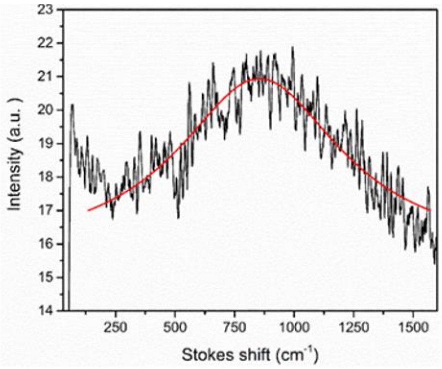

Figure 6: Signal typique d'une pointe en or dans une expérience TERS (noir) ajusté avec par une fonction Lorentzienne (rouge)

Il convient de noter que le PL de l'or est indépendant de la forme ou de la taille de la pointe, ce qui le rend valable pour les pointes TERS en or à l'échelle mondiale, étant donné que le rayon exact de la pointe n'est pas connu pendant une mesure TERS. En d'autres termes, pour tout changement dans le PL de la pointe en or exalté par le LSPR, le signal de la pointe, est principalement attribué aux variations du plasmon telles que les changements d'intensité, le déplacement de la position du plasmon, etc. Ainsi, l'étude du signal de la pointe d'or in situ pendant une mesure TERS permet d'explorer sa propriété plasmonique.

L'élément central du TERS est incontestablement la pointe.[26] En plus d'être la source d'amplification des signaux Raman, elle détermine également la résolution spatiale maximale qui peut être obtenue. En tant que tel, le défi le plus important du TERS est l'évaluation des propriétés plasmoniques de la pointe qui se manifestent à l'échelle moléculaire dans le champ proche optique.[27] Dans ce contexte, des techniques de dépistage précoce permettant de distinguer les pointes plasmoniques des pointes non plasmoniques pour la longueur d'onde considérée permettraient de gagner énormément de temps.

Nous présentons ici une approche facile in situ pour évaluer les propriétés plasmoniques de pointes TERS en or sans avoir besoin d'interaction avec l'échantillon, ce qui peut être facilement réalisé in situ en préparation d'une expérience TERS. Cette approche est réalisée par l'étude du PL de l'or exalté par LSPR de la pointe TERS en or en extractant la courbe plasmonique du signal de la pointe après l'alignement pointe-laser.

Nous prenons l'exemple de six pointes en or, qui ont été utilisées pour les mesures TERS et qui se sont révélées non plasmoniques (pointe (a) et (b)), moyennement plasmoniques (pointe (c) et (d)) et hautement plasmoniques (pointe (c) et (f)). Chaque spectre a été obtenu avec un temps d'acquisition de 1s au " point chaud " des pointes (Figure 7), obtenu suite au balayage du focus du laser dans un plan de 10 x 10 microns contenant l'apex de la pointe (Figure 7). Nous utilisons ensuite le spectre le plus intense obtenu à proximité de la pointe pour l'ajuster avec la fonction Lorentzienne, obtenant les résultats montrés ci-dessous:

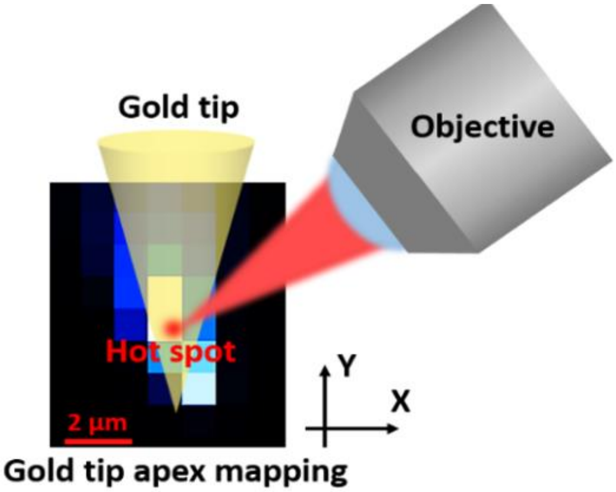

Figure 7: Cartographie de l'apex de la pointe en or dans le plan XY, les spectres ont été choisis au point de plus forte intensité, appelé " point chaud ".

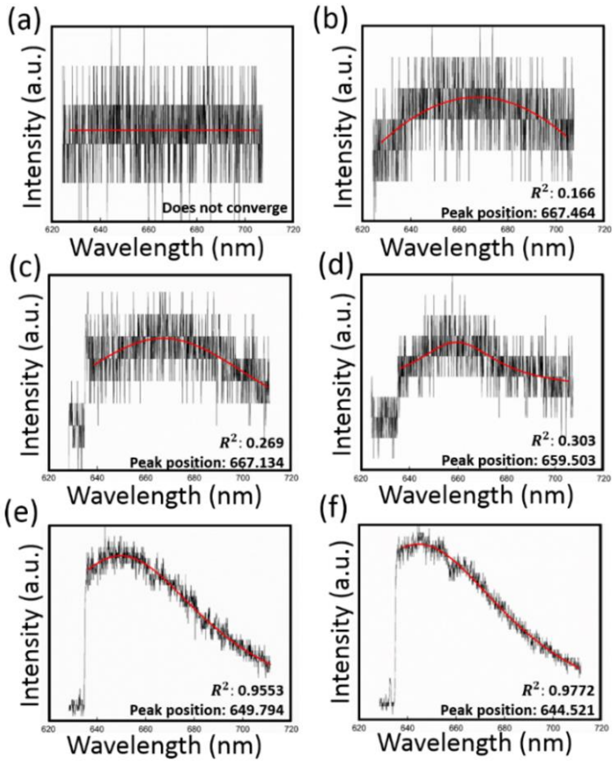

Figure 8: Signaux de pointe avec un temps d'acquisition de 1 s (noir) et ajustement par la fonction Lorentzienne (rouge) de: (a) (b) deux pointes non plasmoniques, (c) (d) deux pointes moyennement plasmoniques et (e) (f) deux pointes hautement plasmoniques avec les résultats d'ajustement R2 et la position du pic respectés.

On peut observer sur la Figure 8 que plus la pointe est plasmonique (de la pointe (f) à la pointe (a)), plus le rapport signal/bruit est élevé ainsi que le R^2 pour l'ajustement Lorentzien.

Cette procédure peut être adoptée comme une évaluation facile in situ de la propriété plasmonique de la pointe TERS en or. Après l'alignement de la pointe et du laser, où le point focal est placé sur le "point chaud" près de l'apex de la pointe, en ajustant le signal de la pointe (qui peut être obtenu avec un temps d'acquisition aussi court que 1 s) avec la fonction de Lorentz, nous pouvons identifier si la pointe se qualifie pour une utilisation ultérieure à partir de l’analyse du rapport signal/bruit et de la valeur R^2. Un R^2 proche de 1 implique une faible déviation de données expérimentales par rapport à l'ajustement, ce qui signifie une propriété plasmonique élevée de la pointe étudiée, et donc une plus grande probabilité d'obtenir une amplification du champ proche de l'échantillon étudié. D'autre part, les pointes dont la valeur R^2 est inférieure à 0,2 peuvent être considérées comme non plasmoniques et donc inappropriées pour les mesures TERS, soit en raison d'une forme inappropriée ou de contaminations sur la surface de la pointe, qui nécessitent un traitement supplémentaire (tel qu'un nettoyage au plasma, etc.) si l'on souhaite les utiliser pour effectuer des mesures TERS. Les pointes dont la valeur R^2 se situe entre ces deux valeurs valent tout de même la peine d'être essayées pour l'imagerie, car des travaux antérieurs ont démontré que de telles pointes peuvent encore être utilisées pour imager les changements locaux d'indice de réfraction avec une résolution aussi faible que 10 nm, même si elles ne peuvent pas être utilisées pour l'amplification des signaux Raman.[22] L'avantage de cette procédure est qu'il s'agit d'un processus in situ complet qui n'est pas limité par les configurations TERS ni par le type de pointe en or utilisé, car le signal de la pointe, ou le PL exalté par LSPR, est une propriété intrinsèque de l'or. L'évaluation préliminaire de la propriété plasmonique de la pointe est assez simple, ne nécessite pas d'échantillon de référence et peut être facilement adaptée à la routine d'une mesure TERS typique.

3 Étude de l'influence de la topographie de l'échantillon sur la position du LSPR

Dans une gamme spectrale de 480-800 nm, une approximation linéaire de la permittivité de l'or en fonction de la longueur d'onde peut être exprimée par :[20,23,28]

$$\varepsilon_r = -0.07\lambda + 32 \qquad 9$$

où ε_r est la partie réelle de la permittivité de l'or et λ la longueur d'onde (nm). Dans des conditions de résonance, la permittivité est alors corrélée à l'indice de réfraction effectif du milieu environnant au voisinage immédiat de l'apex de la pointe, comme suit:[29]

$$\varepsilon_r = -\,2\,n^2 \qquad 10$$

où *n* est l'indice de réfraction effectif de l’environnement de la pointe. Ainsi, à partir des deux équations mentionnées en haut, nous arrivons à la conclusion que, pendant une expérience TERS, la position de la luminescence de la pointe d'or amplifiée par le LSPR (signal détecté de la pointe) dépend de l'indice de réfraction effectif.

Pour évaluer cette influence de la topographie, nous imagerons la position du LSPR sur des nanostructures de titanate de strontium ($SrTiO_3$) chimiquement homogènes déposées sur un substrat de MgO (100) platinisé. Ces mesures sont réalisées à l'aide d'une pointe en or via aSNOM en configuration TERS. La topographie de l'échantillon étudié est représentée sur la Fig. 9 (a). La Fig. 9 (b) représente la cartographie à haute résolution de la position LSPR de la luminescence exaltée de l'or de la topographie de surface correspondante avec une résolution spatiale de l'ordre de 10 nm, ce qui est bien en dessous de la limite de diffraction. La carte obtenue est obtenue en enregistrant un spectre de la luminescence d'or exaltée par LSPR à chaque pixel et ajusté avec une équation de Lorentz.

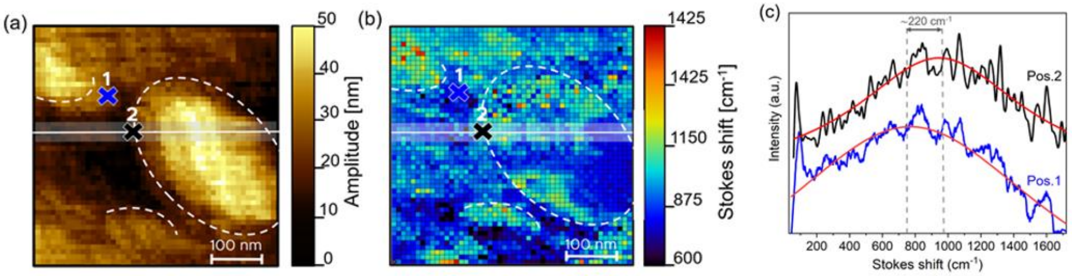

Figure 9: (a) Image topographique de 500 × 500 nm2 des nanostructures de SrTiO3, (b) Cartographie haute résolution de la position du LSPR sur les nanostructures de SrTiO3 déposées sur un substrat platinisé. Les lignes blanches correspondent aux zones sur lesquelles les lignes de profil ont été mesurées. Le temps d'acquisition pour la mesure de chaque spectre est de 1 s et (c) Spectres typiques du signal de la pointe en or acquis sur une surface plane (Pos. 1) et marche (Pos. 2) et ajustés avec la fonction Lorentzienne (ligne rouge).

La position LSPR correspond au nombre d'onde pour lequel cette courbe de forme lorentzienne atteint son maximum. La position LSPR est liée à la permittivité effective du milieu, composé d'air et de $SrTiO_3$ dans notre cas. La Fig. 9 (c) montre le signal typique de la pointe d'or ajusté par l'équation de Lorentz à deux positions différentes de l’échantillon: lorsque la pointe se déplace d'une surface plane (région bleu foncé, Pos. 1 et sur une marche (région bleu clair, Pos. 2 comme illustré dans la Fig. 9 (b). Nous observons un décalage vers le rouge de la position du LSPR lorsque la pointe passe de la position 1 à la position 2, en raison du changement de la distribution de la permittivité entourant la pointe en or. De plus, nous remarquons une forte corrélation entre la topographie de l'échantillon et la position du LSPR. Ces changements ne peuvent pas être expliqués par un changement dans la composition du matériau. La distribution de la position du LSPR varie avec la topographie et dépend fortement de l'environnement de la pointe et en particulier de la fraction volumique de l'air par rapport au $SrTiO_3$ au voisinage immédiat de l'apex de la pointe.

4 Étude de l'influence de la topographie de l'échantillon et de la composition du matériau sur l'intensité du LSPR

En TERS, l'intensité du signal suit la règle de la 4ème puissance de Raman.30,31 Le facteur d'amplification global (G (ω)) est donné par:[21,32]

$$G(\omega) = 5|1 + 2g(\omega_0)|^2|1 + 2g(\omega)|^2 \qquad 11$$

où ω_0 et ω étant respectivement les fréquences des photons incidents et émis.

Lorsque l'apex de la pointe est considéré comme sphérique, le facteur *g* est donné par [21,32]

$$g = \frac{\varepsilon_{metal}(\omega, r) - \varepsilon_{environment}}{\varepsilon_{metal}(\omega, r) + 2\,\varepsilon_{environment}} \tag{12}$$

où ε_{metal} est la permittivité de la particule métallique et $\varepsilon_{environnement}$ la permittivité du milieu. Cette permittivité est généralement considérée comme homogène, ce qui devient invalide lorsque la pointe s'approche de la surface. Ainsi, la permittivité du matériau est remplacée par une valeur effective qui prend en compte la contribution géométrique dans l'environnement diélectrique entourant la pointe.

Nous avons imagé la luminescence de la pointe d'or amplifiée par LSPR au-dessus de nanoîlots de titanate de strontium ($SrTiO_3$) déposés sur des substrats d'oxyde de magnésium platinisé (100) (Pt/MgO (100)). La figure 10 illustre la topographie de l'échantillon avec la carte d'intensité du signal de la pointe correspondante. Les nano-zones de $SrTiO_3$ peuvent être identifiées sur la carte d'intensité (indiquée par la zone à l'intérieur de l'ellipse en pointillés blancs), et elle ne représente que les variations d'intensité du signal de la pointe en or. Des variations significatives d'intensité à différents endroits de l'échantillon peuvent être observées.

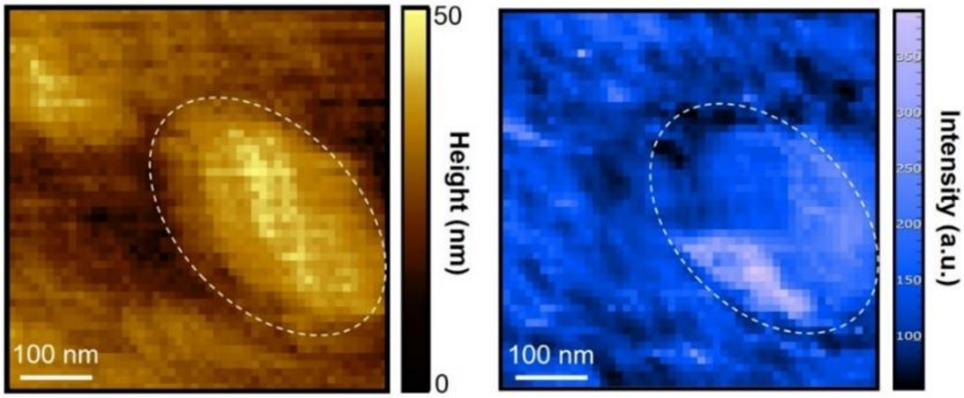

Figure 10: Topographie des nanoîlots de $SrTiO_3$ déposés sur du Pt polycristallin mesurée par la microscopie à force atomique (AFM) (à gauche) et cartographie de l'intensité du signal de la pointe (à droite), la zone indiquée (ligne pointillée) identifie un nanoîlot de $SrTiO_3$. Les deux images ont été enregistrées simultanément.

Pour vérifier l'influence du matériau de l'échantillon sur l'intensité du LSPR, nous étudions l'intensité du signal de la pointe en or à deux positions différentes sur la surface de l'échantillon comme illustré dans la Figure 11: la première est située au-dessus du nanoîlot de $SrTiO_3$ et la seconde, sur le substrat de Pt.

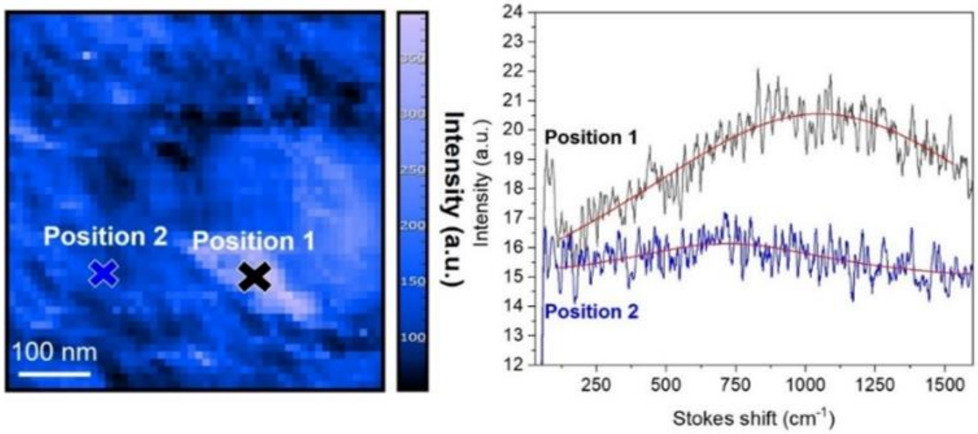

Figure 11: Carte d'intensité du signal de la pointe (à gauche), identifiant deux positions: la position 1 (au sommet d'un nanoîlot de $SrTiO_3$) et la position 2 (au sommet du substrat de Pt). Émission de l'or (noir et bleu) et ajustement numérique avec une fonction Lorentzienne (rouge). La position 1 présente une intensité plus élevée et un décalage vers le rouge par rapport à la position 2.

La figure 11 révèle que lorsque la pointe se trouve au-dessus du nanoîlot de $SrTiO_3$, l'intensité du signal de la pointe est visiblement plus élevée que celle obtenue lorsque la pointe se trouve sur le substrat de Pt, ce qui indique une augmentation de l'intensité du LSPR sur la nanostructure. Selon les équations 1 et 2, ce changement dans l'intensité du LSPR pourrait être dû à une augmentation de la permittivité effective lorsque la pointe passe de la région Pt au nanoîlot $SrTiO_3$. Dans nos conditions expérimentales, la permittivité relative du Pt est négative, donc beaucoup plus petite que celle du $SrTiO_3$. Cette différence de permittivité relative conduit aux changements observés dans l'intensité du LSPR.

Pour vérifier l'influence de la topographie de l'échantillon sur la variation de l'intensité du LSPR, nous nous concentrons sur les signaux de la pointe en or détectés sur le nanoîlot de $SrTiO_3$ comme présenté dans la Figure 12, où aucun changement de composition n'est attendu.

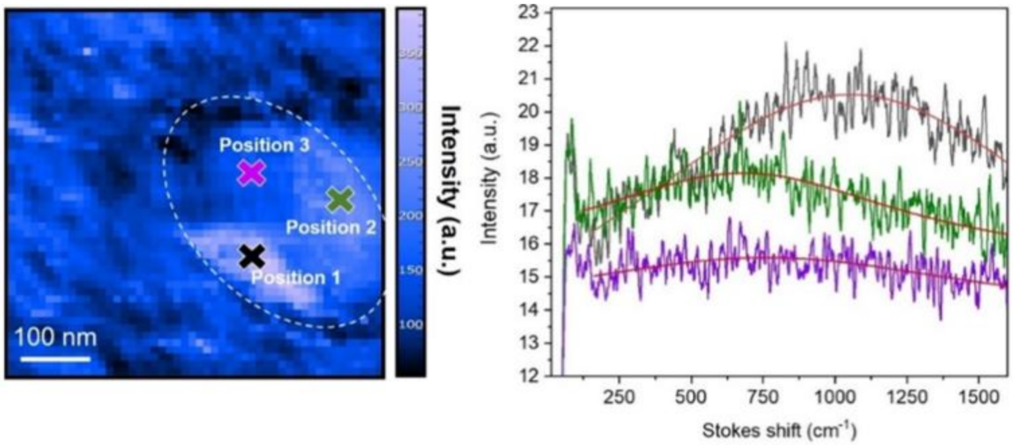

Figure 12: Carte d'intensité du signal de la pointe (à gauche), identifiant trois positions sur le sommet du nanoîlot de $SrTiO_3$. Émission de l'or (noir, vert et violet) et ajustement numérique avec une fonction Lorentzienne (rouge).

Comme nous pouvons le voir sur la Figure 12, lorsque la pointe scanne au-dessus d'un nanoîlot de $SrTiO_3$, des variations significatives de l'intensité du signal de la pointe sont observées et attribuées à une influence de la topographie, étant donné que les trois points ont été choisis dans différentes zones au-dessus du nanoîlot de $SrTiO_3$ avec une topographie variée. Lorsque la topographie locale à proximité de l'apex de la pointe varie, le rapport volumique entre le $SrTiO_3$ et l'air varie également, ce qui entraîne un changement de la permittivité effective. Cela se traduit par un changement dans l'intensité du signal de la pointe.

5 Conclusions

Les travaux précédents de notre groupe ont établi un modèle pour le signal intrinsèque de la pointe en or, qui peut être attribué à la PL Au amplifié par la LSPR. Sur la base de ce modèle, nous pouvons retrouver la courbe approximative du LSPR. J'ai développé une technique in situ pour l'évaluation des propriétés plasmoniques de la pointe TERS avec un processus d'ajustement simple. Cette technique est fiable, efficace et peut être facilement adoptée dans toutes les mesures TERS, quelle que soit la configuration du système ou le type de pointe en or utilisé. Étant donné que ce processus d'évaluation peut être réalisé à un stade très précoce d'une expérience TERS, nous pouvons rapidement déterminer si la pointe est très plasmonique, ce qui la rend extrêmement prometteuse pour l'amplification des signaux Raman de l'échantillon étudié, ou moyennement plasmonique, ce qui en fait un candidat pour d'autres types d'imagerie en champ proche qui ne dépendent pas fortement de l'exaltation du TERS, ou non plasmonique, ce qui signifie que la pointe doit être jetée ou traitée davantage (nettoyage, etc.).

En outre, étant donné que la courbe LSPR peut être extraite du signal de la pointe, sa position peut être utilisée pour l'imagerie réfractive en champ proche, car les changements de l'indice de réfraction effectif local près de l'apex de la pointe induisent des changements détectables de la position LSPR. Dans mon travail, j'ai identifié une influence de la topographie de l'échantillon sur la position du LSPR. Avec les travaux précédents de notre groupe, nous avons démontré la dépendance entre la position du LSPR et l'indice de réfraction effectif, qui varie à la fois avec la composition du matériau et la topographie.

Enfin, j'ai démontré que la composition du matériau et la topographie n'affectent pas seulement la position du LSPR mais aussi son intensité (Figure 13). L'intensité de la LSPR seule peut être utilisée pour l'imagerie en champ proche. Étant donné que le PL intrinsèque de l'or est constant, l'intensité du signal de la pointe peut être utilisée directement pour l'imagerie en champ proche. Par rapport à l'imagerie en champ proche via la position du LSPR, aucun processus d'ajustement n'est nécessaire, ce qui réduit les erreurs introduites pendant le processus d'ajustement.

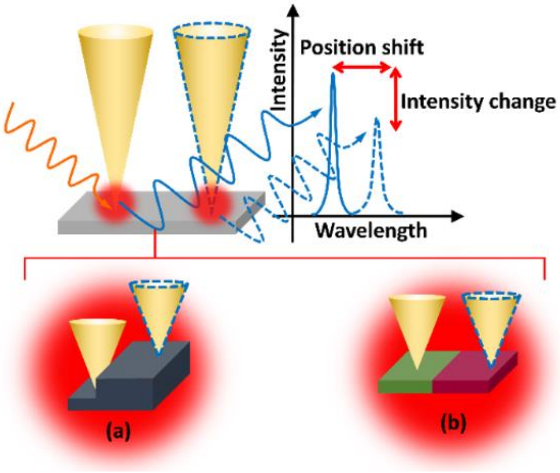

Figure 13: influence de la topographie (a) et de la composition (b) du matériau sur la position et l'intensité du LSPR.

En conclusion, mon travail souligne l'importance de prendre en considération la composition du matériau ainsi que la topographie lors d'une expérience TERS typique, et identifie leur influence sur le comportement plasmonique de la pointe. Cela nous rapproche de la résolution du problème de la compréhension et de la corrélation des intensités relatives des signaux TERS, qui constitue un défi majeur pour la communauté depuis des décennies. En outre, j'ai également étudié en détail le signal intrinsèque de la pointe, en l'identifiant comme un outil précieux pour l’analyse précoce des pointes TERS plasmoniques, ainsi que pour établir l'imagerie en champ proche via la position LSPR extraite ou son intensité. J'ai ainsi prouvé la possibilité d'obtenir des informations précieuses et abondantes à partir du signal de la pointe, qui a toujours été considéré comme un arrière-plan parasite par la communauté scientifique.

Bibliographie

1 T. D. Thangadurai, N. Manjubaashimi, S. Thomas and H. J. Maria, *Nanostructured materials*, Springer Nature Switzerland.

2 E. Abbe, Beiträge zur Theorie des Mikroskops und der mikroskopischen Wahrnehmung: I. Die Construction von Mikroskopen auf Grund der Theorie, *Arch. für mikroskopische Anat.*, 1873, **9**, 413–418.

3 Rayleigh, Investigations in optics, with special reference to the spectroscope, *London, Edinburgh, Dublin Philos. Mag. J. Sci.*, 1879, **8**, 261–274.

4 D. Eschimese, PhD thesis, Universite de Lille, 2019.

5 T. Lecklider, The world of the near field, *Eval. Eng.*, 2005, **44**, 52–57.

6 A. Lewis, M. Isaacson, A. Harootunian and A. Muray, Development of a 500 Å spatial resolution light microscope. I. light is efficiently transmitted through λ/16 diameter apertures, *Ultramicroscopy*, 1984, **13**, 227–231.

7 D. W. Pohl, W. Denk and M. Lanz, Optical stethoscopy: Image recording with resolution λ/20, *Appl. Phys. Lett.*, 1984, **44**, 651–653.

8 X. Chen, D. Hu, R. Mescall, G. You, D. N. Basov, Q. Dai and M. Liu, Modern Scattering-Type Scanning Near-Field Optical Microscopy for Advanced Material Research, *Adv. Mater.*, 2019, **31**, 1804774.

9 G. Dai, Z. Yang, G. Geng, M. Li, T. Chang, D. Wei, C. Du, H. L. Cui and H. Wang, Signal detection techniques for scattering-type scanning near-field optical microscopy, *Appl. Spectrosc. Rev.*, 2018, **53**, 806–835.

10 P. Verma, Tip-Enhanced Raman Spectroscopy: Technique and Recent Advances, *Chem. Rev.*, 2017, **117**, 6447–6466.

11 S. V. Boriskina, T. A. Cooper, L. Zeng, G. Ni, J. K. Tong, Y. Tsurimaki, Y. Huang, L. Meroueh, G. Mahan and G. Chen, Losses in plasmonics: from mitigating energy dissipation to embracing loss-enabled functionalities, *Adv. Opt. Photonics*, 2017, **9**, 775.

12 J. Zhang, L. Zhang and W. Xu, Surface plasmon polaritons: Physics and applications, *J. Phys. D. Appl. Phys.*, 2012, **45**, 113001.

13 A. V Zayats and I. I. Smolyaninov, Near-field photonics: Surface plasmon polaritons and localized surface plasmons, *J. Opt. A Pure Appl. Opt.*, 2003, **5**, S16–S50.

14 A. Sihvola, Dielectric polarization and particle shape effects, *J. Nanomater.*, 2007, **2007**, 45090.

15 T. Perova, I. Shaganov and K. Berwick, Accounting for the local field when determining the dielectric loss spectra of metals in the region of the frequencies of volume, surface and localized plasmon oscillations, *Materials (Basel).*, 2020, **13**, 631.

16 C. F. Bohren, *Absorption and scattering of light by small particles*, New York: Wiley, 1983.

17 B. Sepúlveda, P. C. Angelomé, L. M. Lechuga and L. M. Liz-Marzán, LSPR-based

nanobiosensors, *Nano Today*, 2009, **4**, 244–251.

18 K. A. Willets and R. P. Van Duyne, Localized surface plasmon resonance spectroscopy and sensing, *Annu. Rev. Phys. Chem.*, 2007, **58**, 267–297.

19 M. Sui, S. Kunwar, P. Pandey and J. Lee, Strongly confined localized surface plasmon resonance (LSPR) bands of Pt, AgPt, AgAuPt nanoparticles, *Sci. Rep.*, 2019, **9**, 1–14.

20 A. H. Youssef, J. Zhang, A. Dörfler, G. Kolhatkar, A. Merlen and A. Ruediger, Topography-induced variations of localized surface plasmon resonance in tip-enhanced Raman configuration, *Opt. Express*, 2020, **28**, 14161.

21 G. Kolhatkar, J. Plathier, A. Pignolet and A. Ruediger, Effect of the gold crystallinity on the enhanced luminescence signal of scanning probe tips in apertureless near-field optical microscopy, *Opt. Express*, 2017, **25**, 25929.

22 M. Nicklaus, G. Kolhatkar, J. Plathier, C. Dab and A. Ruediger, Direct Observation of Core–Shell Structures in Individual Lead Titanate Ferroelectric Nanostructures by Tip-Enhanced Refractive Index Mapping, *Adv. Funct. Mater.*, 2019, **29**, 1806770.

23 G. Kolhatkar, A. Boucherif, C. Dab, S. Fafard, V. Aimez, R. Arès and A. Ruediger, Composition variation in Al-based dilute nitride alloys using apertureless scanning near-field optical microscopy, *Phys. Chem. Chem. Phys.*, 2016, **18**, 30546–30553.

24 B. Pettinger, K. F. Domke, D. Zhang, G. Picardi and R. Schuster, Tip-enhanced Raman scattering: Influence of the tip-surface geometry on optical resonance and enhancement, *Surf. Sci.*, 2009, **603**, 1335–1341.

25 P. Apell, R. Monreal and S. Lundqvist, Photoluminescence of noble metals, *Phys. Scr.*, 1988, **38**, 174–179.

26 T. X. Huang, S. C. Huang, M. H. Li, Z. C. Zeng, X. Wang and B. Ren, Tip-enhanced Raman spectroscopy: Tip-related issues, *Anal. Bioanal. Chem.*, 2015, **407**, 8177–8195.

27 A. Sacco, D. Imbraguglio, A. M. Giovannozzi, C. Portesi and A. M. Rossi, Development of a candidate reference sample for the characterization of tip-enhanced Raman spectroscopy spatial resolution, *RSC Adv.*, 2018, **8**, 27863–27869.

28 P. R. West, S. Ishii, G. V Naik, N. K. Emani, V. M. Shalaev and A. Boltasseva, Searching for better plasmonic materials, *Laser Photon. Rev.*, 2010, **4**, 795–808.

29 J. A. Faucheaux, A. L. D. Stanton and P. K. Jain, Plasmon resonances of semiconductor nanocrystals: Physical principles and new opportunities, *J. Phys. Chem. Lett.*, 2014, **5**, 976–985.

30 M. Nicklaus, PhD thesis,INRS-EMT, 2013.

31 L. Novotny, in *Progress in Optics*, Elsevier, 2007, vol. 50, pp. 137–184.

32 J. Zhao, A. O. Pinchuk, J. M. McMahon, S. Li, L. K. Ausman, A. L. Atkinson and G. C. Schatz, Methods for describing the electromagnetic properties of silver and gold nanoparticles, *Acc. Chem. Res.*, 2008, **41**, 1710–1720.

CONTENTS

LIST OF FIGURES

LIST OF TABLES

LIST OF ABBREVIATIONS

AFM	Atomic Force Microscopy (or Microscope)
CNT	Carbon Nano-Tube
CT	Charge-Transfer
EELS	Electron Energy Loss Spectroscopy
EM	Electromagnetic
FIB	Focused Ion Beam
LSPR	Localized Surface Plasmons Resonance
LSP	Localized Surface Plasmon
NA	Numerical Aperture
PL	Photoluminescence
QY	Quantum Yield
RRS	Resonance Raman Scattering
SAM	Sell-Assembled Monolayers
SEM	Scanning Electron Microscopy (or Microscope)
SERS	Surface-Enhanced Raman Spectroscopy
SNOM	Scanning Near-field Optical Microscopy (a.k.a. NSOM)
aSNOM	Apertureless Scanning Near-field Optical Microscopy
c-SNOM	Collection Scanning Near-field Optical Microscopy
SPM	Scanning Probe Microscopy (or Microscope)
SPP	Surface Plasmon Polariton
SP	Surface Plasmon
STM	Scanning Tunneling Microscopy (or Microscope)
TEM	Transmission Electron Microscopy (or Microscope)
TERS	Tip-Enhanced Raman Spectroscopy (or Microscope)

1. Raman scattering and Raman spectroscopy

1.1 Basic principles

The scattering of light is a common physical processes and natural phenomenon. It occurs when monochromatic light with frequency ν_0 irradiates a scatterer, and undergoes elastic or inelastic interaction i.e. deviating from its original propagating direction or also changing energy respectively. The scattered light consists mostly of light with identical frequency ν_0 to that of the incident light. This part of the scattered light interacts elastically with the scattered body (i.e. without energy transfer) and is known as Rayleigh scattering. The weak inelastic scattering process yields frequency-symmetrical component ($\nu_0 - \nu_p$ and $\nu_0 + \nu_p$ bands) on both sides of the Rayleigh line. This inelastic scattering is referred to as the Raman scattering, more specifically the Stokes line with frequency $\nu_0 - \nu_p$ and anti-Stokes line with frequency $\nu_0 + \nu_p$. The name Raman relates to the Indian physicist C. V. Raman who, together with his co-researcher K. S. Krishnan, firstly observed this frequency change during scattering processes in gases and liquids in 1928 and which was awarded the Nobel prize in physics in 1930.[1] Incident photons in Raman scattering interact with the electrons of bonds in the studied matter and lead to energy exchange between the photons and the intrinsic vibrational and rotational energy level of the probed matter. According to classical electrodynamics theory, under the influence of a periodically varying external electric field, the polarizable electrons in an atom (or atoms in a molecule or crystal) undergo an induced oscillation around their equilibrium positions, resulting in a change of electric dipole moment given by

$$P_i = \alpha_{ij} \cdot E_j = \alpha_{ij} \cdot E_{0,j} \cos(2\pi\nu_0 t) \qquad 1.1.1$$

where E and ν_0 being the electric field and frequency of the incident light respectively; E_0 is the amplitude of the oscillating electric field; α_{ij} is the symmetric polarizability tensor. Eq. 1.1.1 makes use of Einstein's sum convention. Each normal mode of vibration has its own polarizability tensor that slightly deviates from the static case under a thermal vibration around the equilibrium position. These vibrations are typically much slower than the impinging light. For simplicity, we will omit the tensor character of the polarizability for the moment and describe a one-dimensional case for which, in the presence of a vibrational frequency ν_p around the equilibrium position, the polarizability can be expressed as a Taylor expansion for small oscillations amplitudes:

$$\alpha = \alpha_0 + \left.\frac{\partial \alpha}{\partial q}\right|_{q=0} dq \cdot \cos(2\pi\nu_p t) \qquad 1.1.2$$

where α_0 is the polarizability of the undistorted chemical bond, while the second term relates to a small oscillating change in the polarizability at the frequency ν_p of a phonon. The contribution is only considered for small amplitudes *q* (harmonic approximation) in the vicinity of the equilibrium position i.e. for *q=0*. It is worth noticing that the oscillation coordinate *q* is defined in the coordinate system of the center of gravity for every single normal mode which may be non-trivial to express explicitly. Inserting Eq. *1.1.2* in Eq.*1.1.1* yields:

$$\begin{aligned} P &= \left[\alpha_0 + \frac{\partial\alpha}{\partial q}\bigg|_{q=0} dq \cdot \cos\left(2\pi\nu_p t\right)\right] \cdot E_0 \cos(2\pi\nu_0 t) \\ &= \alpha_0 E_0 \cos(2\pi\nu_0 t) + \frac{\partial\alpha}{\partial q}\bigg|_{q=0} dq \cdot \cos\left(2\pi\nu_p t\right) E_0 \cos(2\pi\nu_0 t) \end{aligned} \qquad 1.1.3$$

in which the first term again describes the elastic interaction of Rayleigh scattering. The multiplication of two oscillation terms in the second term yields the following expression:

$$\alpha_0 E_0 \cos(2\pi\nu_0 t) + \frac{\partial\alpha}{\partial q}\bigg|_{q=0} dq \cdot E_0 \cos\left[2\pi\left(\nu_0 \pm \nu_p\right)t\right] \qquad 1.1.4$$

This equation refers to the three simultaneous oscillation bands with frequency ν_0, $\nu_0 - \nu_p$, and $\nu_0 + \nu_p$. The three resulting re-emission processes of photons are Rayleigh scattering, Raman Stokes and anti-Stokes scattering respectively. It is important to note that if the molecular vibration does not induce changes in polarizability ($\frac{\partial\alpha}{\partial q}\big|_{q=0} dq$=0), no Raman scattering will be observed.

The above explanation of Raman scattering is based on wave model. It can also be explained based on quantum mechanics theory. Under the influence of the incident photons, the quantum state of the target particles changes. The incoming photons promote the electrons in the scatterer to higher virtual energy states (electronic state for resonant Raman scattering). Upon excitation, the electrons radiate instantaneously and return to lower energy states, which can either be the original states (in the case of Rayleigh scattering), or states of a vibrational or rotational mode with energy above the original states (in the case of Raman scattering). *Figure 1.1* is the Jablonski diagram, which depicts the energy level of the Rayleigh, Raman Stokes and anti-Stokes scattering process.

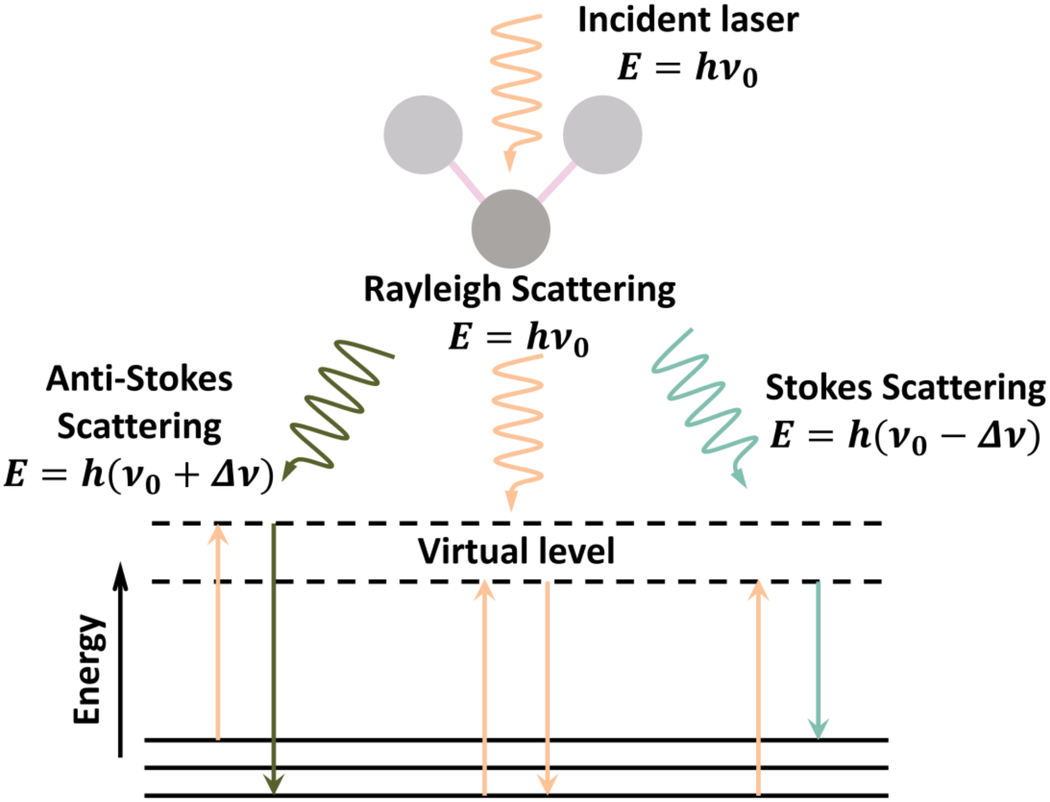

Figure 1.1: Jablonski diagram of the energy level of the Rayleigh, Raman Stokes and anti-Stokes scattering.

For Raman scattering, the emitted photon has a different energy $\mathrm{h}(\nu_0 \pm \Delta\nu)$ then that of the incident photon $\mathrm{h}\nu_0$. For the case of Raman Stokes scattering, the final state has a lower energy of $\mathrm{h}(\nu_0 - \Delta\nu)$, a phonon is generated where for Raman Anti-Stokes scattering, the final state has a higher energy $\mathrm{h}(\nu_0 + \Delta\nu)$, and a phonon is absorbed. Therefore, Raman shift, given by the energy difference between the initial and final state, is determined by the structure and property of the scattering system and is capable of distinctively reflect the intrinsic vibrational and rotational structure of the sample under study. In other words, Raman shift serves as a unique 'fingerprint' of a particular molecular structure. Raman shifts are typically given in units proportional to energy by:

$$\Delta\nu = \frac{1}{\lambda_0} - \frac{1}{\lambda_{scatter}} \qquad 1.1.5$$

where λ_0 is the incident light wavelength and $\lambda_{scatter}$ the Raman scattered light wavelength.

The study of Raman scattering and Raman shift is the foundation of Raman spectroscopy, which can provide both chemical and structural information of the studied sample, as well as identify substances via its specific Raman ‘fingerprint’. The main characteristics of Raman spectroscopy can be summarized as follows:

1) The Raman shift is determined by the structural properties of the material in interest: under the excitation of incident light, different material systems have their distinctive Raman signals. Thus Raman spectroscopy reflects the intrinsic vibrational and rotational energy level structure, making it highly efficient in the detection and characterization of various material structures.
2) The Raman shift is – except for rare cases - independent of the incident light frequency: for same material system under study, the Raman shift remains constant with varied excitation wavelength.
3) The absolute value of Raman Stokes shift equals to that of anti-Stokes shift. However, the intensity of Raman Stokes is significantly stronger compared to anti-Stokes. This is due to the fact that only molecules that are vibrationally excited prior to excitation from incident light can generate anti-Stokes, however in reality only a very small number of molecules would exist in the excited level as compared to the ground state according by Boltzmann distribution. The intensity ratio between Raman Stokes and anti-Stokes lines is given by the density of excited modes of the sample under study therefore has long been used as a direct indication of local temperature.[2–5]
4) Due to the relatively small Raman scattering cross-section (typically $10^{-30}cm^2sr^{-1}$) compared to Rayleigh scattering (typically $10^{-28}cm^2sr^{-1}$), Raman scattering is extremely weak, is typically weaker than Rayleigh scattering by around three orders of magnitude and only as low as 10^{-6}~ 10^{-12} of the incident light. [6]

1.2 Conventional optical spectroscopy in nanoscale material characterization

Nanoscience and nanotechnology as the name suggests primarily focuses on the synthesis, characterization, investigation as well as applications of nanostructured materials characterized by at least one dimension in the nanometer (1–100 nm) range.[7] It has been widely acknowledged that as the size of a material decreases, it experiences drastic changes in properties such as chemical, physical, biological etc. compared to those in atomic (molecular) or bulk scale materials. Furthermore, surface effect, quantum effect and so on also become more significant in such nanoscale systems. The study of the overall unique structural characteristics, energetics, response, dynamics, and chemistry of nanomaterials lays the foundations of modern nanoscience and nanotechnology. The development of nanoscience and nanotechnology so far has significantly promoted the understanding as well as the design and precise control of the nanoscale material properties, and eventually leads to developing novel functional materials and devices. Such research fields, including nano-biology, nano-optics, nano-electronics, nano-mechanics and so on have attracted great amount of interest and attention, and have already been carried out extensively.

One of the primary issues in need to be addressed in the rapid development of nanoscience and nanotechnology is the detection and characterization of material and its properties at the nanoscale. Conventional optical spectroscopy techniques such as Raman spectroscopy and infrared spectroscopy, are capable of detecting the emission, absorption or scattering spectra of substances, and by analyzing the spectral characteristics the structural and molecular dynamics information of the measured sample is readily obtained. Furthermore, conventional optical spectroscopy techniques are sensitive and can also be conducted in situ. They also benefit from their relative simplicity to operate, and generally have few restrictions when it comes to sample preparation and operating environment. Taking conventional far-field Raman spectroscopy for example, it has already become a common laboratory table-top characterization tool and its application has been widely adopted both qualitatively and quantitatively in numerous fields such as pharmaceutical industry, geology and mineralogy, carbon materials, semiconductors, life sciences and various others.

1.3 Conventional optical spectroscopy resolution limit

However, the spatial resolution of conventional optical spectroscopy such as Raman spectroscopy, is severely limited by the optical diffraction limit, making it difficult even impossible in certain cases to meet the needs of nanoscale detection and characterization. This optical diffraction limit is due to the wave nature of light, and exists universally in all optical devices, such as microscope, telescope, and camera and so on.

This limitation in resolution is caused by the intrinsic wave nature of light: Let us consider a beam of light as a transversal electromagnetic (EM) wave with wavelength λ propagating in the direction following wave vector $\vec{k}$ ($\vec{k} = 2\pi/\lambda$). Such EM wave has two contributions, namely an oscillating electric field $\vec{E}$ and an oscillating magnetic field $\vec{B}$, depicted in *Figure 1.2*. Therefore, an EM wave can be described by either one of its field components such as

$$\vec{E} = \vec{E}_0 \cdot cos(2\pi\nu t + kx + \phi) \qquad 1.3.1$$

where t as time, x as position and ϕ as phase.

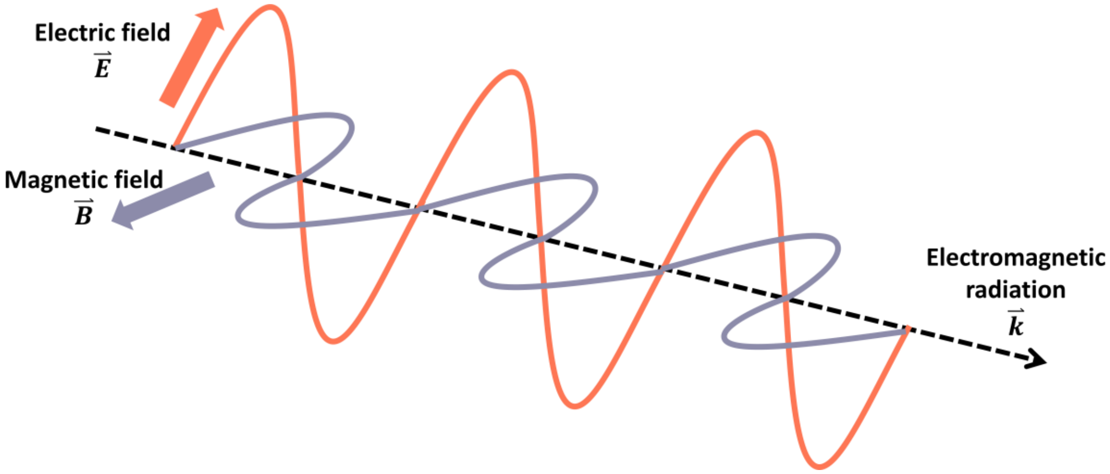

Figure 1.2: Light as an EM wave with an oscillating electric field and a magnetic field.

The diffraction of light occurs when it is scattered by an object with size smaller or comparable to that of the wavelength of the incident light. During a scattering process, every point of the scatterer acts as new light emitter, thus creating an interference pattern in the far-field. In the case of a diffraction process, a diffraction pattern with interference maxima and minima is generated in the far-field due to the relative phase shift. For the diffraction pattern generated by a point light source the bright region in the center (maximum) together with the first concentric ring of lower intensity (minimum) around it, is called the Airy disk (*Figure 1.3*). The diffraction of light governs the resolution limit of all optical devices, which is defined as a minimum distance r which two points of a scatterer can be readily distinguished. This optical limit can be estimated via either Abbe or Rayleigh criteria and is given by:[8,9]

$$r \simeq 0.61\frac{\lambda}{NA} \qquad \textit{1.3.2}$$

where NA is the numerical aperture of the objective. r can be approximated in practice as 0.61λ. As *Figure 1.3* depicts, two points are only optically separated if the overlapping intensity is no larger than 74% of the maximum (I_{max}). [10]

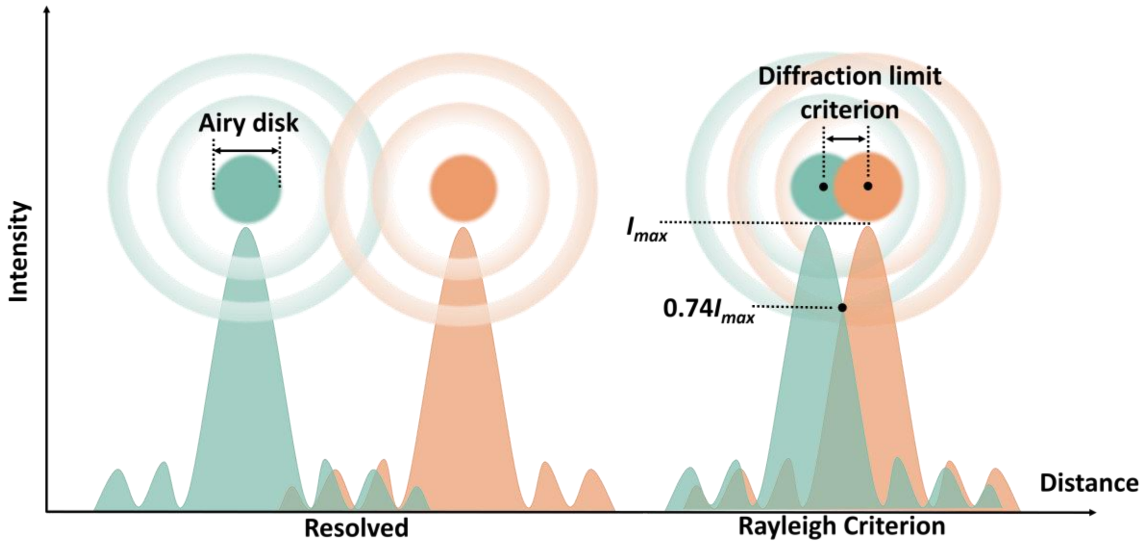

Figure 1.3: Airy patterns of two successive point light sources, from separated to be optically resolved until reaches Rayleigh criterion for diffraction limit

From equation it is obvious that in order to increase the optical resolution, we can either increase the NA of the objective or use light source with shorter wavelength, which will be discussed in the following two subsections, but with all this being said, it will remain in the order of magnitude of the wavelength. [11]

1.3.1 Numerical aperture of an objective

Numerical aperture (NA) or object-side aperture, was firstly defined by Abbe for microscope objectives as well as condensers. It is a measure of the ability of an objective to gather light and is given by:

$$NA = n \cdot sin\, \theta \qquad 1.3.3$$

where *n* is the refractive index of the surrounding environment of the objective (*e.g.* n=1 for air), and θ is the half opening angle of the objective (*Figure 1.4*).

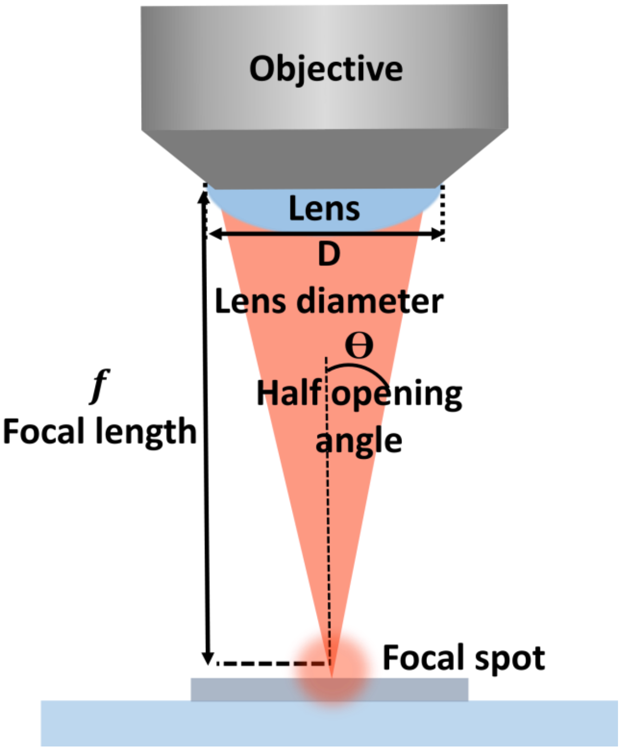

Figure 1.4: sketch of an objective. Frontal lens has diameter D, half opening angle ϴ and focal length f.

In practice, it is difficult to obtain a NA value larger than 0.95 with dry objectives. Thus high NAs are often obtained by increasing the imaging medium refractive index of the surrounding medium. Currently, immersion type objectives are available in medium such as water (n=1.33), glycerin (n=1.47), and immersion oil (n =1.51). Theoretically speaking, the highest NA obtainable is with oil immersion with a value of 1.51, whereas in practice most oil immersion objectives have NAs commonly ranges from 1.0 to 1.35 with a maximum value of 1.4.

Furthermore, the NA can be increased via decreasing the focal length f and increasing lens diameter D which will increase opening angle θ as a result. However, this will result in a significant decrease in the working distance of the objective, meaning the sample will have to be placed extremely close to the objective. Thus even though it is possible to fabricate objectives that sacrifice working distance to obtain higher NA, such objectives are not always practical for application.

1.3.2 Optical techniques with short wavelength

In order to improve the optical resolution limited by diffraction limit, aside from increasing NA, light source with shorter wavelength can also be adopted. For example, electron beams, ion beams, and X-rays with wavelengths much shorter than that of visible light have been used in the detection as well as characterization of the various sample systems. The corresponding techniques include scanning electron microscopy (SEM), transmission electron microscopy (TEM), electron energy loss spectroscopy (EELS) and other methods. However, compared with the conventional optical spectroscopy techniques, the physical processes of the above methods are relatively complicated, electron-based techniques generally require high vacuum conditions and the information obtained is often difficult to analyze without a prior knowledge of the sample under study. Furthermore, due to the decreased incident wavelength which results in higher energy input, the operating environment as well as sample preparation become more demanding, and samples are more prone to be damaged during the measurements.

To sum up, when we narrow down our discussion onto conventional Raman spectroscopy, it faces two main challenges in the application of modern nanoscience and nanotechnology. Firstly, as it is the case of all conventional optical spectroscopy techniques, due to the intrinsic wave property of light, the diffraction limit hinders the maximum spatial resolution to several hundreds of nanometers, making it insufficient for the study of systems in the nanometer scale. Secondly, the Raman scattering cross section is extremely small, far smaller than that of Rayleigh scattering and photoluminescence. In systems down to nanoscale or single molecular detection, the weak Raman scattering makes it extremely difficult, if not impossible to detect any signal.

Under such context, the concept of near-field optics was introduced to cope with the above-mentioned issues.

2 Near-field optics

2.1 Transition from far-field to near-field

Diffraction limit of light has always been considered as an unbridgeable divide which caps the upper spatial resolution limit in conventional optical spectroscopy. With further research, it is acknowledged that the Rayleigh criterion is only valid for optical far-field, where the distance d between the measured objects is much larger than the incident wavelength λ. When d starts to decrease, we reach a region where the far-field approximation is no longer valid anymore, and also evanescent EM waves become more dominant in its contribution to the global field. For nanoscale emitter (or optical antenna), the transition of EM field from far-field to near-field is shown in *Figure 2.1*. [12]

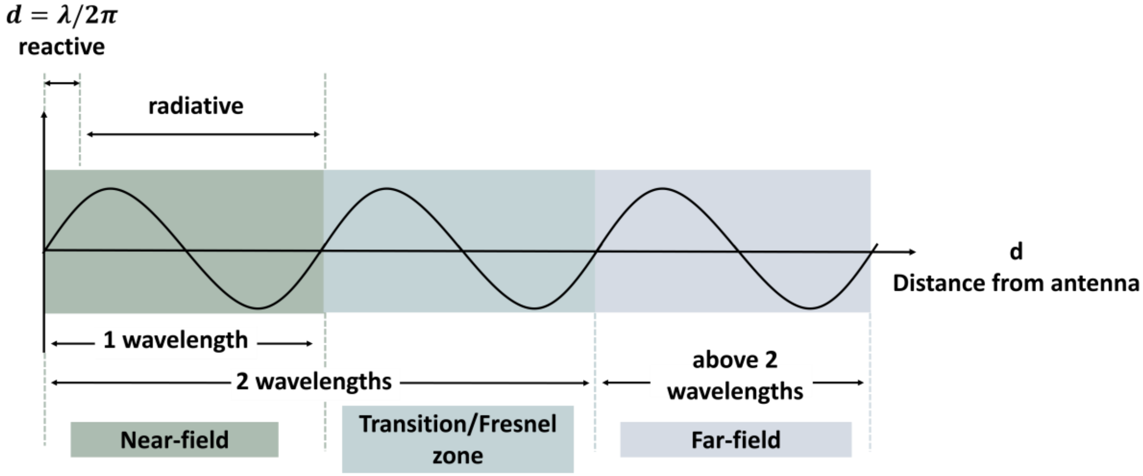

Figure 2.1: Transition of EM field from far-field to near-field based on distance d to a nano-antenna.

Far-field is the region where d is above 2 wavelength, where the Rayleigh criterion is valid. The transition (or Fresnel) zone lies between distances of 1 to 2 wavelengths. And near-field is the region where d is smaller than the wavelength λ, which can also be dived into two regions, namely a reactive region with d smaller than $\lambda/2\pi$ and a radiative region from $\lambda/2\pi$ to 1 wavelength.

2.2 Early development of near-field optics

In an article published in 1928, Irish physicist Synge suggested an idea to obtain information from the near-field region beyond the diffraction limit in the visible range through the utilization of sub-wavelength aperture in an opaque screen.[13] However this idea was not realized until 1972 by Ash and Nicholas in which they used a microwave with 3 cm wavelength. [14] Upon illumination from far-field, evanescent waves can be found at an aperture to form a point emitting source (Huygens elementary emitter). Then this point source is brought very close (less than a wavelength) to the sample under study and scanned alongside the surface during which any light either transmitted or reflected is recorded and analyzed. In such a way, an optical image with a resolution below diffraction limit can be achieved, and this optical technique is part of what is often referred to as super-resolution microscopy. This eventually paved way for high resolution optical imaging while breaching the diffraction limit in the visible range. However, with a decrease in illumination light wavelength, size of the corresponding sub-wavelength aperture and near-field range, thus posing more severe demands on the fabrication process of suitable apertures as well as the precise control of the scanning system. In other words, spatial resolution has to be traded for transmitted intensity. It was not until the invention of scanning tunneling microscopy (STM) in 1982 that the nanoscale space control and scanning techniques were matured enough to provide an adequate technical condition for scanning near-field microscopy.[15] Shortly afterwards, in 1984, Pohl et al. and Lewis et al. independently achieved optical detection resolution beyond diffraction limit in the visible range, thus opening a new chapter in near-field optics research.[16,17] These optical techniques were labelled “scanning near-field optical microscopy” (SNOM) or near-field scanning optical microscopy (NSOM).

2.3 Scanning near-field optical microscopy (SNOM)

2.3.1 Aperture-SNOM

Currently, two types of SNOM are most widely adopted depending on the types of probe (antenna) used. In aperture mode (aperture-SNOM) also known as collection SNOM (c-SNOM), a sharp optical fiber is used (an example of aluminum-coated aperture probe is shown in *Figure 2.2*).[18] The tapered optical fiber in use is metal-coated with an angle leaving an ultra-small opening ($d<\lambda$) at the apex, through which light can either exit or enter. The standard optical fiber probes used in aperture-SNOM typically have diameters in the range of 80 to 250 nm, and in some cases can be as small as 10 to 20 nm via advanced nanofabrication techniques.[19] Upon illumination, the optical fiber generates an evanescent field which exits from its sub-wavelength aperture, creating an optical near-field. Then the optical fiber is brought sufficiently close to the surface of the sample under study where the near-field gets scattered, and the evanescent waves result in propagating waves that are collected in the far-field through detectors.

There are five modes of operation (distinguished based on the direction and position of incident and signal light collection) and are shown in *Figure 2.3*.[20,21] The advantage of aperture-SNOM is that the sample is locally excited in the absence of any far-field background that may interfere with the signal collecting. Currently, the spatial resolution of aperture-SNOM is in the range of 50 ~ 100 nm.[22]

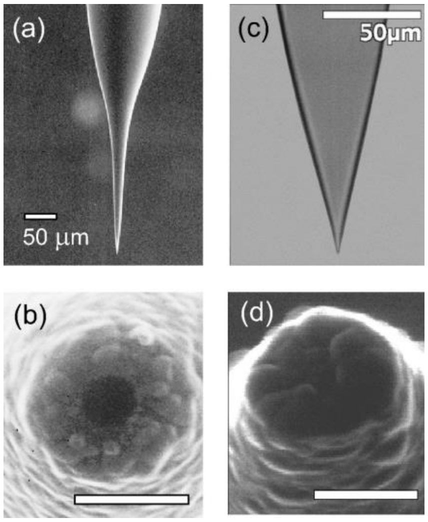

Figure 2.2: Aluminum-coated aperture probes prepared by pulling (a) (b) and etching (c) (d).18

© 2000 American Institute of Physics

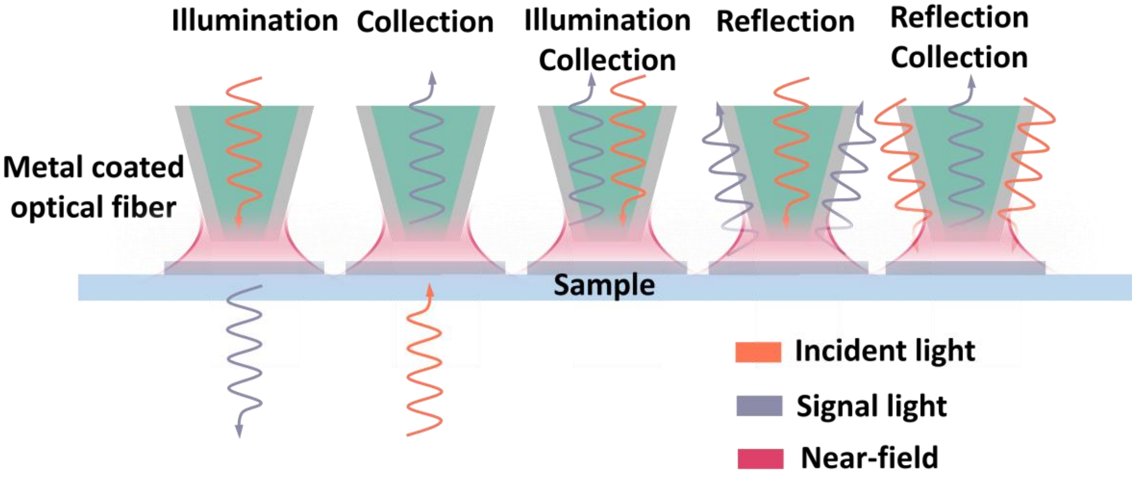

Figure 2.3: Aperture-SNOM modes of operation: a) illumination, b) collection, c) illumination collection, d) reflection and e) reflection collection

At the moment, two significant limitations of aperture-SNOM remain challenging:

1) The competition between light transmission and the size of the aperture. The spatial resolution of aperture-SNOM depends on the aperture size, whereas the amount of light transmission is proportional to the 4th power of the aperture size. In order to improve light transmission one inevitably has to increase aperture size which in turn sacrifices spatial resolution.[23,24]
2) A fundamental lower limit of aperture size of approximately 10 nm due to the limited skin depth in metals as a function of the frequency of the incident EM source.[19,25]

2.3.2 Apertureless SNOM (aSNOM)

In order to overcome the technical challenges in aperture-SNOM, a second type is of SNOM, namely the apertureless SNOM (aSNOM), also known as scattering-SNOM, which involves the utilization of an ultra-sharp probe, was developed. In aSNOM, when incident light illuminates the ultra-sharp probe, the EM field is enhanced over the incident field at the immediate vicinity of the probe apex. [26] The probe functions both as a light confiner (induced by the extremely small tip radius), a light enhancer and a light scatterer (partly due to its elongated shape, in analogy to an optical antenna).[27] Under the illumination of incident light, the optical probe is brought to the surface of the sample, where the regional evanescent field generated by the sample-light interaction is enhanced and scattered into the far field, completing a near-field detection to far-field collection and detection process (*Figure 2.4*).

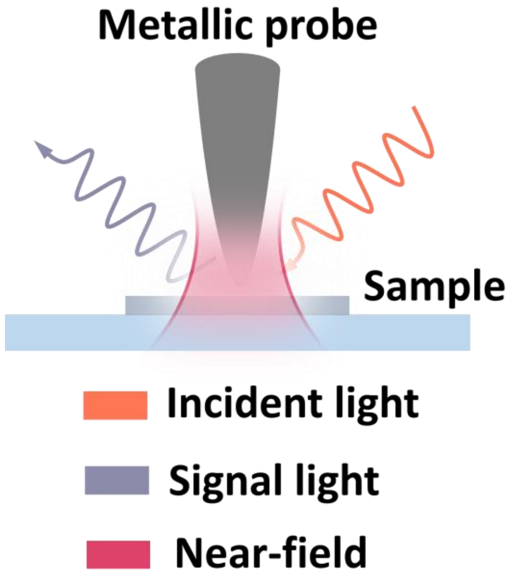

Figure 2.4: Sketch of aSNOM operating mechanism, the metallic probe used is similar to that in scanning probe microscopy.

In this way, the spatial resolution is solely dependent on the radius of the optical probe, in other words, independent to the incident light wavelength.[26] Thus aSNOM overcomes the technical dilemma of balancing between light transmission and aperture size for the sake of maximizing spatial resolution in aperture-SNOM. Currently, aSNOM allows for high spatial resolution far below 10 nm.[27] However, the intensity of scattered near-field signal from the probe is extremely weak. It may also be superseded by comparatively strong background signal. Thus one of the main challenges for aSNOM is how to effectively detect as well as subsequently extract near-field information embedded in the detected signals.[28]

Up to date, current applications of aSNOM are generally dedicated to the study of Raman spectroscopy in the visible range in which plasmon properties play a significant role, such as surface-enhanced Raman spectroscopy (SERS) and tip-enhanced Raman spectroscopy (TERS).

3 Plasmonics

In the previous section, it has been demonstrated briefly that SNOM as a near-field optical technique is capable of providing spatial resolution down to and even below10 nm, which is the main step to go beyond the diffraction limit of optics. However, light can also be confined to dimensions way below the diffraction limit through the resonant interaction with free electrons of materials under certain conditions. This resonant interaction which results in a strong confinement of light is the foundation of the research field of plasmonics, or nano-plasmonics when we refer to such study of systems in nanometer scale. In short, plasmonics explores the interaction between EM radiations (particularly light) and free electrons at the interface of a metal and a dielectric medium. Together with the rapid development in nanoscience and nanotechnology since the early 1990s, nano-photonics, the study of interactions between light and structures near or below the scale of the electromagnetic wavelength interaction at the nanometer scale has emerged and prospered.[29,30]

A plasmon is a quasiparticle which represents the quantization of plasma oscillations. In other words, it is the collective oscillations of free electron gas density. Plasmons can be found most commonly in metals, as the electrons are highly delocalized. Inside metals, plasmons are referred to as bulk plasmon (*Figure 3.1* (a)). Plasmons that are confined to an interface between metal and dielectric are called surface plasmons (SPs). The significance of SPs in nanophotonics is its ability to couple with incident photons under certain conditions (which will be discussed in detail in later sections), which will form propagating surface plasmon polaritons (SPPs) (*Figure 3.1* (b)). SPPs in principle are enhanced evanescent EM fields that propagate along metal-dielectric interface which decay exponentially from the boundary to the environment. [31,32] SPPs have been subjected to extensive studies due to their unique properties which have proven to be promising in study of interaction between light and surfaces and surface electrons in the intensity range extending from perturbative phenomena up to extreme nonlinear optics. [33] Furthermore, when a nanoparticle with sub-wavelength dimension couples its surface electron oscillations with incident photons to form surface plasmons, instead of propagating as in the case of SPPs, these SPs are highly localized and bound to the surface of the nanoparticle, known as localized surface plasmons (LSPs) (*Figure 3.1* (c)). When the incident photons reach the resonance plasmon frequency of the nanoparticle, the coherent oscillation of free electrons becomes in phase with the scattered EM field. Under this condition, a localized surface plasmons resonance (LSPR) is generated in which the EM enhancement obtain its maximum. [34] In particular, SP and LSP are the main components in nano-plasmonics and will be discussed in detail in later sections.[35]

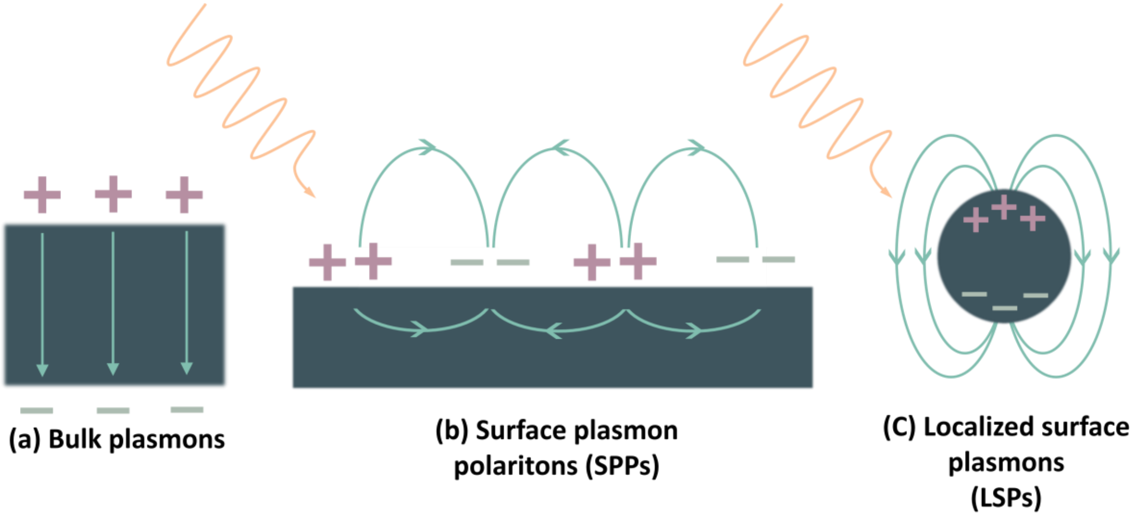

Figure 3.1: (a) bulk plasmon inside metal (b) surface plasmon polaritons (SPPs) propagating along metal-dielectric interface and (c) localized surface plasmons (LSPRs) confined to the very vicinity of a metal nanoparticle with sub-wavelength dimension.

The plasmonic properties of metals are determined by the interaction between their free electrons in the conduction bands and incident EM waves, especially light. Even long before getting to understand the mechanism behind, ancient people have already exploited this interesting metal-light interaction. The magnificent Lycurgus Cup which dates back to 4th century Roman time is a perfect example. As seen in Figure 3.2, depending on the direction of the incident light, the cup presents vividly different colors (green with reflected light and red in transmitted light).[36] This effect is in fact due to the tiny amount of silver and gold particles embedded in the glass structure which have different reactions when come into interaction with incident light. The same concept has also been adopted in the fabrication of stained glass decorating churches etc.

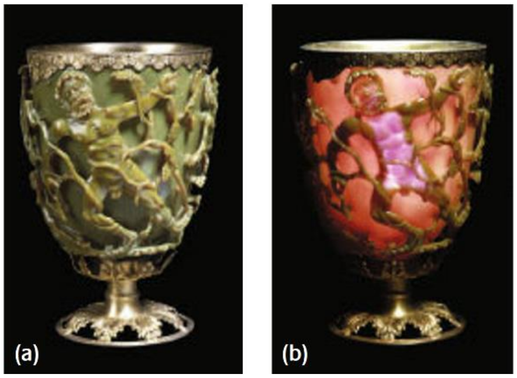

Figure 3.2: Roman Lycurgus Cup shows different colors in reflected (a) and transmitted (b) light.

© The Trustees of the British Museum

The research field of plasmonics and nano-plasmonics has developed and prospered dramatically in the past few decades and currently its application is widely seen in numerous fields, such as photonics and nano-photonics, chemistry, energy, life sciences etc. [37]

3.1 Metal plasmonic properties

Plasmonic properties of metal describe the interaction between free electrons in the conduction band of the metal and the incident fields. The collective oscillation of electrons is comparable to that of a simple damped harmonic oscillator, for which Newton's approximation of damping proportional to the speed of motion is applicable. Lorentz' model is often used to describe the collective oscillation of electrons induced by an external field $\vec{E}$ as a damped Lorentz oscillator.[38] Then the electron motion equation can be written as:

$$-q\vec{E} = m\frac{\partial^2 \vec{r}}{\partial t^2} + \mathrm{m}\mathit{\Gamma}\frac{\partial \vec{r}}{\partial t} + \mathrm{m}\omega_0^2\vec{r} \qquad 3.1.1$$

where m is electron effective mass, $\vec{r}$ is the displacement of electron, $\mathit{\Gamma}$ is the damping rate and ω_0 is the natural frequency. Thus by solving this equation through Fourier transformation we obtain the electron displacement $\vec{r}$ due to external field as:

$$\vec{r}(\omega) = -\frac{q}{m}\frac{\vec{E}(\omega)}{(\omega_0^2 - \omega^2 - i\mathit{\Gamma}\omega)} \qquad 3.1.2$$

The displacement of electron $\vec{r}(\omega)$ then leads to a dipole moment:

$$\vec{p}(\omega) = -q\vec{r}(\omega) = \frac{q^2}{m}\frac{\vec{E}(\omega)}{(\omega_0^2 - \omega^2 - i\mathit{\Gamma}\omega)} \qquad 3.1.3$$

Thus macroscopically, the generated polarization per unit volume as a sum of total dipole moment is:

$$\vec{P} = \mathrm{N}\vec{p}(\omega) \qquad 3.1.4$$

where N is the number of atoms per unit volume. Polarization per unit volume can also be described by electric susceptibility $\chi_e(\omega)$ as:

$$\vec{P} = \chi_e(\omega)\varepsilon_0\vec{E}(\omega) \qquad 3.1.5$$

where ε_0 is the electric permittivity of vacuum. Then we can get susceptibility expressed as:

$$\chi_e(\omega) = \frac{Nq^2}{m\varepsilon_0}\frac{1}{\omega_0^2 - \omega^2 - i\mathit{\Gamma}\omega} \qquad 3.1.6$$

For which we define:

$$\omega_p = \sqrt{\frac{Nq^2}{m\varepsilon_0}} \qquad 3.1.7$$

where $\omega_p$is the plasma frequency. Then re-writing equation 3.1.6 we obtain:

$$\chi_e(\omega) = \frac{\omega_p^2}{\omega_0^2 - \omega^2 - i\Gamma\omega} \qquad 3.1.8$$

The relative permittivity ε_r is given by:

$$\varepsilon(\omega) = 1 + \chi_e(\omega) = \varepsilon' + i\varepsilon'' \qquad 3.1.9$$

Thus equation 3.1.9 can be expressed as:

$$\varepsilon(\omega) = 1 + \frac{\omega_p^2}{\omega_0^2 - \omega^2 - i\Gamma\omega} \qquad 3.1.10$$

with real and imaginary parts:

$$\varepsilon'(\omega) = 1 + \omega_p^2 \frac{\omega_0^2 - \omega^2}{(\omega_0^2 - \omega^2)^2 + \omega^2\Gamma^2} \qquad \varepsilon''(\omega) = \omega_p^2 \frac{\Gamma\omega}{(\omega_0^2 - \omega^2)^2 + \omega^2\Gamma^2} \qquad 3.1.11$$

Equation 3.1.11 is known as the Lorentz model for dielectric function. The real part in the dielectric function describes the strength of polarization that is induced by an external EM field. The imaginary part is related to energy loss due to either absorption and/or scattering process during the interaction with external EM field.

In the case of metals, we assume ω_0 to be 0 due to the fact that most electrons are free to roam and not bound to the nucleus. In analogy to a harmonic oscillator there is no spring to connect them to nucleus, thus no restoring force. Then we can obtain the Drude model for metal dielectric function given below:

$$\varepsilon(\omega) = 1 - \frac{\omega_p^2}{\omega^2 + i\Gamma\omega} \qquad 3.1.12$$

with real and imaginary parts:

$$\varepsilon'(\omega) = 1 - \frac{\omega_p^2}{\omega^2 + \Gamma^2} \qquad \varepsilon''(\omega) = \frac{\omega_p^2\Gamma}{\omega(\omega^2 + \Gamma^2)} \qquad 3.1.13$$

Metals typically have a high density of free electrons, thus according to equation 3.1.7 they have a higher plasma frequency compared to other materials. The intrinsic higher plasma frequency of metals is the key feature that makes metals a promising material for potential plasmonic applications. For most metals, the plasma frequency covers a wide range of approximately 100 nm to 1 mm, from infrared to ultraviolet range.[39] Noble metals such as gold and silver have a plasma frequency within the visible range, making them promising candidates for optical applications.

Ever since its first introduction in 1900, the Drude model for metal has been widely adopted.[40,41] It is especially suitable for metals whose optical response are primarily dependent on their free electrons in the conduction band (such as alkali group metals and metals with three valences). However, the limitation of Drude model is also clear, for example it does not take interband electronic transitions into consideration, which is common when incident photons have higher energy that can trigger valence-conduction band transitions.[42,43] Nevertheless, Drude model is still a pioneer attempt on the analysis of optical properties of metals, which even todays still has significant meaning in the field of nano-plasmonics and nano-photonics.

3.2 Surface plasmon polariton (SPP)

When an incident EM wave has a frequency below the plasma frequency, the dielectric function of a metal becomes imaginary. As a result, the propagation of such EM wave is strongly attenuated inside the metal. However, at the interface between a dielectric medium (positive real permittivity) and a metal (complex permittivity), under certain conditions, EM waves with frequencies in and above the THz range are capable of inducing longitudinal and coherent oscillation of electrons, known as surface plasmon polaritons (SPPs). The term polariton is defined as a quasiparticle, which results from a strong coupling between EM radiation and a charged particle.[44] SPPs are confined to the close vicinity of the metal-dielectric interface and propagate in a wave-like manner along the metal surface until energy dissipation such as heat loss or radiation into free space has them fade.[45,46] The electron oscillations involved in this process inevitably create an EM field which is enhanced near the surface and decays exponentially (characteristic evanescent wave) in direction normal to the interface for both metal and dielectric medium (*Figure 3.3*).[32]

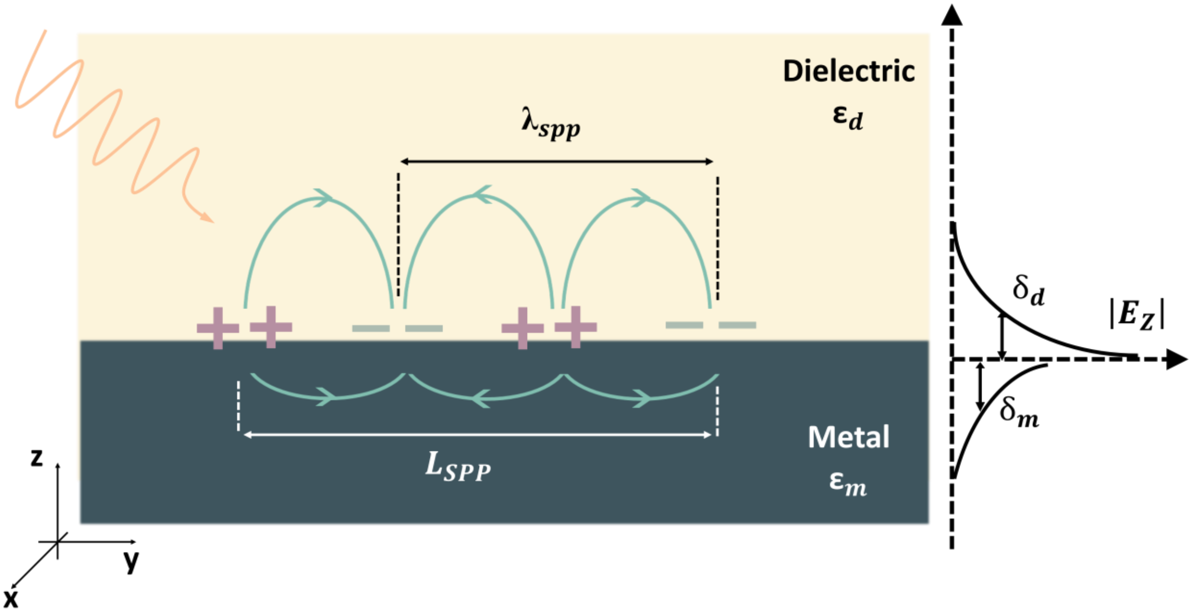

Figure 3.3: Illustration of SPP propagation at metal-dielectric interface and intensity decay of generated EM field.

The in-plane wave vector (or momentum) K_{SPP} of SPPs is defined as the wave vector in plane with propagation surface and can be expressed as a function of angular frequency: [47]

$$K_{SPP} = K_0 \sqrt{\frac{\varepsilon_d \varepsilon_m}{\varepsilon_d + \varepsilon_m}} \qquad 3.2.1$$

with $K_0 = \omega / c$ being the free-space wave vector. From equation 3.2.1 we can see that for a given dielectric medium, the relative permittivity of metal plays a significant role in SPPs behavior. The relative permittivity of a metal is complex, thus the wave vector K_{SPP} of SPPs also becomes complex. Its real part is defined as the plasmon wavelength λ_{SPP} while the imaginary part relates to dissipation and is a measure of the propagation length along the metal-dielectric interface. The penetration depths δ_d and δ_m are defined as the distances at which the intensity of the EM field induced by SPPs decays to 1/e inside the dielectric and metal respectively. The propagation length is defined as the distance at which the intensity of the EM field induced by SPPs decays to 1/e along the metal-dielectric interface. It is given by:

$$\delta_d = \frac{1}{K} \sqrt{\left| \frac{\varepsilon_d + \varepsilon_m}{-\varepsilon_d{}^2} \right|} \qquad 3.2.2$$

in dielectric and

$$\delta_d = \frac{1}{K}\sqrt{\left|\frac{\varepsilon_d + \varepsilon_m}{-\varepsilon_m{}^2}\right|} \qquad 3.2.3$$

in metal.[47] In general, δ_d is larger than δ_m, and the difference increases with longer incident wavelengths. [32]

3.3 SPP excitation

The excitation of SPP via free propagating EM waves through a dielectric medium requires a momentum match between the incident EM wave and $\hbar K_{SPP}$. However, the moment ($\hbar K_{SPP}$) of SPP is always larger than that of light in free space ($\hbar K$) for the same frequency ω (*Figure 3.4*), given that the dispersion curve of SPPs is always to the right of the dispersion curve of the dielectric light line (defined as photon dispersion in a dielectric). Due to this momentum mismatch, SPPs also cannot radiate easily into free-space, thus present a bound or non-radiative nature, which is desirable for transmitting or guiding SPPs waves via plasmonic components such as waveguides, couplers etc.[48]

In order to achieve coupling, this momentum mismatch must be overcome at the metal-dielectric interface when:[32,39]

$$\varepsilon_d + \varepsilon_m = 0 \qquad 3.3.1$$

Under that condition, SPPs are readily excited at a frequency of:

$$\omega_{SPP} = \frac{\omega_p}{\sqrt{1 + \varepsilon_d}} \qquad 3.3.2$$

Note that the SPP frequency is lower than that of bulk plasma.

Therefore, as depicted in *Figure 3.4*, at low frequencies, where $\omega < \omega_{SPP}$, ε_m is real and negative. The SPP dispersion curve is very close to the dielectric light line but is always larger (origin of momentum mismatch mentioned earlier). When frequency increases, the SPP dispersion curve deviates gradually from the dielectric light line until reaches ω_{SPP}. The wave vector of the EM wave in the medium is imaginary and the EM wave decays exponentially and in direction normal to the interface. If the frequency continues to increase, the wave vector becomes infinite. At even higher frequencies ($\omega > \omega_P$), ε_m is real but positive in contrast to that when $\omega < \omega_{SPP}$. [39] Metals start to show a transparent character and radiation through the metal occurs.[48]

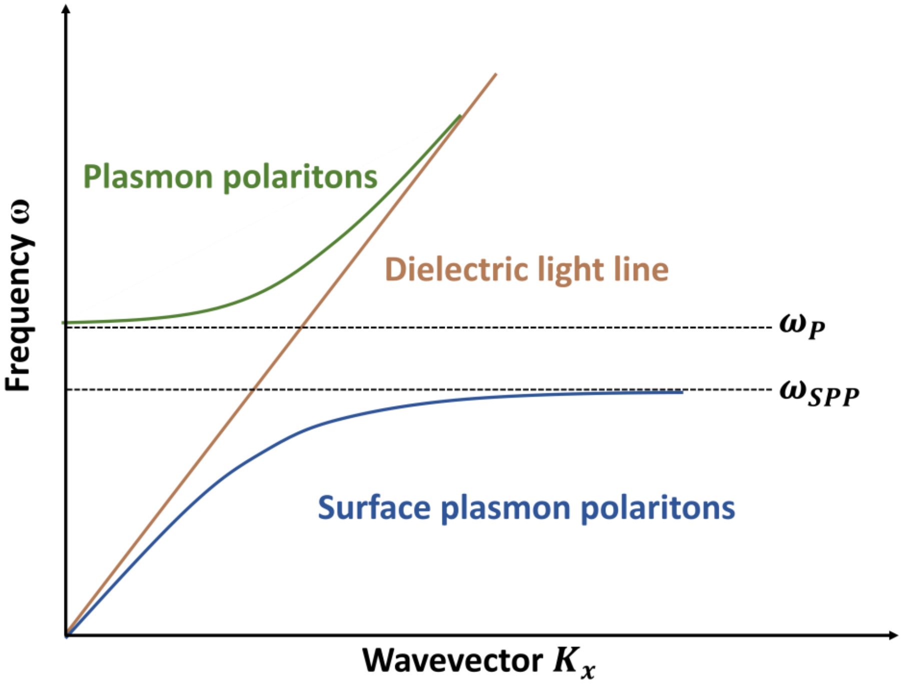

Figure 3.4: Dispersion curves of SPPs (blue), light in vacuum (brown) and PP in bulk metal (green).

In order to overcome this momentum mismatch to effectively excite SPPs at metal-dielectric interface, according to *Figure 3.4*, an EM field with wave vector larger than that of light in free space is required. Throughout the development in near-field optics, researchers have proposed various solutions, the best-known of all are the Kretschmann- and Otto-configuration, both of which are based on principal of total reflection.[49,50]. In short, during a total reflection process, on the side with lower refractive index an evanescent wave is generated, the wave vector of which increases the total wave vector of far-field incident light and can be coupled with SPPs. Furthermore, given an incident light with constant frequency, under certain incident angle it can also carry enough energy to be coupled with SPP. Such an angle results in a sharp 'dip' in the reflectivity curve. [51] On the other hand, the diffraction effects by grating or surface features can also satisfy the momentum matching conditions. The diffracted light from metal–dielectric interface with grating or surface features exhibits larger wave vectors in magnitude compared to that of incident light and can be sufficient to couple to the SPPs. [32,52] Furthermore, near-field probes can also be used for the coupling between light and SPPs by breaking the local conservation of momentum to obtain a wider range of wave vector distributions, thus satisfying the vector momentum match between incident light and SPPs.[53]

Aside from light, electrons can also be used for the excitation of SPPs which was first achieved by Ritchie.[54] However this is beyond the scope of this thesis thus will not be discussed here.

3.4 Localized surface plasmon (LSP)

Parts of the following section are reproduced from: *J. Zhang, G. Kolhatkar and A. Ruediger, Localized surface plasmon resonance shift and its application in scanning near-field optical microscopy, J. Mater. Chem. C, 2021, 9, 6960*. My contribution to the manuscript was to coordinate all contributions to the manuscript, which is a review-style document and the writing of the document including references.

In the previous sections, phenomena relating to surface plasmon occurred at the interface of an infinitely large metal-dielectric surface. However, for a given metallic particle with dimensions equal or smaller than of the incident EM wavelength, contrast to the propagating SPPs on a flat interface, the confined geometrical boundaries of the particle are capable of sustaining a localized oscillation of surface electrons, as seen in *Figure 3.5*, referred to a localized surface plasmon (LSP).

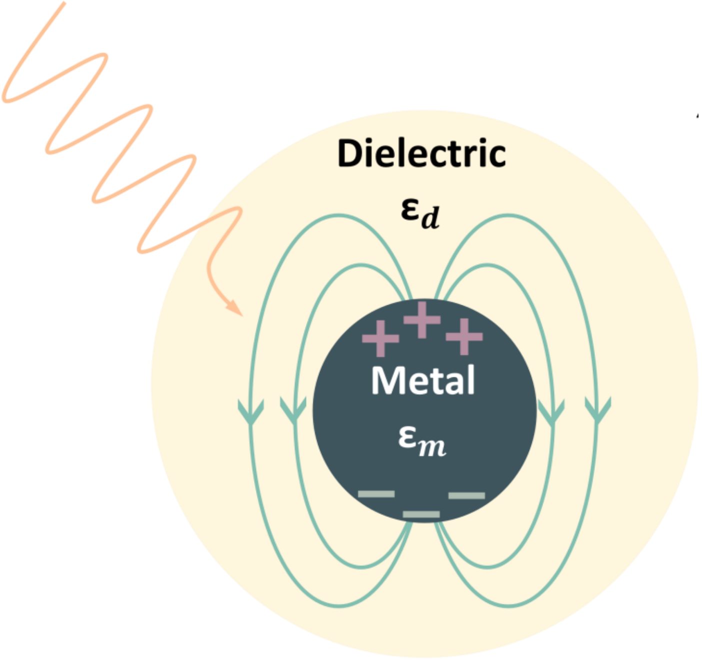

Figure 3.5: Illustration of LSP and intensity decay of generated EM field.

Herein, we take the simple model of a metallic nanosphere as an example to demonstrate the optical response of nanoparticles. It is a simple form of optical antenna which is defined as a structure which is capable of converting far-field EM radiation to near-field (or the other way around) .[55]

The LSP excitation on a metallic nanosphere with radius r by an external electric field is depicted in *Figure 3.6*.

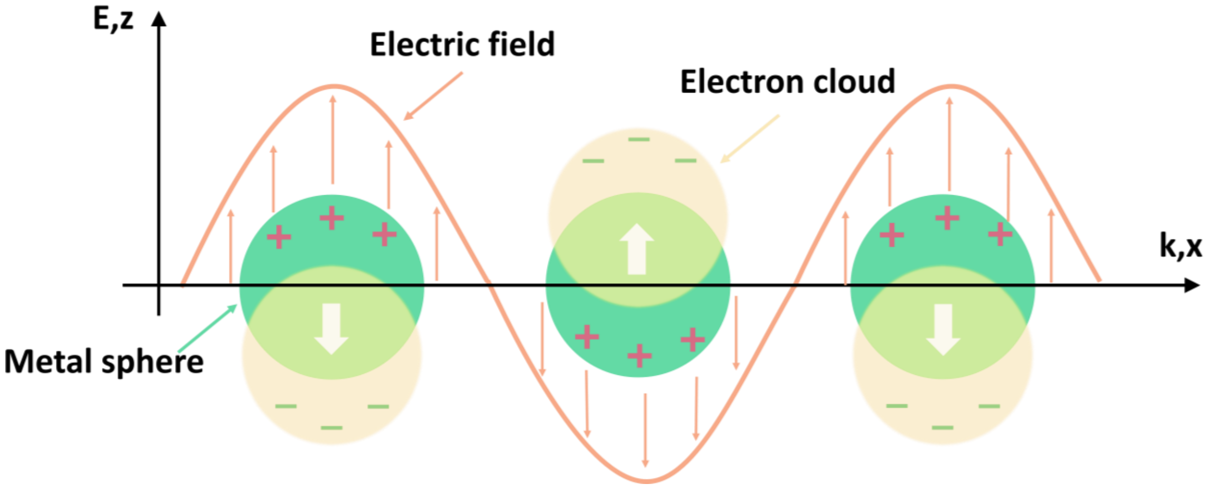

Figure 3.6: Illustration of LSP excitation on metallic nanospheres an external electric field. The displacement of the free electron cloud results in a dipole moment.

As we can see from *Figure 3.6*, the external *E* field leads to a displacement in the free electron cloud of the metal sphere, which results in an induced dipole moment $\vec{p}$ given by:

$$\vec{p} = \vec{E} \cdot \alpha \tag{3.4.1}$$

In which $\alpha(\lambda)$ is the dipolar polarizability in the quasistatic approach:[56]

$$\alpha = 4\pi\varepsilon_0 r^3 \frac{\varepsilon_{sphere} - \varepsilon_d}{\varepsilon_{sphere} + 2\varepsilon_d} \tag{3.4.2}$$

with ε_{sphere} the relative permittivity of metallic sphere, ε_d the relative permittivity of the dielectric medium. In the optical range, ε_{sphere} is approximated by the Drude model introduced in previous sections as:

$$\varepsilon_{sphere} = \varepsilon(\omega) = 1 - \frac{\omega_p^2}{\omega^2 + i\Gamma\omega} \tag{3.4.3}$$

In equation 3.4.2, $\frac{\varepsilon_{sphere}-\varepsilon_d}{\varepsilon_{sphere}+2\varepsilon_d}$ is called the optical response, or g factor, which is a measure of the enhancement of the *E* field. The resonance of the metallic nanosphere locates at $\omega_{\text{resonance}}$ when $\frac{\varepsilon_{sphere}-\varepsilon_d}{\varepsilon_{sphere}+2\varepsilon_d}$ is maximized, that is when:

$$\varepsilon_{sphere} + 2\varepsilon_d = 0 \qquad 3.4.4$$

For spheroidal metallic particles, $\omega_{\text{resonance}}$ can be determined from:

$$\omega_{\text{resonance}} = \sqrt{\omega_p^2 \Big/ 1 + \left(\frac{l+1}{1}\varepsilon_d\right)} \qquad 3.4.5$$

In which l is a shape factor ranging from 1 for spheres and ∞ for needles.[57,58] For example, in the case where the surrounding environment is vacuum whose ε_d equals 1, $\omega_{\text{resonance}}$ of a spherical metallic particle is:

$$\omega_{\text{resonance}} = \sqrt{\frac{\omega_p^2}{3}} \qquad 3.4.6$$

When a metallic particle (regardless of its shape) is excited with the incident light at $\omega_{\text{resonance}}$, the resulted collective oscillation of free electrons is known as localized surface plasmon resonance (LSPR).[59] The excitation of LSPR is the key to the significant enhancement of EM fields, which leads to surface-enhanced Raman scattering (SERS), tip-enhanced Raman scattering (TERS) as well as various other plasmon-enhanced near-field spectroscopy techniques.[60,61] In recent literature, the term plasmon-enhanced Raman spectroscopy (PERS) to describe common features of SERS and TERS has been frequently used. Furthermore, the potential of gold and silver nanoparticles as small-volume, ultra-sensitive and label-free LSPR based sensors has drawn abundant attention in recent studies, especially in the field of biosensing.[62–65] Such application is based on the wavelength shift in the LSPR spectrum arising from local dielectric changes, as the LSPR position is highly dependent on nanoparticle material, size, shape as well as surrounding medium refractive index (*Figure 3.7*).[66–71]

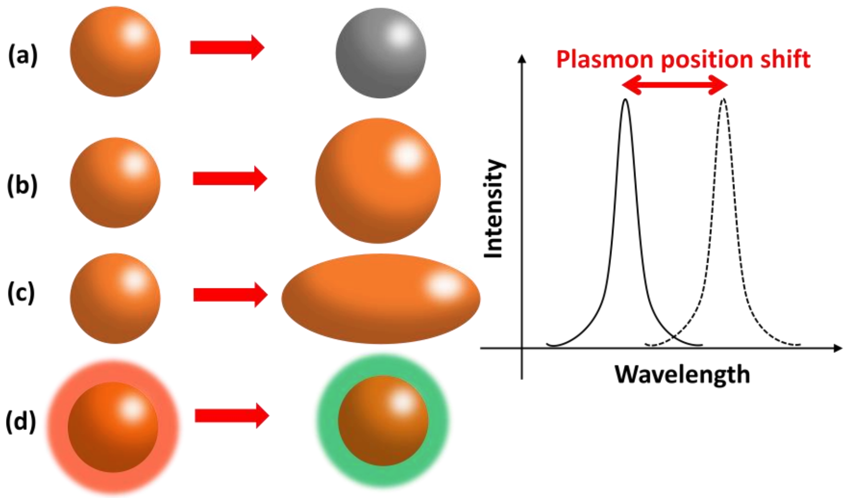

Figure 3.7: LSPR shift induced by change in (a) material, (b) size, (c) shape and (d) surrounding medium refractive index.

For a given nanoparticle with defined geometric properties, the relationship between the LSPR position *λ* and the surrounding medium is approximated in equation (3.4.7) [72]

$$\Delta\lambda = \mathrm{m}\Delta\mathrm{n}\left[1 - exp\left(-\frac{2d}{l_d}\right)\right] \qquad 3.4.7$$

where m is the bulk refractive index response of the NP, n is the refractive index of the surrounding medium (the refractive index is related to the relative permittivity by $n = \varepsilon^{1/2}$), d is the effective adsorbate layer thickness, l_d is the characteristic exponential decay length of the electromagnetic field.[73] Thus by monitoring $\Delta\lambda$, refractive index changes in close vicinity of the noble metal nanostructure surface can be imaged with nanometer precision.

3.5 Plasmon enhanced gold photoluminescence

Photoluminescence (PL) is defined as the light emission process following a photon absorption process. PL of bulk gold was first observed and reported by Mooradian in 1968 as an inefficient process with considerably small quantum yield (QY as low as 10^{-10}), and the phenomenon was explained as an optically excited radiative recombination of sp-band electrons and d-band holes induced via interactions with photons with energy higher than that of direct inter-band transitions.[74,75] Then in 1983, Boyd *et al.* discovered that the QY of gold PL was significantly enhanced with the aid of LSPs in gold with roughened surface compared to smooth gold surface.[76] So far, in order to explain this plasmon enhanced gold PL, two models have been proposed and remain most widely accepted. The first model is based on the emission of a photon after energy transfer from an electron–hole pair to a plasmon excitation.[75] The second model considers plasmonic modes to be the main PL channels as they introduce an antenna effect which enhances the absorption and emission rates significantly.[75–77] Hot carriers generated through direct interband excitation or plasmon excitation and decay are seen as intermediate states in energy relaxation pathways.[77] The LSPR enhanced luminescence photon emission is a three-step process (*Figure 3.8*) in which hot electrons generated from transverse surface plasmon resonance (TSPR) lose their energy nonradiatively, interconvert to LSPR mode, and emit a photon. [78,79]

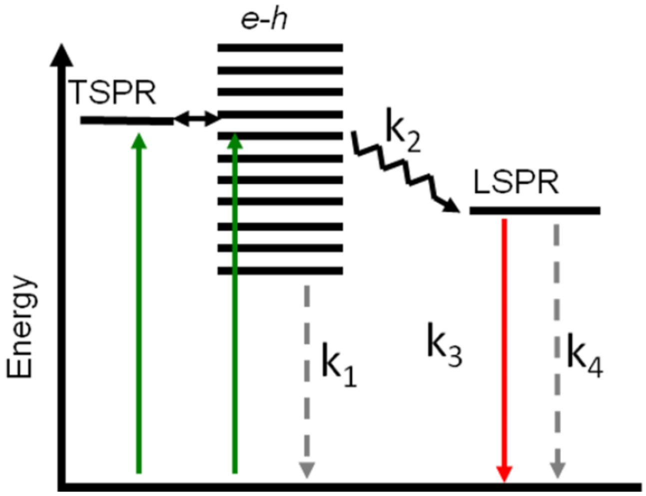

Figure 3.8: Three-step LSPR enhanced luminescence photon emission process.[78] ©2012 American Chemical Society

The LSPR enhanced PL spectrum presents a similar resonance peak, shifts with a change of the dielectric constant of the surrounding medium (Figure 3.9, Figure 3.10), and resembles the response to refractive index change as that of pure LSPR position.[79,80] The linear relationship between peak wavelength and refractive index, as shown in *Figure 3.10*, suggests the potential of LSPR enhanced PL for applications in refractive index sensing.

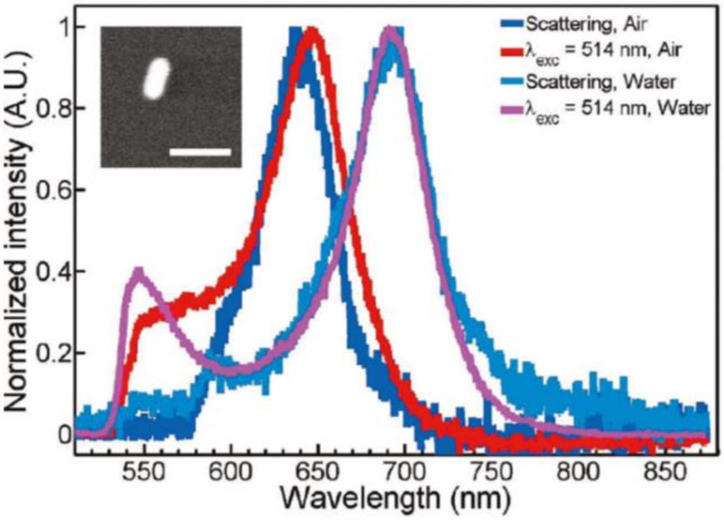

Figure 3.9: Unpolarized scattering (blue and cyan) and 514 nm excited LSPR enhanced PL (red and magenta) spectra of a 33 × 70 nm2 AuNR in air and water.[79] *© 2012 American Chemical Society*

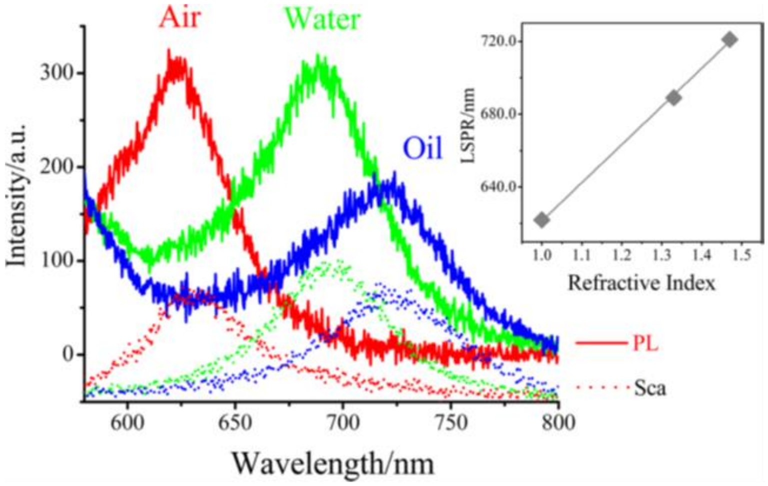

Figure 3.10: LSPR enhanced PL (solid lines) and scattering (dots) spectra of the gold nanorod immersed in air (red), water (green), and glycerol (blue) and the fitting line.[80] *© 2012 American Chemical Society*

4 Surface-enhanced Raman spectroscopy (SERS)

In 1974, Fleischman et al. observed an unusual 10^6 enhancement of Raman signals from a monolayer of pyridine molecules when adsorbed on a rough silver electrode.[81] After further research by Van Duyne et al. this enhancement effect was labelled “surface-enhanced Raman scattering”. [82,83] Surface-enhanced Raman spectroscopy (SERS) is a near-field optical technique based on surface-enhanced Raman scattering. Follow-up studies have demonstrated that the fundamental pre-requisite for such enhancement to occur is the adsorption of molecules onto metallic surfaces with nanometer scale roughness or to the very vicinity of metallic particles. Properties such as shape, size, material type etc. of such roughened metallic surfaces and metallic particles play a significant role in the intensity of enhancement, and systems, which are capable of enhancing Raman signals are known as SERS substrates.[84] Meanwhile, surface-enhanced Raman signal intensity is also dependent on the distance between molecules and SERS substrate, only molecules adsorbed either onto or very close to the substrate (typically within 10 nm) will experience an enhancement in their Raman signal, and such enhancement decays dramatically with distance.[85,86] Thanks to the rapid development in nanofabrication, SERS substrate with various features have been designed and fabricated and have greatly promoted the application of SERS in many fields such as materials science, biochemistry and bio sensing, catalysis, electrochemistry etc.[87,88]

4.1 SERS enhancement mechanisms

Surface-enhanced Raman scattering is a surface optical phenomenon that involves complex interaction between incident light, SERS substrate and molecule; the process is also influenced by the surrounding environment. Due to the complexity of the SERS system, its exact enhancement mechanism is still under debate.[89–92] At the moment, the most widely accepted SERS enhancement mechanisms acknowledges two main contributions, namely EM enhancement (also known as physical enhancement) and chemical enhancement. In practice during a SERS experiment, both factors contribute to the total enhancement simultaneously, making it extremely challenging, if not impossible, to identify and quantify their contribution individually. In general, from a theoretical standpoint SERS enhancement can be categorized into at least one of the four situations as shown in *Figure 4.1*.[91–93]:

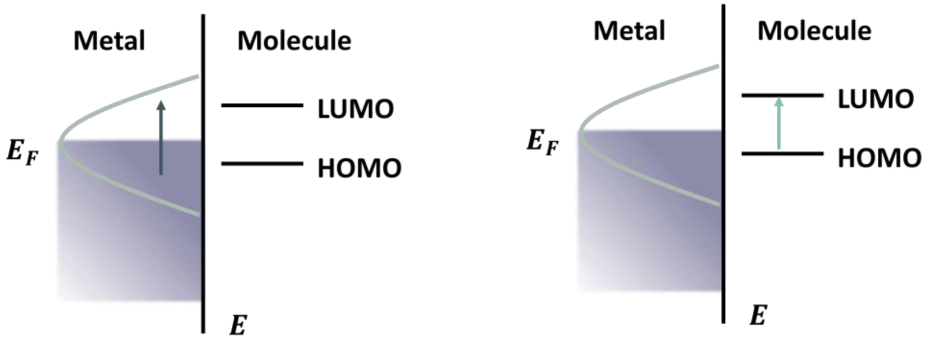

(a) EM enhancement

(b) Resonance Raman scattering (RRS)enhancement

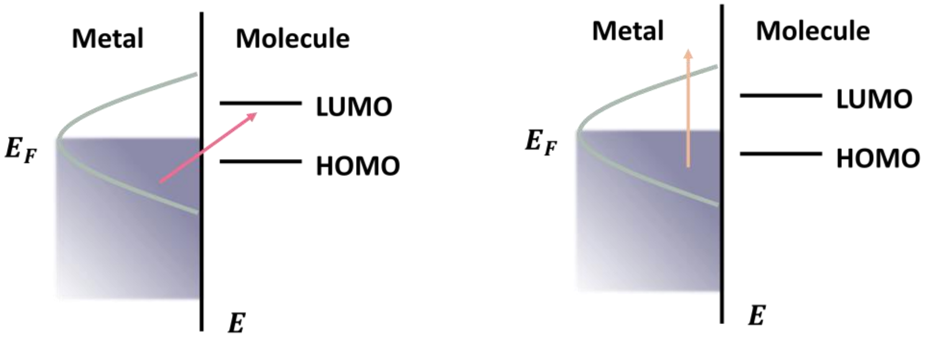

(c) Charge transfer (CT) resonance Raman enhancement

(D) Non-resonant chemical (CHEM) enhancement

Figure 4.1: Illustration of 4 types of possible enhancement scenarios that may occur in SERS.

1) EM enhancement (*Figure 4.1*(a)): the excitation of SPs results in a significant EM field enhancement. It is the strongest contribution to the overall SERS enhancement.[94]
2) Resonance Raman scattering (RRS) enhancement (*Figure 4.1*(b)): when molecule is adsorbed onto the metallic SERS substrate surface, metal-adsorbate complex can be formed which leads to a change in molecular energy level. Resonance Raman scattering will take place when the energy of incident photons matches that of the new molecular electronic transition.
3) Charge-transfer (CT) resonance Raman enhancement (*Figure 4.1*(c)): it is considered to be analogous to the RRS process, only that in this process the transient excited state is a CT level of the metal-adsorbate complex.[95]
4) Non-resonant chemical (CHEM) mechanism (*Figure 4.1*(d)): enhancement induced by specific chemical coupling between molecule and SERS substrate at ground state.[96] The interaction between the molecule and the SERS substrate does not form new electronic states.[97] It contributes the least among other mechanisms.

Scenarios (1) to (3) combined are known as chemical enhancement and scenario (4) is known as EM enhancement.[92] Together with the above two enhancements, the intensity of a certain peak in SERS:[98]

$$I_{SERS} \propto \sum_{\rho,\sigma} \left|(\alpha_{\rho\sigma})_{fi}\right|^2 \cdot \left|\vec{E}(\omega_0)\right|^2 \left|\vec{E}(\omega_s)\right|^2 \tag{4.1.1}$$

in which ρ is the direction of electric field of the incident light and σ is the direction of electric field of the scattered light, $(\alpha_{\rho\sigma})_{fi}$ is the polarizability from initial state i to final state f. $\vec{E}(\omega_0)$ and $\vec{E}(\omega_s)$ are the incident and scattered light electric field intensity, respectively. The term $\sum_{\rho,\sigma}\left|(\alpha_{\rho\sigma})_{fi}\right|^2$ is the chemical enhancement contribution, which signifies that an increase in polarizability will result in a higher SERS intensity; the term $\left|\vec{E}(\omega_0)\right|^2\left|\vec{E}(\omega_s)\right|^2$ is the EM enhancement contribution, which indicates that the higher the intensity of the incident and scattered light E field the higher the SERS signal.

As mentioned before, EM enhancement is the main contribution in overall SERS enhancement, and it is a result of the excitation of SPs on a dielectric-metal interface.[99] It is often described as a two-step process, namely a local field enhancement and a radiation enhancement.[100] To further discuss this process we take SERS occurring at the surface of a metallic nanoparticle as an example (*Figure 4.2*).

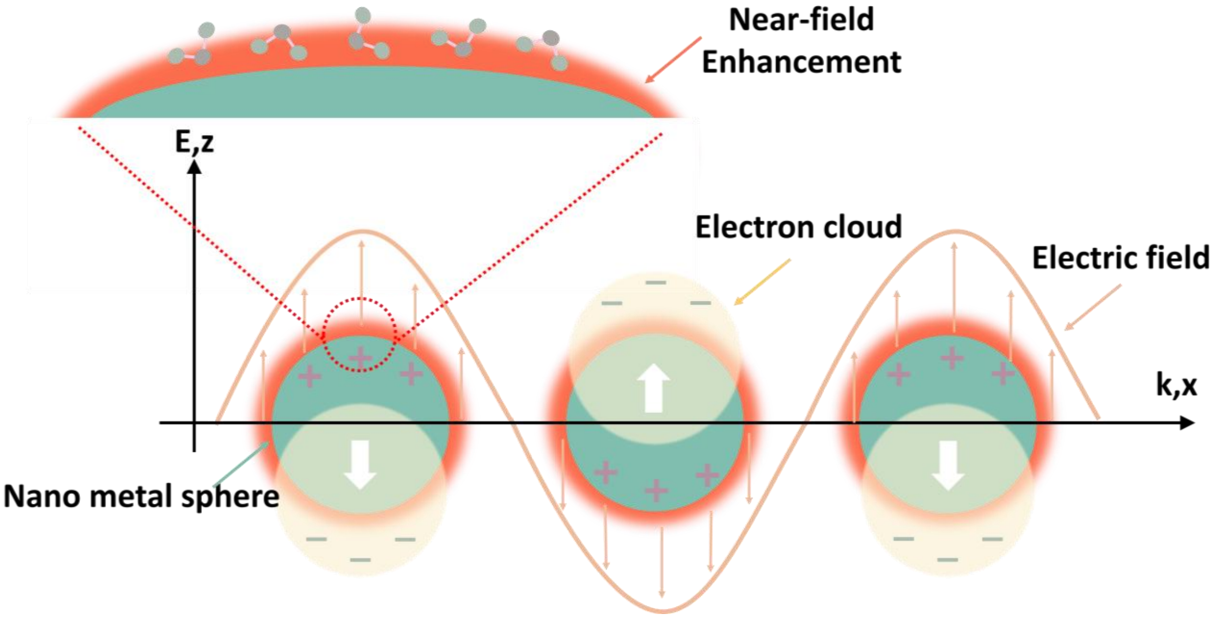

Figure 4.2: SERS induced by the excitation of LSPR at a metallic nanoparticle and air interface.

During the local field enhancement process (step 1), when excited by incident light with frequency ω_0 , an LSPR is generated at the surface of the metallic nanoparticle, which acts as an optical antenna that transfers far-field incident light to the near-field. The enhancement factor *EF₁* in this step is given by:

$$EF_1 = \frac{|E_{local}(\omega_0)|^2}{|E_0(\omega_0)|^2} \qquad \mathit{4.1.2}$$

Then in the radiation enhancement process (step 2), the metallic nanoparticle again acts as an optical antenna, but in contrast to step 1, it transfers near-field scattered light to far-field, and the enhancement factor EF_2 in this step is given by:

$$EF_2 = \frac{|E_{local}(\omega_\mathrm{R})|^2}{|E_0(\omega_\mathrm{R})|^2} \qquad \mathit{4.1.3}$$

Knowing that the Raman-shift only amounts to a very small fraction of the incident photon energy, we can approximate that the incident light frequency ω_0 equals that of scattered ω_R. Thus as a result, the total EM enhancement factor $\mathrm{EF}_{\mathrm{EM}}$ is given by:

$$EF_{EM} = EF_1 \cdot EF_2 \approx \frac{|E_{local}(\omega_0)|^4}{|E_0(\omega_0)|^4} \qquad \mathit{4.1.4}$$

Recall from previous section we have defined g factor as the enhancement of *E* field, thus:

$$EF_{EM} \propto g^4 \qquad \mathit{4.1.5}$$

This is commonly known as the fourth power of EM enhancement in SERS.[101]

It should be pointed out that SERS enhancement resulted from molecules locating in-between two plasmonic particles could be extremely large, as depicted in *Figure 4.3*.[102] The two particles form a dimer with a nanogap between them. This nanogap is often referred to as a ‘hot spot’, which signifies that it is highly efficient in amplifying near-field optical signals and it is characterized as presenting a greatly enhanced EM field.[94,103] This is due to the strong electromagnetic coupling of the two particles in the dimer. In this case $\mathrm{EF}_{\mathrm{EM}}$ is highly dependent on the size of the nanogap, and under the right conditions can be as high as 10^{11}, high enough for potential application in single-molecule detection.[104,105]

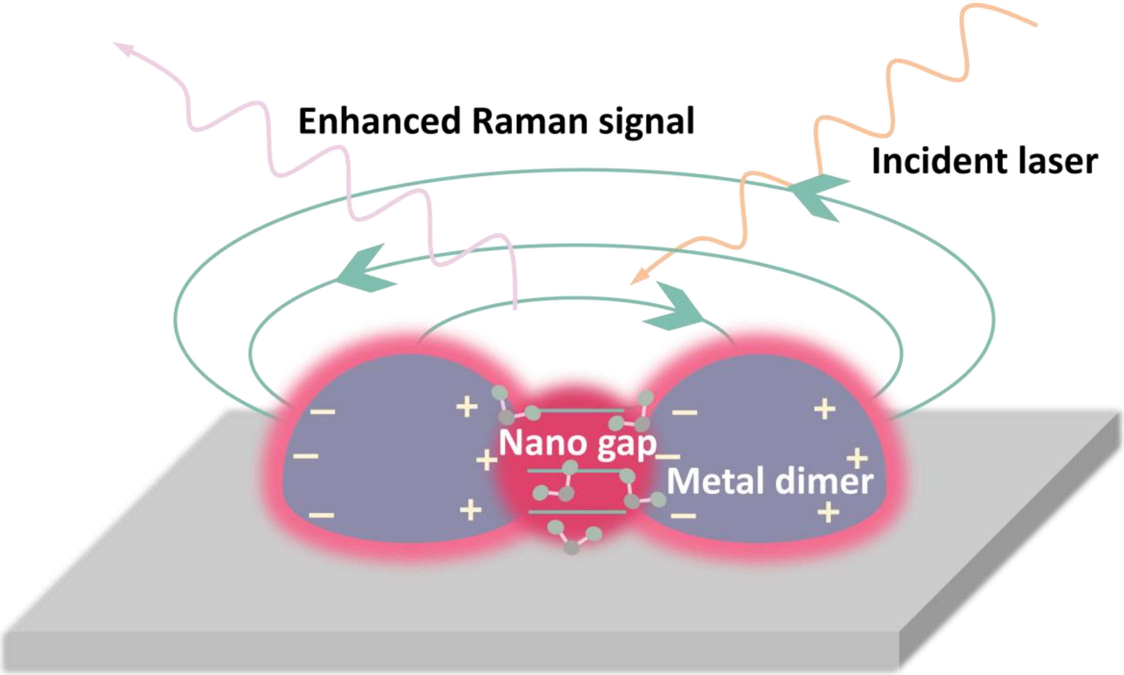

Figure 4.3: A dimer formed by two plasmonic nanoparticles separated by a nanogap, in which the signals of molecules locating in between are significantly enhanced.

Thanks to the huge enhancement provided by SERS, it offers the possibility to overcome the intrinsic low Raman scattering cross section. However, SERS still relies on a conventional optical microscope, thus its spatial resolution is inevitably limited by the diffraction limit introduced earlier to a couple hundreds of nanometers, which is no better than the conventional Raman spectroscopy.[106]

5 Tip-enhanced Raman spectroscopy (TERS)

5.1 Brief history

After acknowledging the technical drawbacks and spatial resolution limitation of SERS, various studies have been conducted in attempt to modify this technology into single-point SERS, in which instead of adopting a roughened metallic surface to generate plasmonic 'hot spots', a single plasmonic nanoparticle was used for *E* field enhancement as an optical antenna.[106] The pioneer work in this direction was a concept introduced by Wessel in 1985 in which he proposed surface-enhanced optical microscopy (SEOM).[107] SEOM benefits from a strongly enhanced field generated through plasmon resonance as well as lightning-rod effect from a single plasmonic nanoparticle. Then this plasmonic nanoparticle could be precisely controlled via scanning probe microscopy (SPM) thus making single-point light enhancement possible. Furthermore, Wessel also pointed out that that the single-point enhanced light could be confined to the very vicinity of the plasmonic nanoparticle, thus would be capable of detecting as well as measuring optical signal such as Raman, two-photon, or second-harmonic from the minuscule volume (even down to nanometer scale) of a sample right beneath the nanoparticle. In theory such technique would provide high spatial resolution as well as strong field enhancement. Together with the rapid development in SPM, the stage was set for the implementation of Wessel's proposal.[108] Fourteen years later, in 2000, four separate groups, Zenobi, Kawata, Anderson, and Pettinger,[109–112] independently published the first Raman measurements at nanoscale achieved by coupling an inverted optical microscope with SPM (three groups with AFM and one with STM) in which a nanoprobe either fully plasmonic or coated with plasmonic metal was used to locally confine and enhance a light field. In analogy to SERS, as in this case the enhancement results from a tip instead of a surface, this technique was named a tip-enhanced Raman spectroscopy (TERS) by Zenobi's group. By combining the chemical sensitivity of conventional Raman spectroscopy with the high spatial resolution of SPM, TERS as a novel characterization technique, has demonstrated its capability to obtain topography and its corresponding spectral information from various types of samples simultaneously with high sensitivity and spatial resolution way below diffraction limit. As an emerging and relatively new characterization technique, TERS has gradually become a routine table-top tool and is applied to a wide range of research fields, such as chemistry, physics, biology, material science etc.

5.2 Technical aspects

As pointed out earlier, TERS combines the chemical sensitivity of conventional Raman spectroscopy with the high spatial resolution of SPM. Thus its set-up is an integration of confocal Raman system with SPM, which requires a careful design of optical pathways as well as precise feedback controls to guarantee a successful TERS measurement. Furthermore, properties of the sample under study (such as conductivity, transparency etc.) also need to be taken into consideration. The following sections will be focused on the introduction as well as comparison on the different optical geometries and scanning probe microscopy (SPM) feedback controls commonly used in TERS.

5.2.1 Optical geometries

The four most widely used TERS optical geometries are shown in *Figure 5.1*. Each of those geometries can be adopted based on the specific requirements imposed by the sample under study.

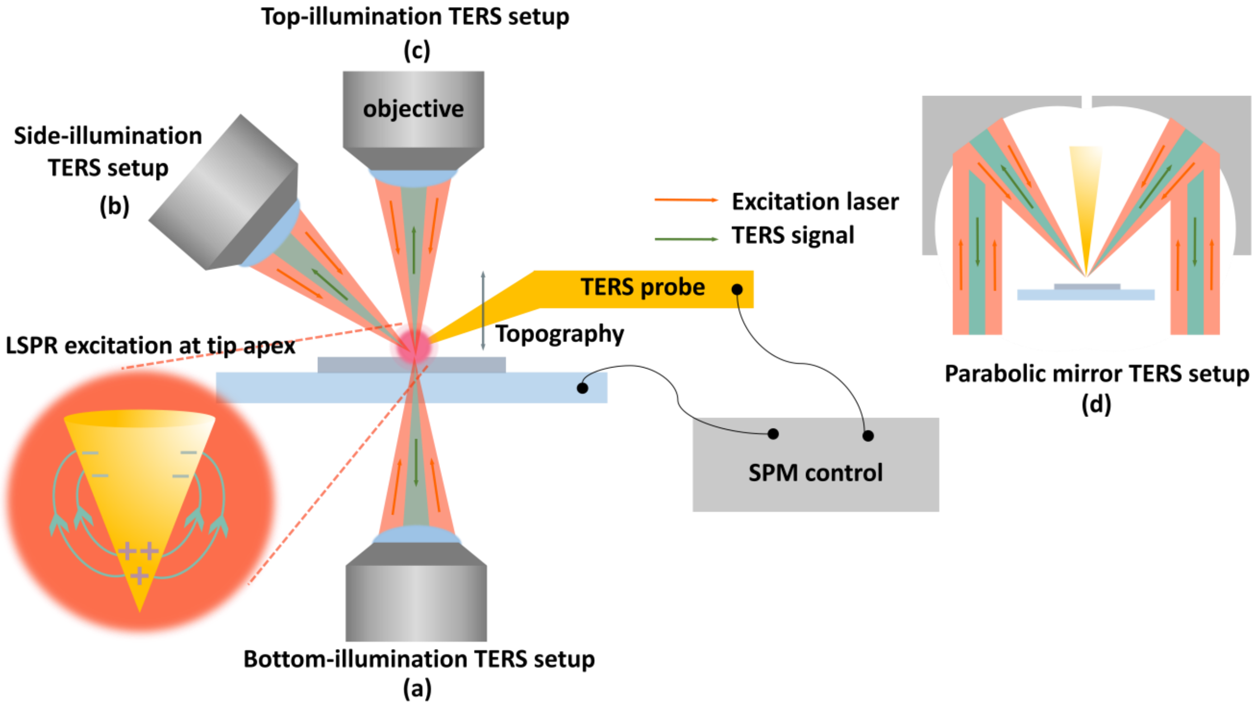

Figure 5.1: Illustration of the four most commonly used TERS optical geometries. (a) bottom-illumination (b) side-illumination (c) top-illumination (d) parabolic mirror illumination.

Recall from the section on the brief history of TERS, four groups successfully conducted TERS independently for the first time, and all of them were conducted in bottom illumination configuration (*Figure 5.1*(a)).[109–112] In this configuration, the sample under study is placed on a transparent sample holder, such as glass, thin mica, indium tin oxide (ITO) or gold thin film. A laser is focused at the tip apex from the bottom of the sample and holder and the same objective is used for introducing incident laser and signal collection, from two opposite directions. In this configuration, an oil-immersion type objective with high NA (≥ 1.4) can be used, which leads to a tight focus, thus results in a more confined laser energy and a smaller illuminated background area, both ideal for optimizing signal collection. Furthermore, a solid angle of up to 140° can be achieved which significantly increases efficiency of enhanced Raman signal collection for short integration time. This configuration is especially suitable for applications in bio-sample studies.[113] However, the first limitation of this configuration is that for obvious reasons it can only be used for transparent samples while the second limitation relates to the light polarization in the plane of the sample, which is less than ideal to efficiently excite a localized surface plasmon resonance on the tip.

In order to overcome these limitations of bottom-illumination configuration, side-illumination TERS (*Figure 5.1* (b)) was developed, and firstly introduced in 2001.[114] In side-illumination configuration, the incident laser is focused to the tip apex from the side via an objective with long working distance and smaller NA (0.28~0.7) at an angle typically between 45–70°, but partly up to grazing angles of 87°.[115,116] The enhanced Raman signal is collected confocally with the same objective. Thus in this configuration, samples as well as substrates are no longer limited to being transparent. Conducting substrates may provide so called gap-mode enhancement between the charges on the tip and the virtual mirror charges below metal surface forming a virtual dipole/dimer configuration around the sample of interest. [113] This gap-mode (an enhancement factor of 100) usually overcompensates the loss of scattered photons due to the smaller NA of the objective in this configuration. Furthermore, in side-illumination one can control the polarization of the incident laser along the tip axis to more efficiently couple with LSPR, thus leading to stronger enhancement. A drawback of this configuration is that due to the angle between the focal plane and the sample surface the laser focus is non-symmetric and further enlarged to approx. 2–3 µm which results in a comparatively large far-field background as well as reduced efficiency in excitation and collection, which can partly be compensated by higher energy input from incident laser.[113,117]

Besides side-illumination, a second alternative to study opaque sample on non-transparent substrate as well as to benefit from gap enhancement is top-illumination configuration (*Figure 5.1* (c)). It was firstly introduced in 2001 by Sun et al.[118] It has the benefit to work on opaque samples but suffers from a lack of polarization control and a partial obstruction of the optical path by the tip.[113] In this set-up, the sample surface is illuminated perpendicularly by incident laser along the tip axis from top. The NA of objective in this case is between side and bottom illumination and can be as high as 1. It also allows the application of objectives with larger working distance. In general, compared to side-illumination the confocal background is reduced via a tighter focus. The main disadvantage of this configuration is that the tip is in the light path of incident laser and Raman collection. An objective with a high NA can be used to compensate for this blockage. Furthermore, the tip is typically tilted with an angle of approximately 45° to the sample surface normal.

With respect to the polarization control for bottom- or top-illumination, several teams have explored the benefits of radially polarized light that provides a longitudinal polarization in the focal spot, thus facilitating the excitation of an LSPR. Another option is to obstruct half of the optical beam perpendicular to the polarization direction. While the first technique requires additional optical components that jeopardize the stability of the alignment, the second technique reduces the effective aperture of the objective and drastically deforms the Gaussian intensity distribution of a TEM00 beam profile in the focal spot.

All three above mentioned TERS optical configurations rely on refractive optical elements to focus light efficiently. For the 4th case of TERS set-up, parabolic mirrors with a high NA can be used to focus light by reflection. This parabolic mirror illumination configuration was firstly realized by Debus et al in 2003.[119] Upon illumination, incident laser is reflected to the parabolic mirror focal spot. A NA as high as 1 can be achieved which then allows for a wide detection angle of as large as 180°. However, in practice, the strong susceptibility to coma aberrations impose severe demands on the optical alignment.[120] Moreover, the sample size is also restricted in this configuration, given that the light has to pass around the sample to reach the parabolic mirrors so that the sample has to be either transparent or relatively small in size (<5 mm). Larger parabolic mirrors can be used but making the whole process more complex and difficult due to the high precision necessary to keep the NA close to 1.[113]

5.2.2 SPM feedback control

Enhancement of Raman signal in TERS is strongly confined to the close vicinity of the tip apex, where size of the enhanced EM near-field is in the range several nanometers. Due to this relatively small dimension of the enhanced field, a precise control and stabilization of the tip-sample distance is of great significance to TERS measurements, and is realized via the scanning probe microscopy (SPM) feedback part of the system. SPM alone is commonly used to measure surface topography and properties with resolution and precision down to atomic scale thus is especially suitable for the precise control of the tip-sample distance in TERS.[121] The three most commonly used SPM feedback controls in TERS are beam-deflection atomic force microscopy (AFM), scanning tunneling microscopy (STM) and shear force tuning fork microscopy (*Figure 5.2*).

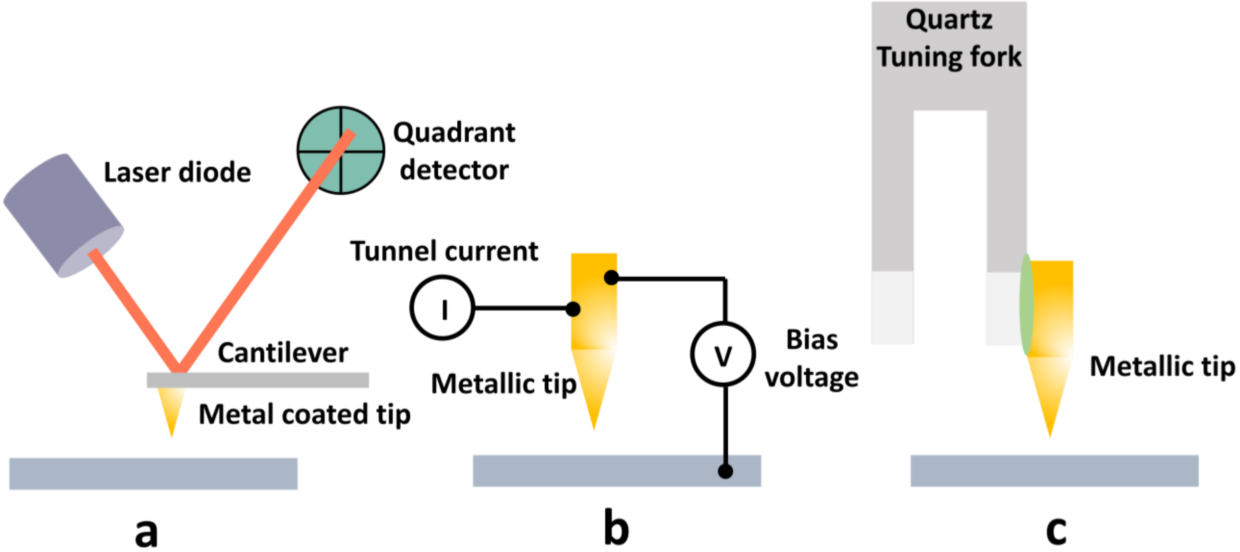

Figure 5.2: Illustration of SPM feedback controls for TERS. (a) Atomic force microscope (AFM); (b) Scanning tunneling microscope (STM); (c) Shear force tuning fork microscope.

For AFM modulated TERS, the control of tip movement is either in contact mode, with the tip of the cantilever in physical contact with the sample; tapping or intermittent mode, which means that the tip is periodically hammering the surface as it oscillates with an amplitude of typically several tens of nanometers and non-contact mode, in which the short-range forces near the surface (e.g. van der Waals) are exploited to provide a feedback about the tip-sample distance. The motion of the cantilever as it follows the topography of the sample is monitored via a laser deflected from the backside of the cantilever. TERS tips used in this configuration are noble metal-coated cantilevers, which enables the control and manipulation of coating material, thickness and the radius of the tip apex, as well as the resonance wavelength of the tip to ensure a stronger coupling with the incident laser.[106,113] There are several challenges associated to this technique: First of all, the cantilever obstructs a large solid angle otherwise useful for excitation and detection. Second, the Raman laser tends to interfere with the laser-based detection scheme for the detection of cantilever deflections thus destabilizing the feedback control for the tip-sample distance unless particular care is taken e.g. by distinct wavelength ranges for both lasers. Third, for the case of contact and tapping mode AFM, the use of ductile noble metals such as gold and silver as plasmonic nanoantenna results in excessive tip wear and extremely short lifetimes. And last but not least, the relatively large oscillation amplitudes compared to the reach of the optical near field result in the near field being out of interaction with the sample surface for most of the oscillation cycle. The following two methods overcome this problem.

For STM modulated TERS, a conductive tip is scanned relative to the surface of the sample within tunneling distance, which is in the range of 1 nm.[122] This distance is especially preferable for TERS since it is within the distance required for potential gap enhancement and is kept at an almost constant value based on the feedback mechanism of the STM. Furthermore, the tips used in STM configuration TERS are fabricated from bulk metal wire (often from electrochemical etching process) which in comparison are less expensive and less complicated than the metal coated cantilevers used in AFM-TERS. However, due to the intrinsic requirements of STM, only conductive samples and substrates can be used, which in turn limits the optical geometry capable to be coupled with to side-illumination, whose limitations have been discussed in the previous section.

The third type of TERS SPM feedback control is via shear force tuning fork microscopy. In this configuration, a noble metal TERS tip made of an electrochemically etched noble metal wire is glued to a prong of a quartz tuning fork which laterally vibrates near its resonance frequency in the proximity of the sample surface. The sample-tip interaction is monitored through the resonance frequency shift induced by damping. Despite the success of this technique and its ease of use, the nature of this damping mechanism is still not fully understood.[123] It is worthwhile mentioning that the lateral vibration direction is perfectly well suited to maintain an almost constant tip-sample distance. [124] Shear force tuning fork control for TERS does not pose any requirements on the sample and thus can be coupled with all types of optical geometries. The tips used in this configuration are similar to those in STM-TERS which are fabricated from bulk metal wires, making them relatively affordable compared to beam deflection cantilevers. The disadvantage of this set-up is the relatively arduous tip cutting and gluing process which makes the whole process more time-consuming and more prone to tip damage due to the complex handling process that will be described in the following section.

6 TERS tip

As mentioned earlier, optical nanoantenna is defined as a structure which is capable of converting far-field EM radiation to near-field (or the other way around).[55] In TERS, the optical nanoantenna is the main component which is used to overcome the diffraction limit as the source of the enhancement. Thus the tip is considered the core element in TERS as it dominates the enhancement of the signal and also determines the spatial resolution. Currently, facile fabrication of reliable and reproducible TERS tips is the bottleneck for further development and application of TERS. In this section, I will raise a brief discussion on TERS tips, from the material, fabrication techniques to the lifetime and protection issues.

6.1 Tip material

Similarly to SERS, TERS enhancement mainly comes from the plasmonic *E* field enhancement effect generated from SP resonance. Currently, TERS tips are most commonly fabricated from gold and silver due to their high free electron density, low damping and thus strong LSPR effect in the visible range as well as their relatively high chemical stability. Recall the complex nature of dielectric constant introduced in previous sections, high free electron density results in its real part to be negative, which results in strong *E* field enhancement. For metallic nanoparticles, in the visible range, the SP resonance is only achievable when the real part is < 2.[125,126]. As a result, for most metals this is only possible within and beyond the infrared range, with the few exceptions including Au (~ 500 nm), Ag (~ 365 nm), Cu (~ 350 nm), Pt and Al (both in UV range).[38,126–128] The imaginary part on the other hand, represents the absorption of light which leads to energy loss thus ideally should be as small as possible. The real part and imaginary part of Au and Ag are shown in *Figure 6.1*.[129,130] The imaginary part of Au is relatively small in the red visible range thus when coupled with red laser (~ 600 nm), tips made from Au are capable of generating strong *E* field enhancement. In comparison, the imaginary part of Ag is comparatively smaller than Au within the complete visible range. When coupled with green laser (~ 500 nm), Ag tips can produce an even stronger *E* field enhancement than gold. However, in ambient conditions Ag is far more susceptible to irreversible contaminations and oxidation due to its chemical reactivity.[131] Thus Ag tips are more popular in ultra-high vacuum TERS experiments or in conventional TERS after chemical stabilization. In comparison, Au is significantly less chemically active in ambient condition, and Au TERS tips have a lifespan of up to months compared to that for Ag TERS tips (lifespan of a few of hours). However, the ductility of gold makes it prone to tip-wear and tip deformation during scans.

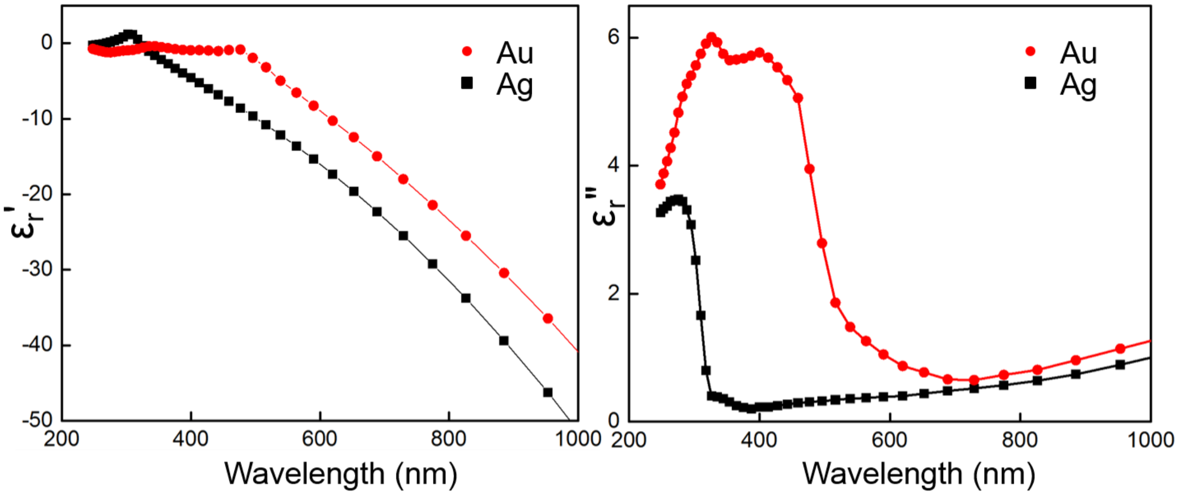

Figure 6.1:Complex permittivity of gold and silver in the UV-visible range. Real (left) and imaginary (right) parts of as a function of wavelength.

Aside from Au and Ag, Titanium Nitride (TiN) has also been acknowledged as a promising material for TERS tip in recent years due to its similar optical properties to that of Au, robust physical properties (resistance to thermal and mechanical degradation), chemical stability as well as its ability to act as a diffusion barrier.[132–135] At the moment TERS tips with TiN coating have an enhancement factor significantly lower than that of Au and Ag.[133] Nevertheless its high plasmonic tunability still makes it a promising candidate as TERS tip material.

6.2 TERS tip fabrication techniques

As mentioned earlier, the three most commonly used SPM feedback controls are AFM mode, STM mode and shear force tuning fork mode. Thus different types of tips are chosen in accordance to the SPM mode. In short, for STM, a highly conductive tip is required to guarantee a tunneling current. For AFM, cantilever tips are required for the feedback control and they are often coated to achieve better reflectivity. For shear force tuning fork there is no special requirement for tips that can be used as long as they can be readily attached to the tuning fork. As far as the application for TERS is concerned, the tip material also has to provide an LSPR. Herein, a non-exhaustive list of TERS tip fabrication techniques will be introduced under the three classes of SPM feedback modes.

6.2.1 STM TERS tips

Given that the tip used in STM is required to be conductive, STM TERS tips are most commonly made form bulk metal wires. However, the simplest STM fabrication technique of a cutting metal wire is not applicable for TERS as the tip apex generated is often highly irregular and not reproducible.[129] The most widely used technique for the fabrication of STM TERS tip is via electrochemical etching of bulk metal wires. It is most commonly adopted due to its cost-efficiency and the high quality tips fabricated.[136] An example of Au wire electrochemical etching process is illustrated in *Figure 6.2*. During a typical electrochemical etching process, a metal wire and a counter electrode are immersed inside an etching solution and connected to a power source, where both direct current and alternating current can be used. The wire-etchant interface, known as the meniscus is where the tip is formed. The most widely acknowledged etching mechanism is known as the 'drop-off', in which after a certain amount of etching, the lower part of the wire can no longer be supported by the upper part and drops into the etchant, and thus a tip is formed.[137,138] In order to avoid over-etching to guarantee a small tip radius, a cut-off circuit is often used to promptly abort etching process after the lower part is dropped.[139] The biggest drawback of this technique is the requirement to optimize numerous free parameters that can influence the properties of the tips fabricated. Such parameters include: etching solution (material, concentration, viscosity etc.), counter electrode (material, shape, position etc.), voltage profile (DC/AC, intensity, frequency, duty cycle etc.), etching time, bulk metal wire (thickness, crystallinity, immersion depth etc.) and so on. Thus it is extremely difficult, if not impossible to control and optimize all parameters, which requires considerable amount of trial and error studies. Fortunately, at the moment there already exists recipes with enough optimization which is capable of providing high quality TERS tips (*Figure 6.3*).[139–142] Given all the parameters that can be tuned, electrochemical etching for the fabrication of TERS tips is among the most promising techniques of all and is also abundant in potentials.

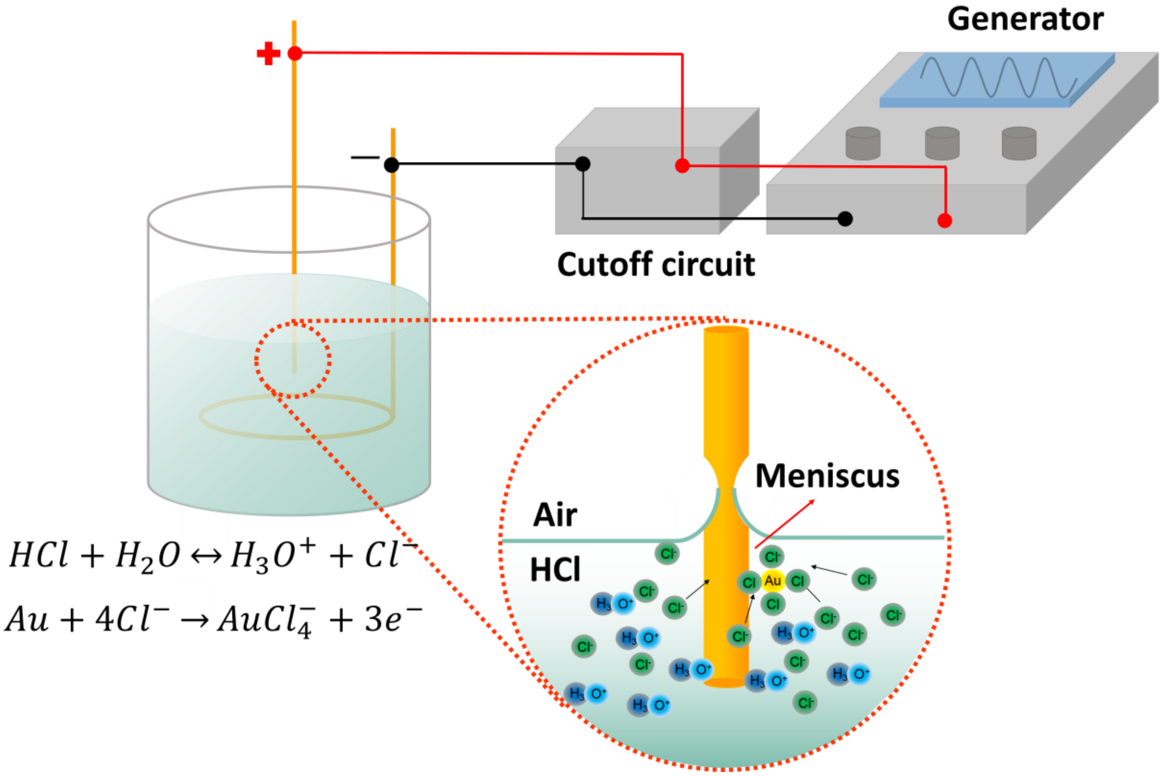

$$HCl + H_2O \leftrightarrow H_3O^+ + Cl^-$$

$$Au + 4Cl^- \rightarrow AuCl_4^- + 3e^-$$

Figure 6.2: Illustration of electrochemical etching procedure for the fabrication of Au TERS tips

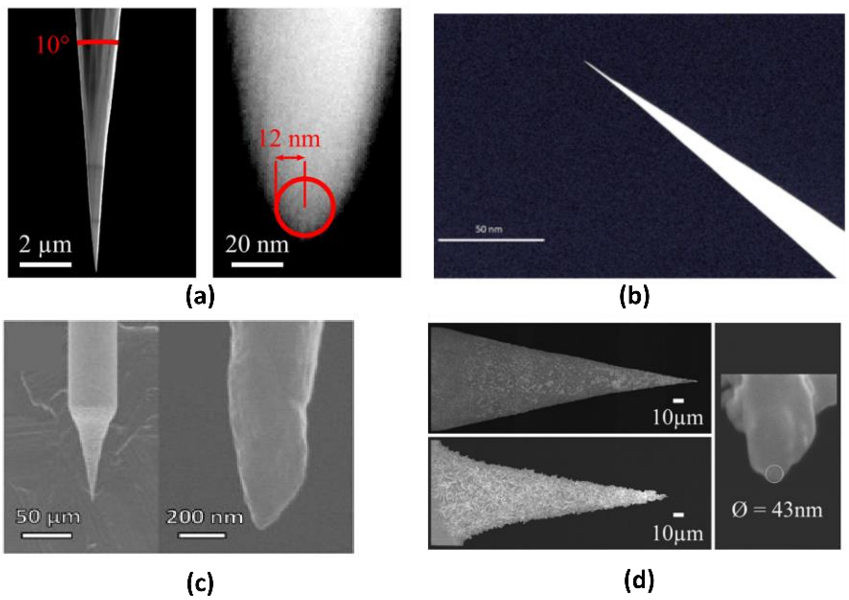

Figure 6.3: SEM of electrochemically etched Au tips (a) (b) and Ag tips (c) (d) which show small tip radii and opening angle, as well as relatively smooth surface.139–142 © 2018 Author(s). © 2016 John Wiley & Sons, Ltd. © 2011 American Institute of Physics.

Furthermore, after the electrochemical etching process, focused ion beam (FIB) has been adopted to further modify surface features on the tip in order to control and optimize its LSPR properties.[126] For example, nano-gratings can be added to the surface of tips as plasmonic waveguide, in which the SPPs can be generated and propagate toward the tip apex (*Figure 6.4* (a)).[143] The advantage of these grating embedded TERS tips is that the plasmon excitation point is away from the tip apex thus during interaction with sample under study the only contribution to the signal is from near-field enhancement with very little to no far-field signal in the background.[10] FIB can also be used to modify the structure of the tip by creating a groove near the tip apex which acts as an EM cavity, which results in 'resonance tips' with well-defined and highly tunable LSPR properties (*Figure 6.4* (b)). Given that tips are a consumable, the additional expenses associated to the use of FIB processing need to be considered.

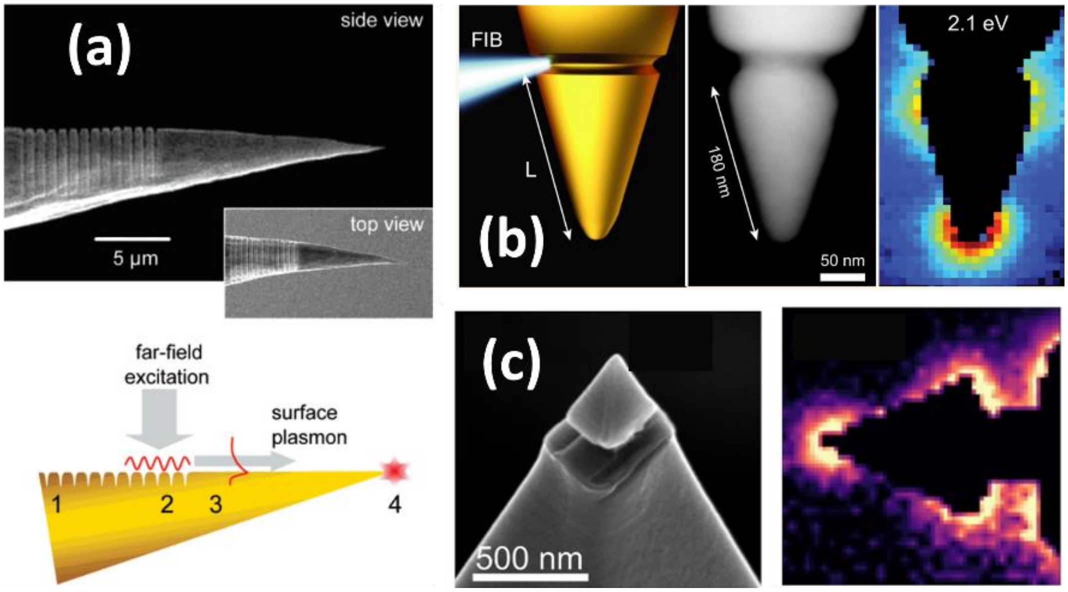

Figure 6.4: Illustration of FIB-modified TERS tips: (a) with nano-gratings as plasmon waveguide (b) (c) with nano-groove close to the apex as EM cavity for tunable LSPR properties.143 © 2007 American Chemical Society

6.2.2 AFM TERS tips

For AFM TERS, cantilever-based tips are required. The most common technique to fabricate AFM TERS tips is via deposition of plasmonic metal particles onto commercially available silicon oxide or silicon nitride cantilever. Such deposition can be achieved either via physical deposition or chemical deposition.

Some typical examples are shown in *Figure 6.5*.[144–147] The main drawback of this process is the limited reproducibility of the optical properties of tips manufactured due to the broad distributions of size and shape of noble metal nanoparticles.[126]

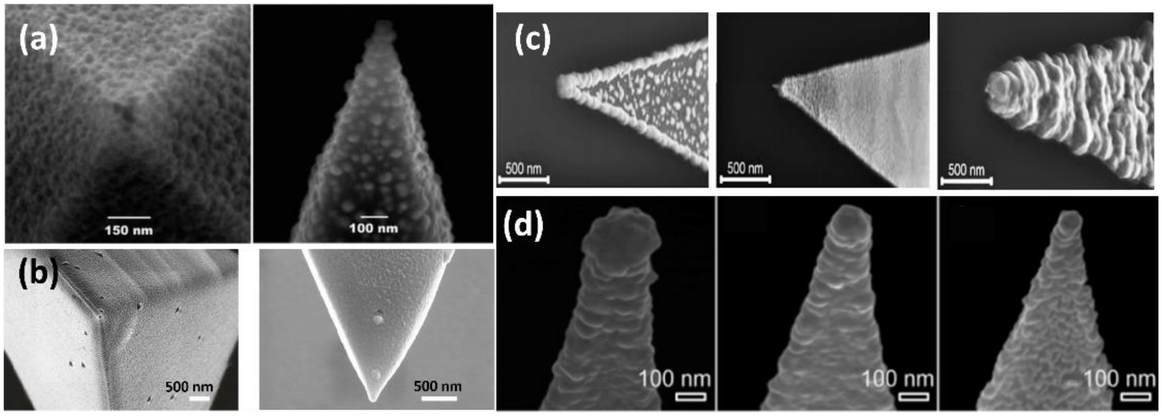

Figure 6.5: AFM TERS tips fabricated via physical deposition (a) (b) and chemical deposition (c) (d) in which plasmonic noble metal nanoparticles are deposited onto commercial AFM cantilevers.144–147 © 2012 John Wiley & Sons, Ltd. © 2010 Society for Applied Spectroscopy © 2015 OSA

Furthermore, the so-called 'resonance tips' with groove near the tip apex which acts as an EM cavity used in STM TERS can also be achieved for AFM TERS with the application of FIB as well (Figure 6.6).[148] Similarly to the TERS tips with grooves used in STM mode, such AFM TERS tips are highly tunable in plasmon resonance which can be used to optimize TERS enhancement by better coupling with the incident laser.

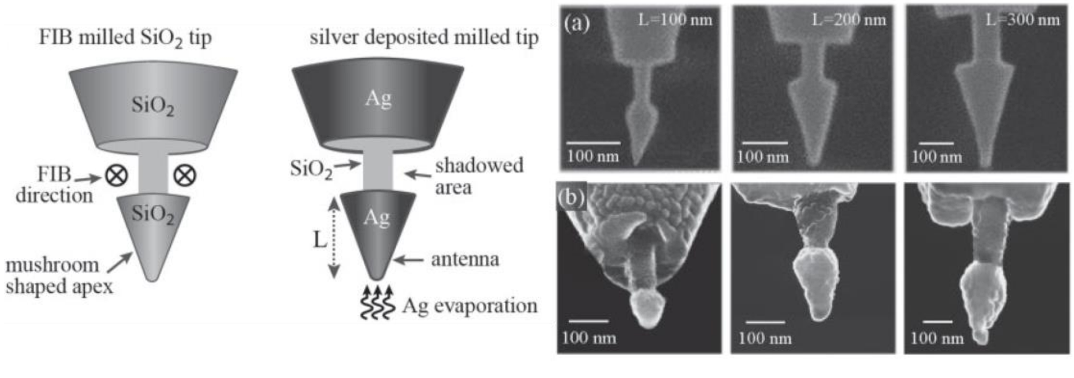

Figure 6.6: Fabrication of AFM TERS tips with grooves via FIB.[148] © 2015 The Japan Society of Applied Physics

Aside from the above mentioned AFM TERS techniques, various types of non-standard AFM TERS tips have been fabricated by means of attaching of nanoparticles to a commercial

AFM cantilevers or micro fabrications.[129] However such processes are by far time-consuming and complex in manipulation, which still requires further study and development thus will not be introduced here.

6.2.3 Shear force tuning fork TERS

Shear force tuning fork TERS has the least requirements on plasmonic metal tips as long as they can be attached onto a tuning fork. Thus in principle all tips suitable for SPM TERS that have been introduced in the previous section can be adopted in shear force tuning fork TERS. Some care is required about the mass of the wire and the glue to fix it to the prongs as high masses and soft glues will have a strongly adverse effect on the quality factor of the tuning fork.

6.3 TERS tip lifetime

TERS enhancement is primarily dependent on the plasmonic properties of the tip. Thus chemical and mechanical degradation of tips should be carefully monitored and controlled to guarantee successful and reproducible TERS measurements. Ag is relatively chemically active compared to Au, in ambient conditions various reactions with sulfides, sulfates, chlorides, and oxides from the atmosphere can occur and contaminate the surface of the Ag tips which leads to a dramatic loss in enhancement.[149] The lifetime of Ag tips is typically limited to several hours, or at most a matter of days before losing enhancement completely as reported in the literature.[149–152] For a contaminated tip, two modes at 220~240 cm^{-1} can be assigned to silver oxide while a mode at 960~970 cm^{-1} is related to the silver sulfite (Ag_2SO_3) and silver sulfate (Ag_2SO_4).[131,153–156] Besides, during TERS mapping, the apex of TERS tips is prone to mechanical wear i.e. the plasmonic nanostructures will deform or detach. Also due to plasmonic local heating effect may induce decomposition of organic compounds (typically results in amorphous carbon residues which have a Raman signature above 1300 cm^{-1}). All above mentioned issues leads to fluctuations in TERS signal, reduced enhancement and poor reproducibility.

To cope with these issues various techniques have been adopted to protect TERS tips and to prolong their plasmonic lifetime, such as protective coatings, electrochemical reversal, controlled storage environment etc. Some common protective coatings include sell-assembled monolayers (SAMs),[157,158] SiO_x,[151,159,160] Al_2O_3,[161,162] AlF_3,[157]. However, it should be noted that better protection with thicker coating and less enhancement factor must be delicately balanced, given that thicker coatings inevitably lead to an increase in tip radius which results in a decrease of the field enhancement.[156] For tips that are already contaminated, electrochemical reversal, ionic beam cleaning can be adopted to recover the activity.[149,152] Furthermore, based on a study on the influence of the storage environments (ambient, vacuum, and nitrogen) on the lifetime of Ag tips, in ambient conditions, the lifetime is only about 8 hours whereas it extends to a few days when stored in vacuum and can also be further extended to 5 months in nitrogen glovebox.[150] Additionally, various studies have demonstrated the merits of conducting TERS measurements in ultra-high vacuum environment, such as a significantly improved tip lifetime and a higher stability of the tip-sample junction as well as minimized tip contamination.[156,163–165] This advantage needs to be balanced with the additional experimental complexity of operation in a UHV environment which limits the capability to tests/exchange multiple tips without breaking the vacuum and also voids the possibility to operate with high NA objectives for the collection of a large solid angle as none of these objectives are compatible with UHV conditions.

6.4 TERS tip enhancement mechanism

The mechanisms of EM (physical) enhancement and charge transfer (chemical) enhancement in SERS have been introduced in the previous sections. Similarly, in TERS, the enhancement mechanisms can also be rationalized by these two contributions. The chemical enhancement originates from the short-range interactions between the sample molecules and the plasmonic tip apex. During scanning process, different forms of tip-sample interactions occur which leads to variations of the peak position as well as the intensity of Raman signatures as a result of minute fluctuations in the local chemical environment.[166,167] The chemical enhancement can be categorized into the following contributions:[166]

1) Non-resonant contribution such as ground-state interactions between molecule and tip apex.
2) Resonant contribution originating from excited-states of molecules close to the incident laser wavelength.
3) Charge-transfer contribution originating from charge-transfer processes of: tip to molecule, substrate to molecule, simultaneous tip and surface to molecule, and tunneling charge transfer between tip and substrate.[168,169]

The main physical enhancement mechanisms originating from TERS tip are illustrated in *Figure 6.7*.[126]

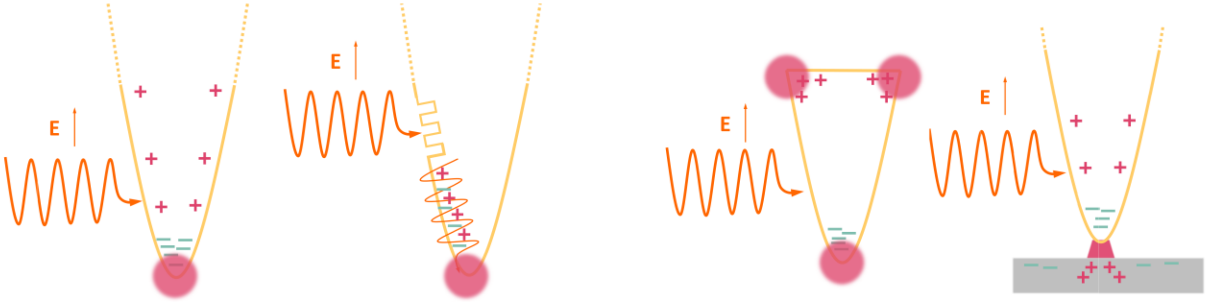

(a) Lightning-rod effect **(b) Surface plasmon polariton** **(c) Localized surface plasmon resonance** **(d) Gap mode**

Figure 6.7:Illustrations of four main types of physical enhancement at the TERS tip apex.126

The electrostatic lightning-rod effect (*Figure 6.7* (a)) is non-resonant, and is induced by geometric singularity (corner or edge) that upon illumination from an external EM radiation field leads to a highly localized surface-charge density and thus generates an enhanced E field at the apex of the tip.[126,144,170,171] Its contribution to total TERS enhancement depends primarily on the morphology of the tip surface as well as electrical conductivity of tip material at the frequency of incident EM field which drives the surface charge density.[126,172] A second source of TERS enhancement originates from the activation of SPPs or LSPR via incident laser (*Figure 6.7* (b)(c)) that follows the Raman 4th power rule, similarly to that in SERS. Additionally, in the case where the sample under study is “sandwiched” between the tip and a metallic substrate or on top of a metallic nano particle, gap mode TERS (also denoted as double tip TERS in some cases) can be obtained (*Figure 6.7* (d)).[126,173] In gap mode TERS, when the tip is irradiated with an E field polarized parallel to its axis, an oscillating electric dipole is generated at apex, and when brought to the very proximity of a metallic substrate or nanoparticle, an image dipole with accumulated opposite mirror charges is induced. The extremely localized and intense EM field within the gap can then be used as a nano-sized light source for TERS which significantly increases the overall signal enhancement.[174] Influence of the substrate material on gap-TERS can be referred to the work of Johannes Stadler et al.[174]

7 Exprimental

The TERS system, an AIST-NT OmegaScope, in this thesis is illustrated in *Figure 7.1*. The AFM (SmartSPM, AIST-NT) is confocally integrated with a Raman spectrometer. The sample scanner system has a mechanical range of 5mm × 5mm × 18mm as well as a more precise piezoelectric range of 100μm × 100μm × 15μm with a closed-loop accuracy of 0.1nm. The SPM feedback control is stabilizing the resonance frequency of the tuning fork (Quartz, AB38T-32.768kHz, Abracon Corporation) in shear force mode via amplitude control for forks with typical quality factors above 2000. The TERS tips are fabricated within our group via electrochemical etching of bulk metal wires and then glued to the tuning fork by UV glue (NOA68, Norland Optical Adhesives). The frequency stability of the tuning fork with the glued tip is correlated to the quality factor (ref PhD thesis Nicklaus for details) and typically 0.02 Hz/min.[213] This implies that, over the duration of a long scan of approximately one hour, the tip-sample distance might slightly vary, in the range of 0.25 nm or less.

The optical geometry of our system is side-illumination mode with a 0.7 NA objective (Mitutoyo Inc.) with an inclination angel of 65° (to that of the tip axis). The side objective sits on a piezoelectric scanner which moves the focal spot in three directions by 30 μm × 30 μm × 12 μm with precision down to nanometer. In order to match the plasmon resonance of gold tips, a linearly-polarized, helium-neon laser (25-LHP-928-249, CVI Melles Griot) with 632.8 nm wavelength is chosen as the excitation beam for Au TERS tips and 533 nm for Ag, and is controlled by an optical preparation unit (Nanofinder 30, Tokyo Instruments Inc.). The laser power can be varied from 10 mW to 10 μW by a neutral density filter. The laser diameter is controlled via a beam expander in accordance to the entrance pupil of the objective in use. A rotating half wave plate is used to select either vertical or horizontal polarization for the excitation laser. In the detection route within the Raman spectrometer, light is spectrally dispersed by 150/ 600/ 1800 lines/mm and is then detected by a CCD array (iDus 420 BU, Andor Technology) which operates at -80 °C (cooled by Peltier elements) in order to reduce thermal noise. The CCD array has a pixel resolution of 255 × 1024, and translate to a spectral resolution of approximately 2 cm^{-1}/pixel over a spectral range of 0 cm^{-1} to 1800 cm^{-1} at 600 lines/mm grating with excitation at 632.8 nm wavelength. The cut-off of the Semrock RazorEdge filter is at 70 cm^{-1}, meaning that spectral feature closer to the Rayleigh line will be efficiently suppressed.

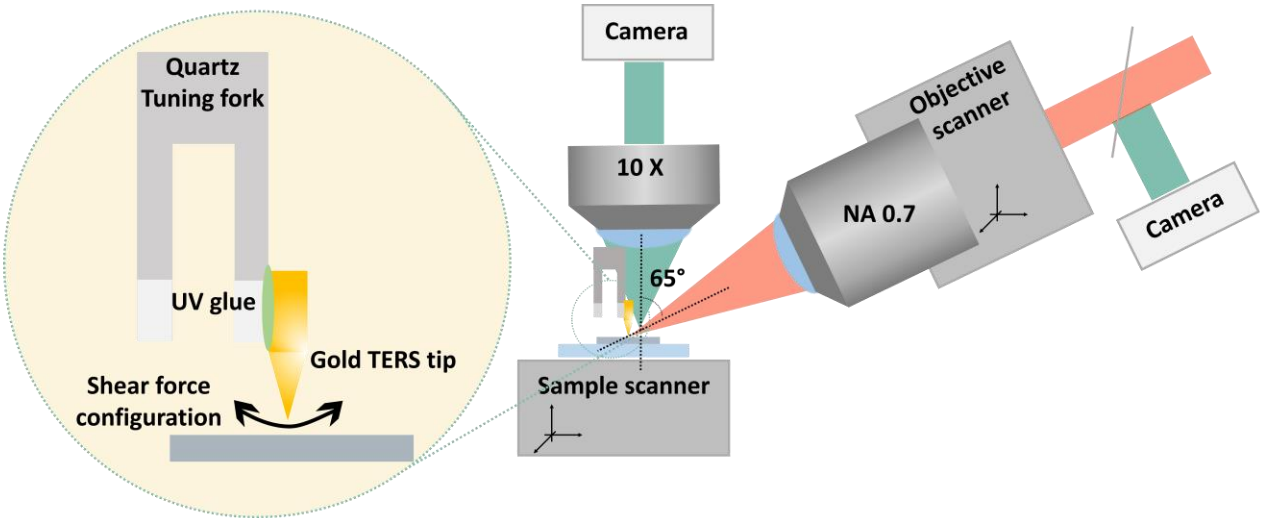

Figure 7.1: Schematic of TERS setup used in this thesis.

8 Silver TERS tip fabrication

As previously pointed out in section 6.1, given that the imaginary part of Ag is comparatively smaller than Au within the complete visible range, when coupled to laser with appropriate wavelength, Ag tips are capable of producing stronger *E* field enhancement than Au tips. Thus the development of Ag TERS tips has always been heavily sought after.

In our group, we have already developed a mature recipe for the fabrication of functioning Au TERS tips via pulse voltage electrochemical etching, and our development for the Ag TERS tip is derived from a similar setup. The challenges of Ag TERS fabrication via electrochemical etching have long been identified by the community such as:

- Choice of etching solution, given that the chemical reactivity of Ag is significantly higher than that of Au, etchants that are capable of inducing oxidation as well as other potential contaminations should be avoided (strong acids such as perchloric acid, nitric acid, or concentrated sulfuric acid which are normally used in the fabrication of Au TERS tips).[142,175,176]
- Precise control of etching procedure to avoid over-etching which results in tips with big radii. For Au TERS tips, a cutoff circuit which monitors the change in either current or voltage is often used to stop etching promptly. The current between the etching tip and the ring electrode is Faradaic, i.e. provided by the drift of dissolved ions from the tip as they move towards the ring electrode to eventually be reduced again to metallic deposit. This Faradaic current depends on the etching rate, the charge number of the ionic species and the mobility of ions in solution. To stop the etching process, the voltage is cut off as soon as the current drops below a certain value, which corresponds to a very low etching rate as the tip is already very thin at the meniscus which leaves less and less material to be etched. The detection of this current threshold depends intimately on the experimental conditions and the etching medium chosen for the process and are much less favorable in the case of silver with lower Faradaic currents than for gold.

Besides a cut-off circuit, an optical method has also been adopted.[176] However, for most of these methods, external components need to be added into the etching set up which complicates the manufacturing process while increasing its cost.

To cope with these challenges, I have established a two-step pulse voltage electrochemical etching process for the fabrication of Ag TERS tips that does not necessitate any cut-off circuit with the etching solution being a mixture (volume ratio of 2:3) of phosphoric acid (H_3PO_4, Sigma Aldrich, 85 wt. % in H_2O) and acetonitrile (C_2H_3N, Sigma Aldrich, anhydrous, 99.8%). Phosphoric acid is a colorless, odorless, and non-volatile mild acid with neglectable oxidation capability due to its structural properties. As concentrated H_3PO_4 is highly viscous, which hinders ion transfers within, it is diluted with acetonitrile, an oxygen free solvent which is not reactive with Ag. The corresponding chemical reaction is given by:

$$2\,H_3PO_4 + 2n\,Ag + C_2H_3N \rightarrow 2\,Ag_nH_{3-n}PO_4 + nH_2 + C_2H_3N\;(0 < n < 4) \qquad 8.1$$

The electrochemical etching setup employs for the fabrication of Ag tips is illustrated in *Figure 8.1*. Based on the anodic dissolution principle, Ag tips are etched from a 0.125 mm diameter, 99.9% pure Ag wire (GoodFellow). Prior to the etching process, the wire is immersed in 2M nitric acid solution for several minutes in order to remove surface contaminations such as organic residues. It is then used as the anode which eventually forms a tip, whereas another piece of silver wire bent into the shape of a ring is used as counter electrode. A pulse voltage (high voltage of 4.5 V, low voltage of 1 V) provided by an arbitrary wave function generator is applied to the etching set up.

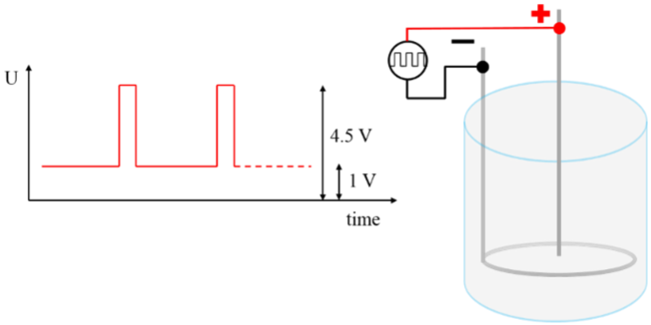

Figure 8.1: Schematic of electrochemical etching system.

As mentioned earlier, over-etching is one of the biggest challenges in the fabrication of Ag TERS tips via electrochemical etching process. This is due to several factors. For starter, in conventional etch and drop process, the tip is formed within the meniscus of the solution, where an hour-glass shape is formed (*Figure 8.2*). However, this hourglass-shaped part of the wire is within the meniscus during the etching process, which cannot be readily monitored with any optical microscope. Thus when the lower part of the wire drops into the solution over-etching already starts at the newly formed tip apex, leading to tips with undesirable apex radii. Furthermore, during the etching process, the volume ratio of phosphoric acid and acetonitrile at the meniscus changes dramatically, as acetonitrile is highly volatile and the meniscus is in fact vibrating in accordance to the pulse voltage applied. This will lead to a low reproducibility as well as ill-defined tip shape, as shown in *Figure 8.3*.

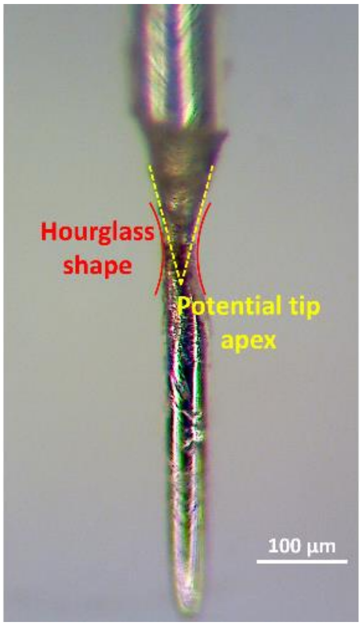

Figure 8.2: optical microscope image of a partially etched Ag wire where the hourglass shape and potential tip apex are indicated in red and yellow, respectively.

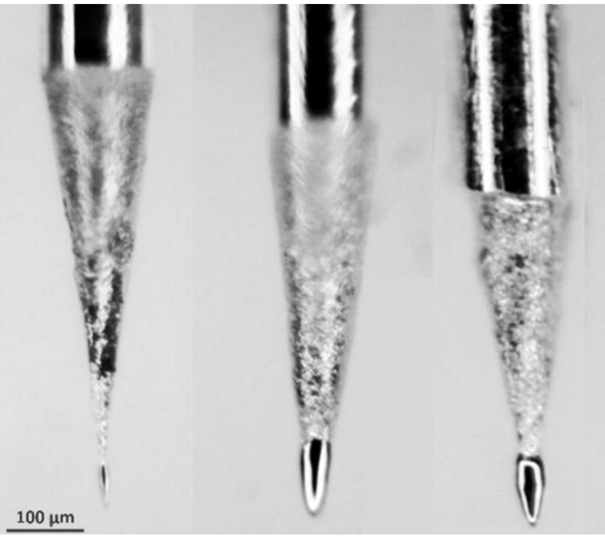

Figure 8.3: Typical optical microscope images of tips manufactured with the conventional one step etching, which show rough surface and irregular tip apex.

In order to cope with this issue without the need for other complicated components added to the setup such as a cut-off circuit, I developed a new etching process consists in two main steps, depicted in *Figure 8.4*. In order to guarantee proper monitoring towards the end of the etching process, instead of leaving the tip to be formed in the meniscus, in this new process it is formed deeper inside the etching solution. After the electrochemical etching, the Ag tips are cleaned in pure acetonitrile for ~10 s to remove undesired contaminations and etchant residues resulting from the etching process that would deteriorate the Raman enhancement. Pure acetonitrile was chosen since it is an oxygen free solvent of the acid.

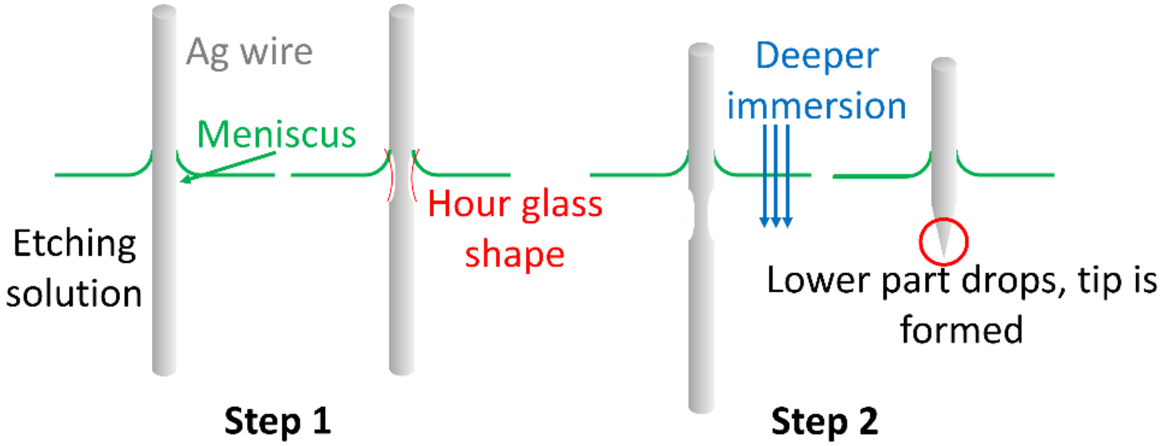

Figure 8.4: Schematic of two-step etching process: Step 1: The silver wire is etched for 4 minutes to form an hourglass shape before cutting the pulse voltage. Step 2: With the aid of an optical microscope, the silver wire is immersed deeper into the etching solution, so that the hourglass shape of the silver wire produced by the drop of the meniscus is lower than the air-solution interface. The etching is then resumed until a sharp tip with a nanoscale radius of curvature is obtained.

To be more specific, in the first step, the Ag wire is immersed into the etching solution and due to surface tension, a meniscus is formed around the surface of the wire. When the etching starts, the wire's shape changes due to the drop of the meniscus, to resemble that of an hour glass. This hour glass shape is of great significance to the second step in which the tip is formed. Time optimization shows that it takes ~5 min for the lower part of the wire to drop from the meniscus. Therefore, the etching time of the first step is set to last 4 minutes to guarantee an hour glass shape. This first step corresponds to ~80% of a complete etching process. Prior to the second etching step, the pulse voltage is switched off and the wire is further immersed into the solution that the previously etched part is completely submerged inside the solution. The pulse voltage with a decreased duty cycle is then switched on to resume the etching. The etching process is monitored through an optical microscope, and when this second etching is very close to end, a third more reduced duty cycle with is applied, and the etching is stopped manually when the lower part of the wire fell into the solution.

Table 8.1: Duty cycles used in the fabrication of Ag TERS tips

Step 1	60 μs/330 μs	60 μs/330 μs	60 μs/330 μs	60 μs/330 μs	60 μs/330 μs
Step 2 part 1	20 μs/330 μs	20 μs/330 μs	20 μs/330 μs	20 μs/330 μs	20 μs/330 μs
Step 2 part 2	20 μs/ 30 ms	20 μs/ 40 ms	20 μs/ 60 ms	20 μs/ 80 ms	20 μs/ 100ms

Different duty cycles used in this process are chosen in order to overcome the issue of over-etching by minimizing the influence of operator reaction time (from observing the drop of the lower part to manually stopping the process) and are shown in *Table 8.1*. Theoretically speaking, when a longer cycle is applied to the etching, within the same reaction time that is required to cut off the voltage manually, less wire is etched as a result of the decrease in etching speed. Thus with a proper tuning of the cycle, we should be able to produce tips with small tip radii. However, there exists a critical radius, due to the fact that at the end of the etching process, the final shape of the tip especially its radius is governed by the competition between electrochemical etching and mechanical rupture. As the wire gets thinner at the hour glass shape position during etching, the lower part of the wire is pulling downwards by its weight thus there exists a critical radius at which the wire will break due to mechanical stress. To approximate the critical radius for the silver wire in our experiment, we perform the following calculations:

The pressure at the point of the wire which is being etched is given by:

$$\mathrm{P} = \frac{F}{A} \tag{8.2}$$

Thus:

$$\mathrm{A} = \frac{F}{P} \tag{8.3}$$

The critical threshold for plastic deformation in silver is at stresses of $100\ \mathrm{MPa} = 100\ \mathrm{N}/mm^2$.[177] The force F is the difference between the gravitational force of the silver and the force of buoyancy:

$$\mathrm{F} = m_{silver} \times g - m_{solution} \times g$$

$$= \mathrm{V} \times \mathrm{g} \times (\rho_{silver} - \rho_{solution})$$

$$\rho_{silver} = 10.49\ g/cm^3 \tag{8.4}$$

8.5

$$\rho_{solution} = \rho_{phosporic\ acid} \times \omega_{phosporic\ acid} + \rho_{acetonitrile} \times \omega_{acetonitrile}$$

$$= \frac{1.685g}{cm^3} \times \frac{2}{5} + \frac{0.786g}{cm^3} \times \frac{3}{5} = 1.146\ g/cm^3$$

The volume of the lower section of the hour glass structure of silver can be calculated via the radius of the wire and the immersion depth, denoted by *h*:

8.6

$$\mathrm{V} = \pi \times {r_{silver\ wire}}^2 \times h = \pi \times (62.5 \times 10^{-4}\ \mathrm{cm})^2 \times (10^{-1} cm) = 1.2 \times 10^{-5} cm^3$$

8.7

$$\mathrm{F} = \mathrm{V} \times \mathrm{g} \times (\rho_{silver} - \rho_{solution})$$

$$= 1.2 \times 10^{-5} cm^3 \times \mathrm{g} \times \left(10.59 \frac{g}{cm^3} - 1.146 \frac{g}{cm^3}\right)$$

$$= 1.1 \times 10^{-6}\ N$$

Inserting these values into equation 1 provides:

8.8

$$\mathrm{A} = \frac{F}{P} = 1.1 \times 10^{-8} mm^2 = \pi \times {r_{critical}}^2$$

$$r_{critical} = 60\ nm$$

From the calculations we can see that from the etch and drop procedure, the smallest tip radius that can be obtained in a controlled way through etching is approximately 60 nm. It should be mentioned that mechanical rupture is likely decreasing the effective tip radius, except for in a way that is not accessible to external control.

SEM (M Tescan LYRA 3) was performed to investigate the influence of different etching cycles on the tip. As we can see from *Figure 8.5*, with an increase of the last etching cycle, the tips manufactured do not have a significant change in morphology.

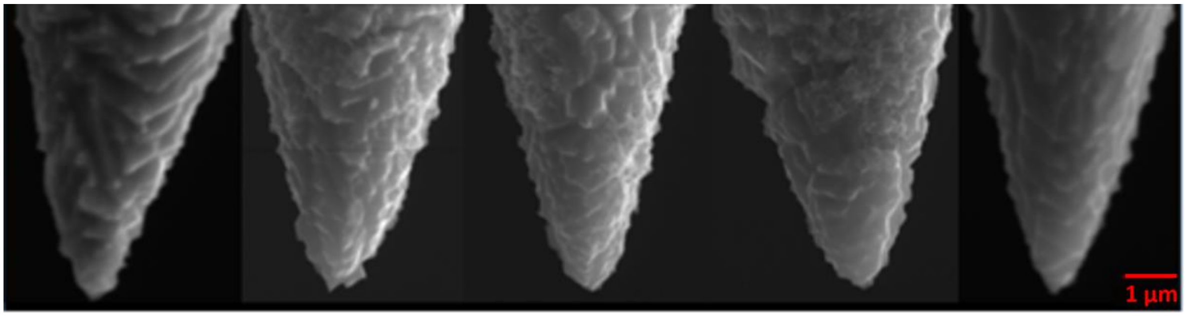

Figure 8.5: SEM images of tips manufactured with different etching cycles at the second part of step 2: (left to right) 20 µs/ 30 ms, 20 µs/ 40 ms, 20 µs/ 60 ms, 20 µs/ 80 ms, 20 µs/ 100 ms

The effective tip radii were calculated using topography maps acquired on carbon nanotubes (CNTs, commercially available) deposited on a gold substrate. *Figure 8.6* depicts a typical topography image obtained with the silver tips manufactured with our technique. As we can see, highly resolved topographies (10 nm resolution) presenting single CNTs can be obtained. This attests to the potential of our silver tips for the acquisition of high-quality topography images and optical images below the diffraction limit. A tip radius of 11 nm was extracted from this image via an approximate model which based on the assumption of a spherically shaped tip.[178–180]

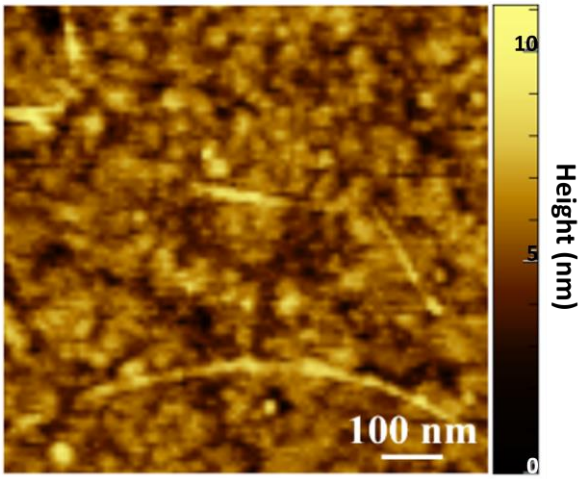

Figure 8.6: Topography of CNTs on gold substrate obtained via electrochemically etched Ag tips

Thus even though the apparent tip radii observed from SEM study are relatively large, the effective tip radii are in fact much smaller. This may seem contradictory, however it can be explained by the fact that during our fabrication procedure, granular structures of silver are formed at the surface of the tip and theses structures have sharp features which will interact with the studied sample, thus the actual tip radius is determined by those sharp features, which in most cases are smaller than the calculated 60 nm.

The optical properties and surface quality of the tips are investigated through the Raman signal of freshly etched tips, as shown in *Figure 8.7*. The Raman spectrum presented here is consistent with that previously reported and the main peak observed at ~ 250 cm^{-1} can be attributed to an Ag-O vibrational mode, as silver oxidizes in air spontaneously.[131,155] The first peak observed at ~100 cm^{-1} is not representative of the silver spectrum, most certainly a plasma line of the HeNe laser. To detect further contaminations, a long acquisition time of 60 s was used showing features extending from 1000 cm^{-1} to 1600 cm^{-1}, which can be associated to carbon deposits and others forms of silver compounds resulting from exposure to air.[131,155] For typical acquisition times in TERS measurement of 1 s, the features extending from 1000 cm^{-1} to 1600 cm^{-1} of those tips have not been observable, suggesting that the carbon deposits are sparse as they would have otherwise been amplified with the tip in feedback above the surface.

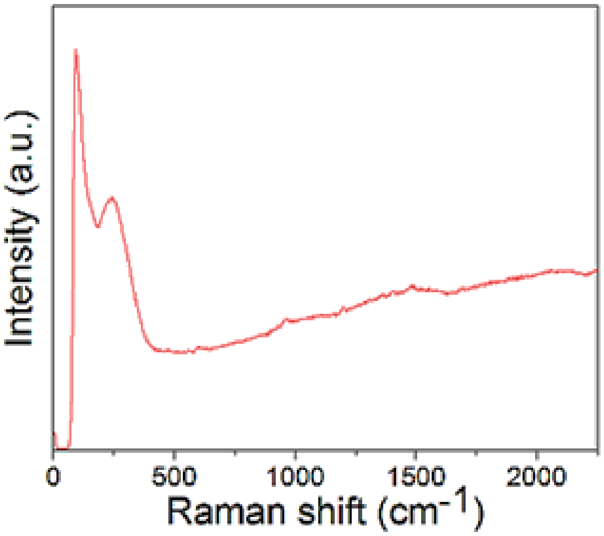

Figure 8.7: Typical Raman spectrum acquired at the apex of an etched silver tip using a 60 s acquisition time.

Thus in comparison with conventional methods, the advantages of this two-step etching are as follows: firstly, as we have mentioned before, in this procedure, no electronic equipment is needed, which simplifies the whole manufacturing procedure. Secondly, due to a faster ion transfer rate, the etching within the solution is more stable than that of meniscus, thereby ensures better tip properties such as smooth surface, well defined shape (*Figure 8.8*) as well as a higher tip reproducibility.

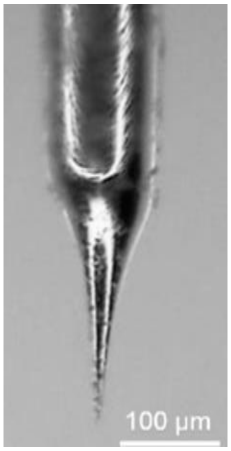

Figure 8.8: Typical optical microscope image of tips manufactured with the new two-step etching process

To verify the TERS enhancement property of the as-prepared Ag tips, the incident laser wavelength needs to be chosen appropriately to couple with the plasmon resonance frequency of the Ag tips. The plasmon resonance frequency of silver nanoparticles is a function of their geometric properties such as shape, size etc.[181] For this reason, a multi-wavelength Raman study was conducted by mapping the tip emission at the apex by a red (*Figure 8.9* (a)) and a green (*Figure 8.9* (c)) laser, two laser wavelengths commonly used for TERS experiments. When the tip is excited using a red laser (632.8 nm), a 'hot spot' can be detected at the apex of the tip (white spot, Pos. 1), as indicated by the strong emission signal with a high contrast with the background as well as the rest of the tip (Pos. 2, *Figure 8.9* (b)). The hot spot corresponds to an enhancement of the tip Raman signal by the surface plasmon.[182] Features extending from 1000 cm^{-1} to 1600 cm^{-1} can be associated to various silver compound (such as Ag_2S) photodecomposition products.[131,155] In TERS studies, this hot spot will generate an amplification of the Raman signal. However, when a green laser (532 nm) is used, no such hot spot is observed, and the signal along the tip (dark region) remains relatively uniform. This result signifies that the silver tips manufactured with our recipe are more resonant with a 632.8 nm red laser, making this wavelength more appropriate for TERS measurements.

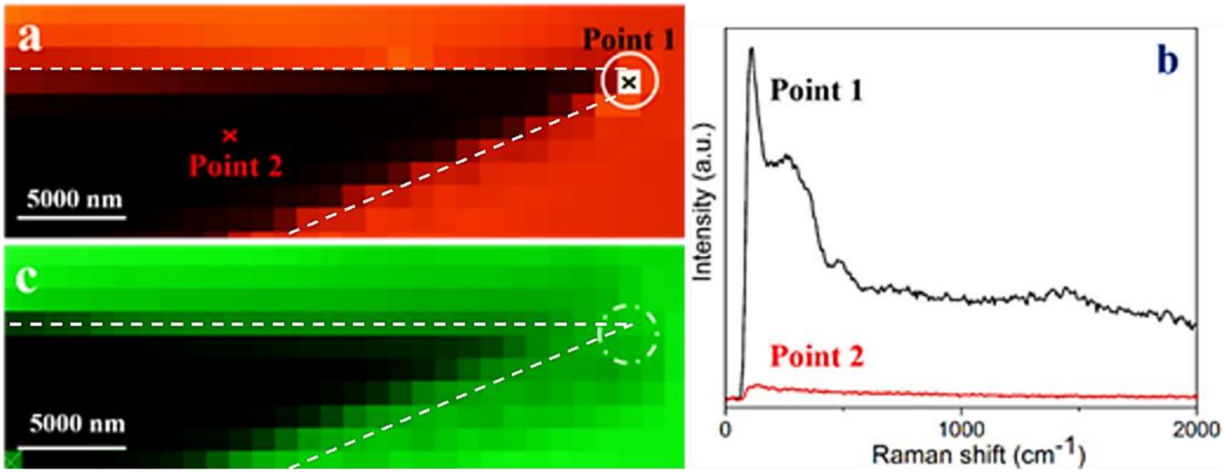

Figure 8.9: Tip Raman maps acquired with (a) a red and (c) a green laser. (b) Spectra recorded at two positions along the tip using the red laser, at the apex (Position 1) and higher on the tip (Position 2).

To assess the field enhancement properties of the Ag tips, TERS measurements were carried on a sample consisting of a monolayer of non-resonant molecules 4-Nitrothiophenol (4-NTP, Sigma Aldrich) on gold substrate. The spectra were acquired when the tip was placed in feedback with the sample (~ 1 nm for the sample surface, tip-in) and away from the sample (tip-out). A typical result is shown in *Figure 8.10*. In the tip-out configuration in which the tip is retracted from the sample surface by 5 µm, the large tip-sample distance prevents any interaction between the substrate and the tip and no significant peaks can be detected from the 4-NTP molecules. In contrast, when the tip is engaged to the surface of the sample (tip-in), a strong peak enhancement is observed. These peaks are characteristic of the 4-NTP Raman signal, attesting to the TERS amplification provided by our Ag tips.[183,184] This signal overshadows the tip luminescence. An electrical field enhancement factor (EF) of approximately 11 can be calculated according to:[185]

$$\mathrm{EF} \approx \sqrt[4]{1.22\,\frac{\lambda}{N.A.}\,\frac{1}{\sqrt{2rd}}\,\frac{\Phi_{nf}}{\Phi_{ff}}} \qquad 8.9$$

where λ is the wavelength of the incident laser, NA is the numeric aperture of the objective, r is the radius of the tip, d is the tip sample distance, Φ_{nf} is the intensity of the near field Raman signal and Φ_{ff} is the intensity of the far field signal. This is a conservative estimation of the actual enhancement factor, taking the width of the noise band of the far field as an upper limit for the intensity of the far field signal.

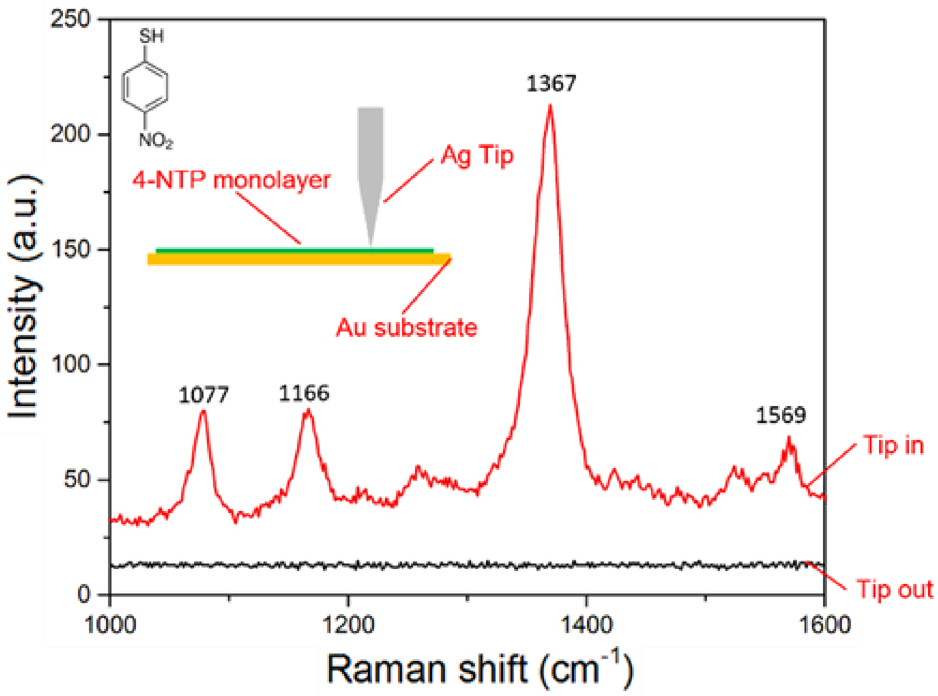

Figure 8.10: TERS of 4-NTP adsorbed on an Au substrate. The insert shows the experimental configuration.

In conclusion, we have developed a recipe for Ag TERS tip manufacturing with low contamination and good reproducibility. Using a 2:3 (volume ratio) solution of H_3PO_4 and C_2H_3N, and a two-step etching process, we avoid the need for cut-off circuits or any other method preventing over-etching, which in turn simplifies the entire manufacturing process. Optical images and topographies of CNTs show that the tips have well-defined shapes and relatively small tip radii. A tip multi-wavelength Raman study revealed that a red laser (632.8 nm) should be coupled with these tips to produce the optimum enhancement in TERS experiments. The TERS potential of our Ag tips was tested using a red laser on a sample consisting of a monolayer of 4-NTP deposited on a gold substrate. While the surface shows evidence of oxidation, carbon associated deposits are too dilute to interfere with the enhancement at the tip apex. By comparing the Raman spectra with the tip in feedback (~1 nm from the surface) and far away for the sample (~5 μm), we showed that the Ag tips manufactured by our method provide a significant Raman enhancement, as evidenced by the presence of strong 4-NTP peaks on the tip-in spectrum. A lower boundary of the electrical field enhancement factor of 11 was determined for these measurements. The etching method proposed here presents an easier, more cost-efficient approach than conventional etching processes for the fabrication of TERS active silver tips. However, at the moment there still exists several challenges of this technique:

1) Even though the reproducibility is good in terms of the macroscopic geometric properties of tips manufactured, not all tips are TERS active. The exact tip shape following mechanical rupture and the formation of sharp crystalline features is currently beyond experimental control.
2) The overall etching time is approximately 7 ~ 8 minutes, which is significantly longer than that of Au TERS tip fabrication as well as other published works.
3) The numerous nanometer scale protrusions at the tip apex is SERS active, which upon illumination, are prone to contaminations such as amorphous carbon in the atmosphere, as well as blinking effects which overweight the signal intensity of sample under study.
4) The lifetime of such Ag tips is relatively short, so far we have not been able to achieve TERS mapping with them.

Thus there's still ample room for optimizing our fabrication procedure to achieve more reliable Ag TERS tips. As mentioned in the previous chapter, there are numerous free parameters that can influence the properties of the tips fabricated via electrochemical etching such as etching solution (material, concentration, viscosity etc.), counter electrode (material, shape, position etc.), voltage profile (DC/AC, intensity, frequency, duty cycle etc.), etching time, bulk metal wire (thickness, crystallinity, immersion depth etc.) and so on. Future studies focusing on fine tuning of these parameters are required to optimize the resulted tips. Once we have established an updated recipe there are various protection techniques (introduced in previous chapter) that can be readily adopted to prolong the lifetime of Ag TERS tips.

9 TERS tip signal

During a typical TERS experiment with gold tips that are most commonly chosen for their chemical stability, a laser beam with certain wavelength matching the expected LSPR is focused near the apex of a tip, which exhibits a detectable spectrum of its own; a typical spectrum recorded on a gold tip is illustrated in *Figure 9.1*. The wavenumber at which this Lorentzian shaped curve reaches its maximum is referred to as peak position. [178,186–189] The observed spectrum of the tip signal results from two major contributions: the first being the photoluminescence of the gold tip, which is an intrinsic property of gold that can be attributed to the gold inter-band *d-sp* transitions,[190] and second being the localized surface plasmon resonance (LSPR) given it is excited by the incident laser. The gold PL spectrum has a broad feature extending to high wavenumbers, with a relatively large FWHM and within the spectral range of interest, it is broad enough to be considered locally flat. In comparison, the LSPR spectrum is narrower in the form of a Lorentzian curve. The LSPR in turn enhances the gold PL, leading to a LSPR enhanced gold tip PL which is the tip signal that we detect during experiment. During a typical TERS experiment where a gold tip is used as nanoantenna, the incident laser is focused at the apex of the tip in order to generate LSPR and create an optical near field signal. When the LSPR is induced at the tip apex, prior to landing on the studied sample, a tip signal is detectable in the spectrometer. This signal is the LSPR enhanced gold PL, and has the shape of a broad Lorentzian curve.

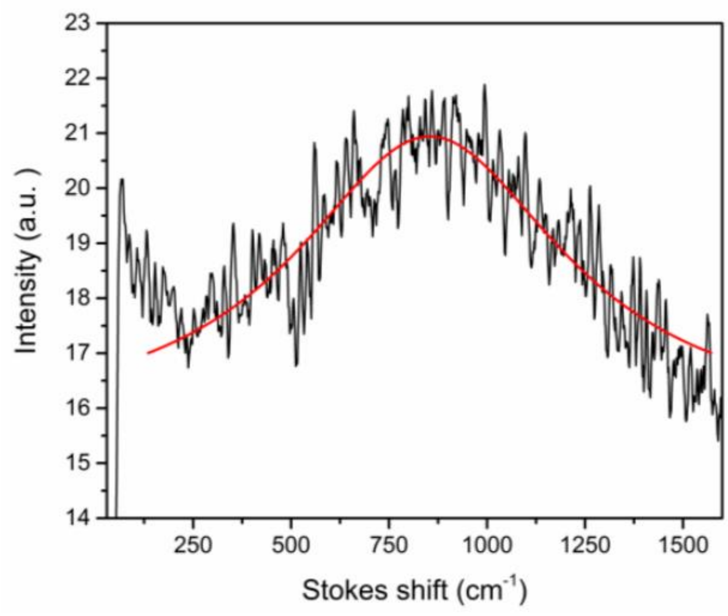

Figure 9.1: Typical gold tip signal in a TERS experiment (black) fitted with Lorentzian equation (red)

In our previous work, we have established a model to describe this LSPR enhanced gold luminescence via two separate models which consist of pure gold luminescence and LSPR. [178,191] The luminescence of gold I(ω) is induced through the direct radiative recombination of electrons from either d or sp bands, or interband transitions below the Fermi level.[190] It can be described by a function consisting of the following factors: the complex refractive index, the absorption coefficients α(ω) at ω, the incident ω0 and emitted ω photon frequencies in the form of:

$$\mathrm{I}\,(\omega) = \frac{\omega}{\alpha(\omega_0)+\alpha(\omega)}\frac{4}{(1+n)^2+k^2}\frac{1}{n^2+k^2}D^0(\omega) \tag{9.1}$$

In this equation, $D^0(\omega)$ is given by:[192]

$$D^0(\omega) = \int_{E_F-\omega_0}^{E_F-\omega} dED(E)^2 \tag{9.2}$$

where *E* is the energy, E_F the Fermi energy, and *D(E)* the d band density of states.

The LSPR *G(ω)* is given by[193]

$$\mathrm{G}(\omega) = 5|1+2g(\omega_0)|^2|1+2g(\omega)|^2 \tag{9.3}$$

where *g* is the amplification factor, ω_0 is the incident beam of frequency. The amplification factor *g* is given by[193]

$$\mathrm{g}(\omega) = \frac{\varepsilon_{metal}(\omega)-\varepsilon_{env}(\omega)}{\varepsilon_{metal}(\omega)+\chi\varepsilon_{env}(\omega)} \tag{9.4}$$

which is a function of the particle shape factor ω, the permittivity of the metallic particle ε_{metal} and that of the surrounding medium ε_{env}.

Last but not the least, ε_{metal} is described by[194]

$$\varepsilon_{\mathrm{metal}}(\omega) = \varepsilon_{\mathrm{bound-electron}}(\omega) + \varepsilon_{\mathrm{free-electron}}(\omega) \tag{9.5}$$

where $\varepsilon_{free-electron}$ is the dielectric function of the free electrons, and $\varepsilon_{bound-electron}$ is the permittivity of the bound electrons. In nanoparticles, the collective oscillation of these free electrons generates the SPR, and their dielectric function depends on the plasma frequency of gold ω_P, the electron velocity at the Fermi surface v_F, their damping constant *γ*, a scattering constant *C*, and the nanoparticle size *S*, according to[194]

$$\varepsilon_{\mathrm{free-electron}}(\omega) = 1 - \frac{\omega_P^2}{\omega^2 + i(\gamma + \mathrm{C}\frac{v_F}{S})\omega} \tag{9.6}$$

Thus the LSPR enhanced Au PL model can be obtained via the product of equation 9.1 and 9.3,as depicted in *Figure 9.2* (black and blue dash- dotted line). It can also be seen that it is in good agreement with the red curve which corresponds to the actual LSPR enhanced gold luminescence measured experimentally.[195] The abrupt cut of the spectrum at 635.5 nm is due to the fact that an edge filter was used to reduce the Rayleigh peak generated by the 632.8 nm laser by suppressing the excitation laser below 635.5 nm.

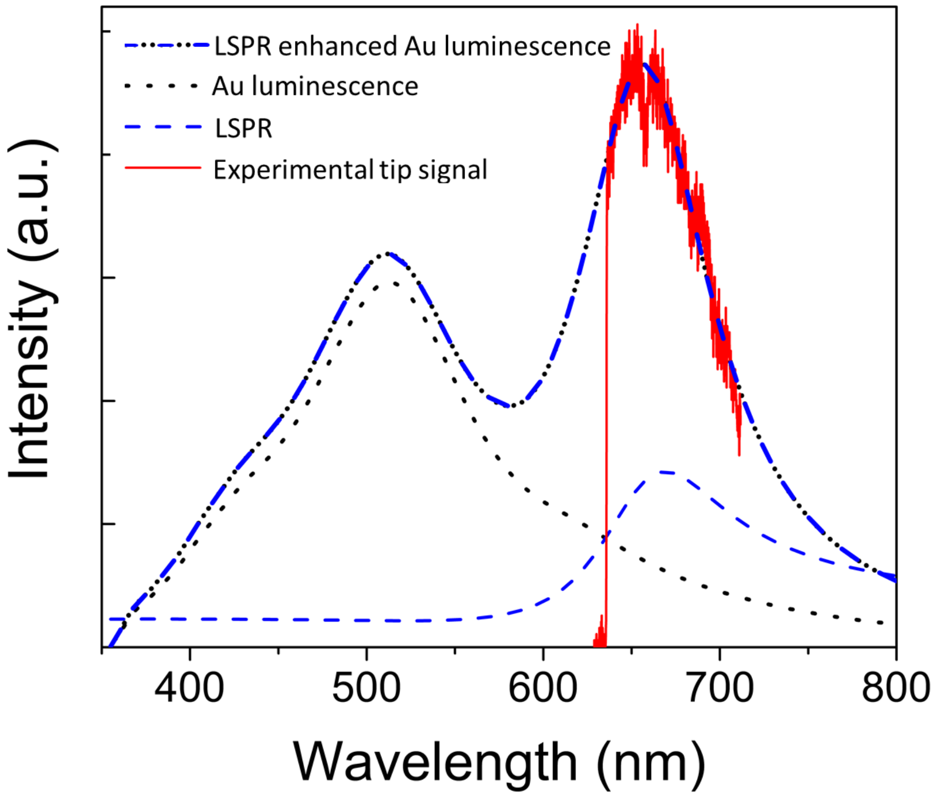

Figure 9.2: Spectra of the experimentally measured gold emission (red line), calculated gold luminescence (black dotted line), LSPR (blue) and the LSPR enhanced gold tip luminescence (black and blue dash- dotted line).195 © The Royal Society of Chemistry 2018

Ever since the first reports on tip-enhanced techniques by Domke et al. in the early 2000s, there are systematic reports on background signals near the Rayleigh line that have for long been considered a nuisance.[196] This unwanted background is in fact the tip signal which is often discarded and subtracted from the TERS spectra of the sample during data analysis in order to obtain a more accurate interpretation of the obtained Raman peak intensities. However, there is indeed an abundant amount of information embedded within this tip signal.

9.1 *In-situ* evaluation of plasmonic enhancement of gold tips for plasmon-enhanced imaging techniques via tip signal

Parts of the following section are reproduced from*: J. Zhang and A. Ruediger, In situ evaluation of plasmonic enhancement of gold tips for plasmon-enhanced imaging techniques, Rev. Sci. Instrum., 2021, 92, 053004.* My contribution to the manuscript was to identify the possibility of *in-situ* evaluation of TERS tip plasmonic property via tip signal, then gather and analyse selected tip signals, calculations based on models introduced in previous publications as well as to compose the manuscript including main text and all figures.

The core element in TERS is unarguably the tip.[129] In addition to being the source of the enhancement of Raman signals, it also determines the maximum spatial resolution that can be obtained. As such, the most critical challenge of TERS is the evaluation of the tip plasmonic property that is experienced at molecular scale in the optical near field.[197] Since the plasmonic properties depend on size and shape features that are almost always beyond the direct control of the fabrication techniques, the techniques fall into categories with different fractions of plasmonically active tips, without certainty about individual tips. In this context, early screening techniques to discriminate plasmonic against non-plasmonic tips for the respective wavelength under consideration would save tremendous amounts of time.

Herein, we introduce a facile in situ approach to evaluate the plasmonic property of the gold TERS tip without the need of sample interaction which can be readily carried out *in-situ* in preparation of a TERS experiment. This is achieved via the study of the LSPR enhanced gold PL of the gold TERS tip by means of extracting the plasmon curve from the tip signal after the tip-laser alignment. This offers valuable information on the plasmon property of a gold TERS tip which is not only crucial for the ongoing experiment but for the optimization of tip fabrication procedures, identifying tip-to-tip variability, determining tip lifetime etc. Plus, with the plasmon property obtained from our approach, it also shines light into understanding the relative intensities across a TERS spectrum, given that the plasmon at the tip apex defines the relative enhancement of different Raman modes at different wavelength.

As mentioned before, during a typical TERS experiment, when the laser beam is focused onto the apex of a gold tip, a spectrum is detected. This observed tip signal results from two major contributions: intrinsic gold PL and LSPR. In the work of G.K, a model has been built consisting two contributions which determine the spectral shape of the LSPR-enhanced gold PL to account for the experimentally obtained tip signal.[178] It should be noted that the gold PL is independent of shape or size, thus making it valid for gold TERS tips on a global scale given that the exact tip radius is not known during a TERS measurement. In other words, any changes in the LSPR enhanced gold tip PL, the tip signal, is primarily attributed to the plasmon variations such as changes in intensity, shift in plasmon position etc.

To illustrate the nature of the overall signal, we simplify the LSPR curve as a Lorentzian equation for analysis. We then decrease its intensity to 80%, 60%, 40%, and 20% of the original theoretical LSPR intensity and compute the LSPR enhanced gold tip PL by multiplying the LSPR intensity with the gold PL intensity, results depicted in *Figure 9.3*.

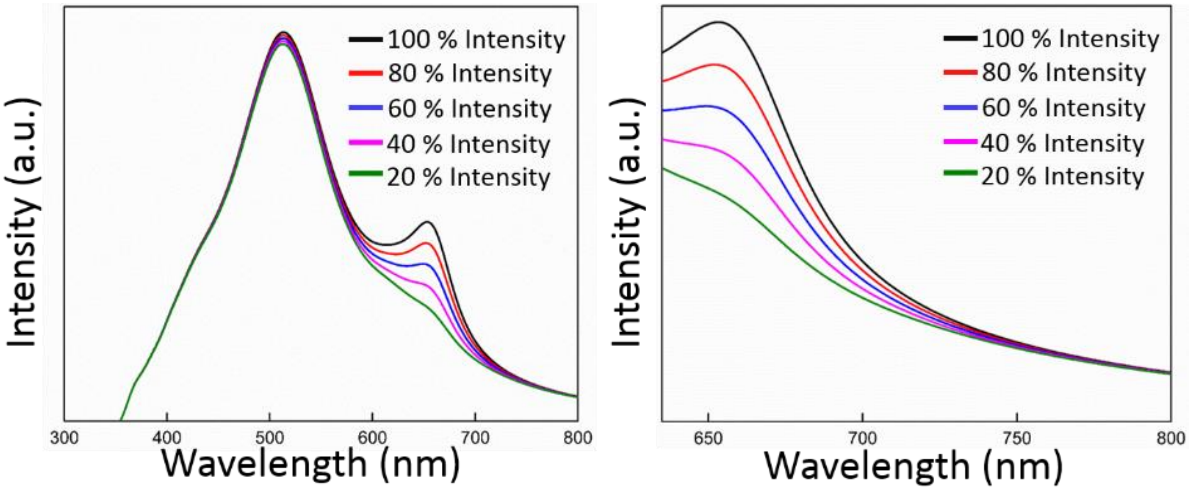

Figure 9.3: Computed LSPR enhanced gold tip PL with LSPR intensity of 100%, 80%, 60%, 40%, and 20% of a spectral range from 300 nm to 800 nm (right) and from 635.5 nm to 800 nm (left).

In most TERS set ups, an edge filter is applied (in our case 635.5 nm for Semrock LP02-633RE-25) thus the signal bellow 635.5 nm is cut from the spectrometer and will not be considered in this study. The spectral range extending beyond 635.5 nm is where the tip signal is detected and studied (*Figure 9.3* left). It is clearly seen in the figure, when the intensity of the LSPR decreases, the shape of the LSPR enhanced gold tip PL spectra, or that of the tip signal, change significantly. Furthermore, the intrinsic PL of gold is relatively low in intensity, approximately an order of magnitude above noise level. Thus, by studying the gold tip signal in situ during a TERS measurement, its plasmonic property can be explored.

Herein, we take six gold tips as examples, which were used in TERS measurements and have been proven to be non-plasmonic (tip (a) and (b)), average-plasmonic (tip (c) and (d)) and highly plasmonic (tip (c) and (f)). Each spectrum was obtained with 1s acquisition time at the “hot spot” on the tips (*Figure 9.5*), which was obtained as the result of scanning the laser focus in a plane of 10 x 10 micron containing the tip apex (*Figure 9.4*). We then use the most intense spectrum obtained in the proximity of the tip to be fitted with a Lorentzian, obtaining the results shown below:

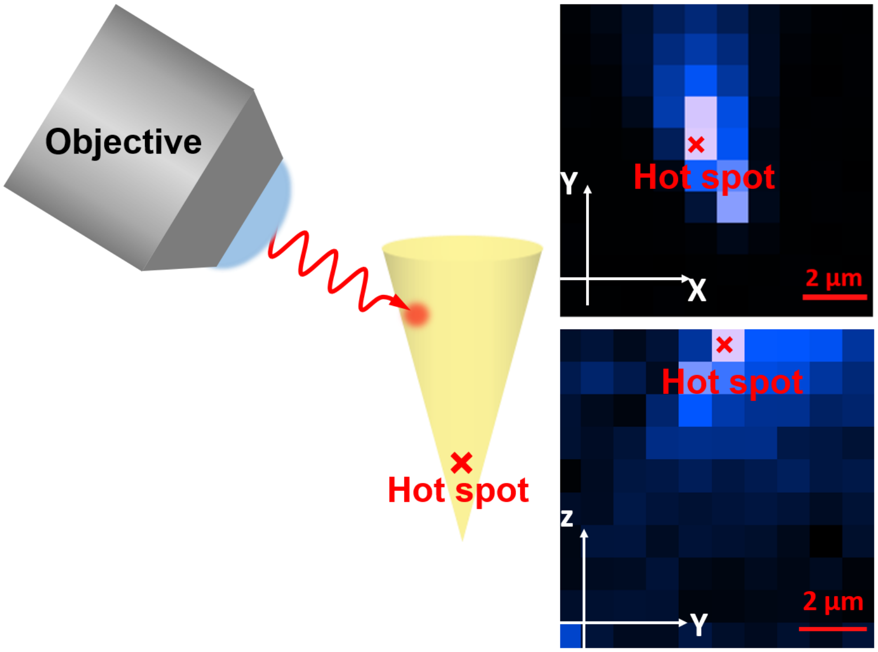

Figure 9.4: Gold tip apex mapping in the XY and YZ plane, spectra were chosen at the highest intensity point, known as the "hot spot".

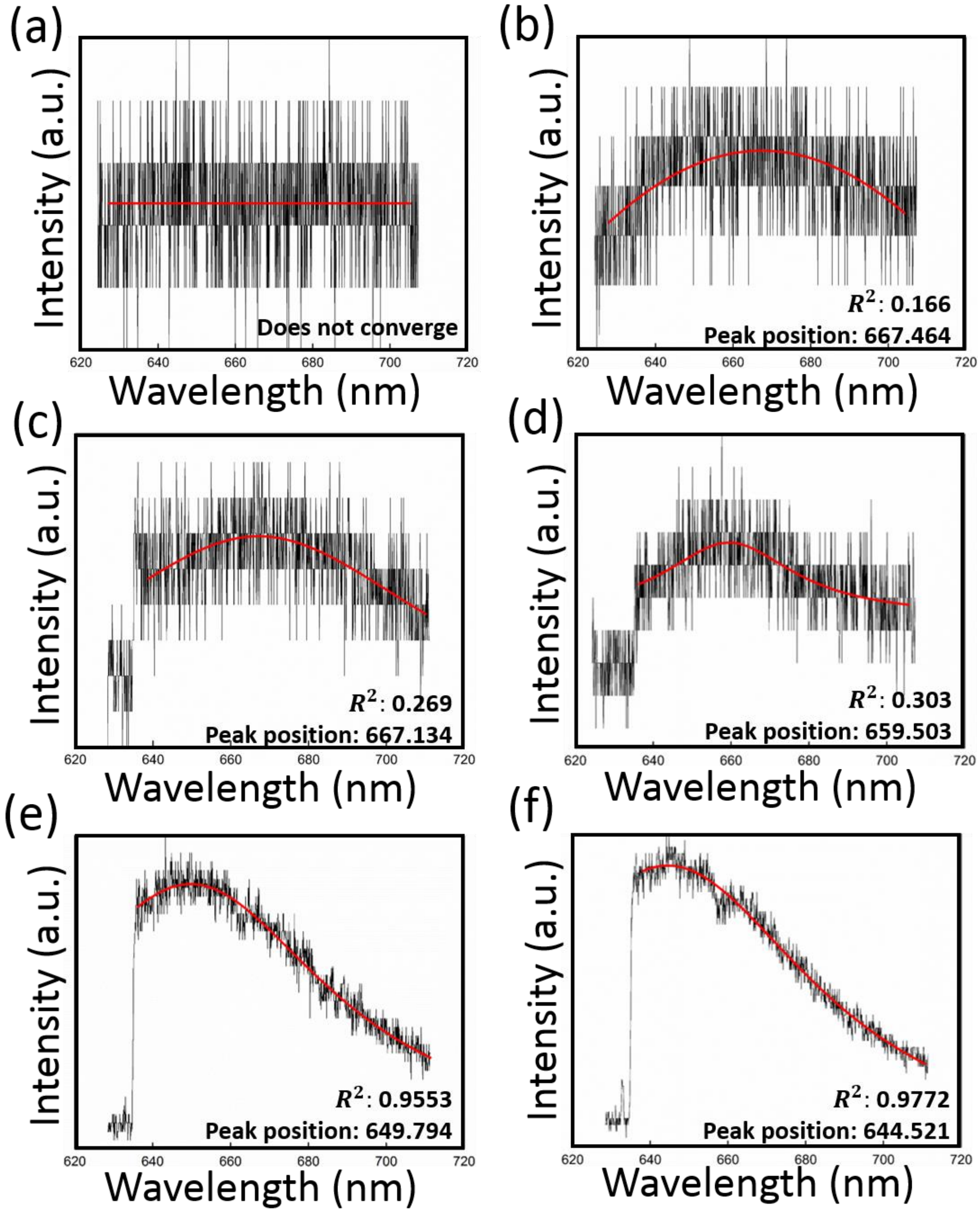

Figure 9.5: Tip signals with 1 s acquisition time (black) and the fitted Lorentzian curve (red) of :(a) (b) two non-plasmonic tips, (c) (d) two average-plasmonic tips and (e) (f) two highly plasmonic tips with the respected fitting results R^2 and peak position.

It can be observed from the *Figure 9.5* that the more plasmonic the tip (from tip (a) to tip (f)), the higher the signal to noise ratio as well as higher R^2 for the Lorentzian fitting.

This procedure can be adopted as a facile in situ evaluation of gold TERS tip plasmonic property. After tip-laser alignment where the focal spot is placed on the “hot spot” near the tip apex, by fitting the tip signal (which can be obtained with acquisition time as short as 1 s) with Lorentzian function, we can identify whether the tip qualifies for further use from the inspection of the signal to noise ratio and R^2 value. An R^2 close to 1 implies a small deviation of data points from the fit, which signifies high plasmonic property of the tip under study, which results in a higher chance of obtaining a near-field enhancement of sample under study. On the other hand, tips with R^2 value lower than 0.2 can be regarded as non-plasmonic thus unsuitable for TERS measurements, either due to an inappropriate shape or contaminations on the tip surface, which requires further treatment (such as plasma cleaning etc.) if wished to be used for TERS. Tips with R^2 value in between are still worth trying for imaging, as previous works have shown such tips can still be used to image local refractive index change with resolution as low as 10 nm even though they may not qualify for Raman enhancements.[187]

Alternative options along our line of investigations are the use of the omnipresent Rayleigh line to monitor the quality of the plasmonic tip. The Rayleigh signal however will not only include a possibly enhanced back-scattered portion but a relatively large and possibly even dominating fraction of reflected intensity that also varies with location on the sample. Ultimately, the tip-enhanced Raman signal intensity itself can serve as an alignment parameter, it however requires a previous landing and the identification of a sample on the surface in combination with the experimental capability of scanning the laser with respect to the tip while being in feedback control above the sample.

The advantage of this procedure is that it is a complete in situ process which is not limited by TERS configurations nor the type of Au tip used, as the tip signal, or the LSPR enhanced PL is an intrinsic property of Au. As a preliminary assessment of the tip plasmonic property, it is fairly simple, does not require a reference sample, and can be readily adapted into the routine of a typical TERS measurement.

9.2 LSPR position and effective refractive index of tip surrounding environment

Parts of the following section are reproduced from*: J. Zhang, G. Kolhatkar and A. Ruediger, Localized surface plasmon resonance shift and its application in scanning near-field optical microscopy, Journal of Materials Chemistry C, 9, 6960.* My contribution to the manuscript was to coordinate all contributions to the manuscript, which is a review-style document as well as the writing of the document including references.

Parts of the following section are reproduced from: *A. H. Youssef, J. Zhang, A. Dörfler, G. Kolhatkar, A. Merlen and A. Ruediger, Topography-induced variations of localized surface plasmon resonance in tip-enhanced Raman configuration, Opt. Express, 2020,* ***28****, 14161*. My contribution to the manuscript as the co-first author to the manuscript is listed below:

- Conducting near-field mapping in TERS configuration, including fabrication and selection of Au tips via electrochemical etching, tip cutting and gluing, system alignment, tip-laser alignment, system optimization and complete mapping process.
- Identifying a proper substrate (platinum) for sample preparations.
- Data analysis, in which I learnt the manipulation of the map curve fitting process (special thanks to Dr. Julien Plathier), then I started the data analysis for our near-field maps and optimized the fitting results with my colleague (Dr. Azza Hadj Youssef).
- Manuscript writing, in which together with my colleagues we composed and finalized the manuscript including the main text as well as all figures.

In a spectral range of 480–800 nm, a linear approximation of the permittivity of gold as a function of wavelength can be expressed by:[186,188,198]

$$\varepsilon_r = -0.07\lambda + 32 \qquad \textit{9.2.1}$$

where ε_r is the real part of the permittivity of gold and λ the wavelength (nm). Under resonance conditions, the permittivity then correlates to the effective refractive index of the surrounding environment at the very vicinity of the tip apex following:[199]

$$\varepsilon_r = -2\,n^2 \qquad \textit{9.2.2}$$

where *n* is the effective refractive index of the surrounding medium. Thus from the two aforementioned equations we come to the conclusion that during a TERS experiment, the position of the LSPR enhanced gold tip luminescence (detected tip signal) depends on the effective refractive index.

The influence of the refractive index on the position of the LSPR has already been studied and utilized for tuning the plasmon resonance position of TERS probes. To be more specific, given the high sensitivity of plasmonic structures on detecting refractive index variations, the plasmon position of TERS probes, especially the ones fabricated via metal deposition on a supporting material, have proven to be tunable via the coupling of underlying supporting material and the plasmonic nanostructures on top. Zenobi et al. reported a pioneering work in tuning LSPR properties of noble metal-coated TERS probe via the modification of refractive index of its base material. [200,201] They deposited materials with low refractive indices such as SiO_2 (n = 1.5), AlF_3 (n = 1.4) and Si_3N_4 (n= 2.0) onto Si (n = 4.4) probe prior to the Ag coating. In their simulation, a significant shift in LSPR position could be observed as a function of the refractive index of the underlying material. This can be attributed to the changes in effective refractive index in the optical near-field volume which lead to a shift in LSPR position. Following such concepts, numerous works have been conducted, both experimentally and numerically, on the tuning of plasmonic properties of noble metal deposited TERS tips to optimize plasmon enhancement. [193,202,203]

During a typical TERS measurement, the tip is either in contact or remains considerably close to the surface of the sample (typically 1 to 2 nm). Therefore, the dielectric environment at the tip apex consists of both air and the sample under study, making the effective refractive index at the tip apex a combination of the refractive index of air and that of the sample by a certain volume ratio. So far, we have identified two sample factors influencing the LSPR position, namely a sample material composition influence and a sample topography influence. It should be noted that in a typical TERS experiment, the sample material composition and topography influence the LSPR position simultaneously and should be taken into account at the same time.

As reported in the work of G. K, the peak position of the fitted Lorentzian curve of the tip signal discussed in previous section can be used as an estimation of the LSPR position, with deviations coming from the influence of the intrinsic PL of gold which shifts slightly with respect to crystallinity of the tip surface.[178] This paved way for the investigation of LSPR position variations with regard to sample material composition and local topography in TERS.

The sample composition influence on the LSPR position in TERS has been investigated by prior members in our group, measurements using a gold tip via aSNOM in TERS configuration were performed by Kolhatkar et al. to image the LSPR position on $Al_{0.1}Ga_{0.9}N_xAs_{1-x}$ alloy. [188] The LSPR position was obtained simultaneously with the topography, as depicted in *Figure 9.6*. A correlation was obtained between the topography and the LSPR position. In theory, the refractive indices of AlGaAs domain and AlN are 4.0 and 2.2 respectively, which corresponds to a difference of 1.8.[204,205] This difference in refractive index leads to a variation in refractive index of the medium surrounding the tip apex when scanning on different areas on the sample, where the effective refractive index decreases in area mainly composed of AlN, inducing a shift to lower wavenumbers in the LSPR position, consistently with equation 9.2.1 and 9.2.2, which is in agreement with the results obtained experimentally.

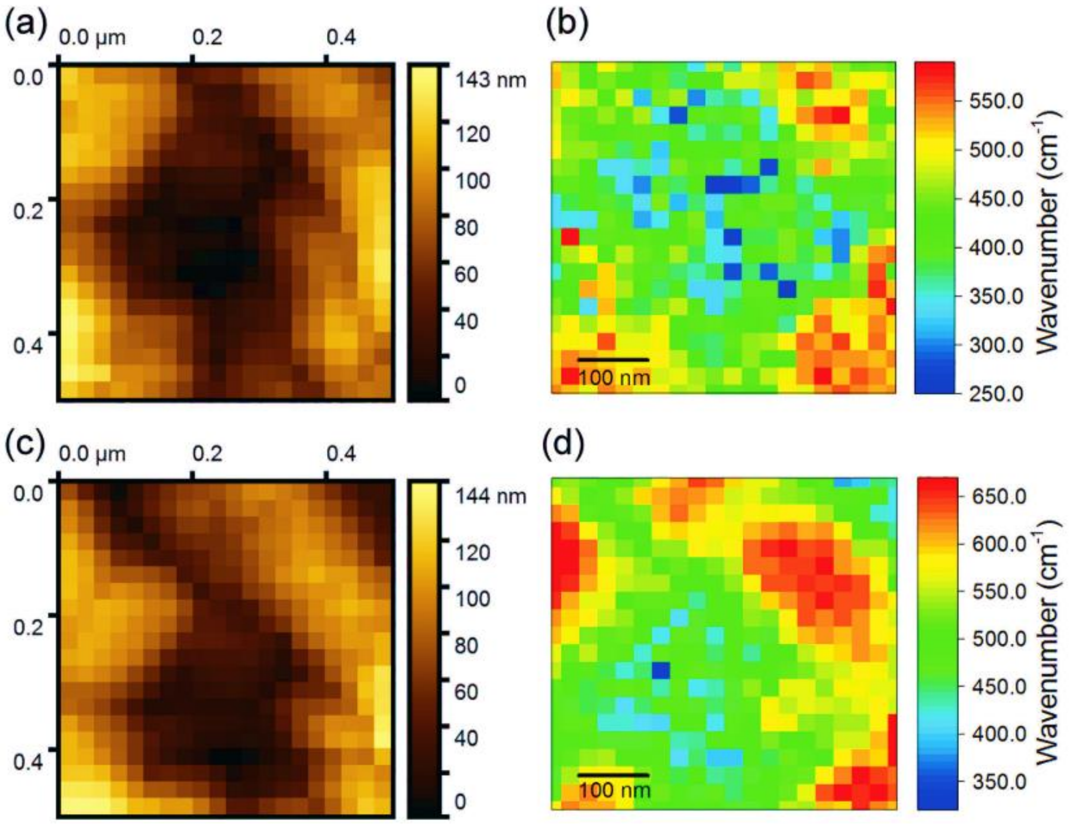

Figure 9.6: (a) topography of one region and the corresponding LSPR position map (b) of the same area, (c) topography second region and the corresponding LSPR position map (d).188 © the Owner Societies 2016

Numerical simulations were conducted to verify this model using COMSOL the result of which is shown in *Figure 9.7*. The simulated absorption cross-section of the gold tip at the apex when the tip is placed on AlGaAs (higher refractive index) island and on an AlN pit (lower refractive index) shows a blue shift in peak position, in agreement with the experimental results.

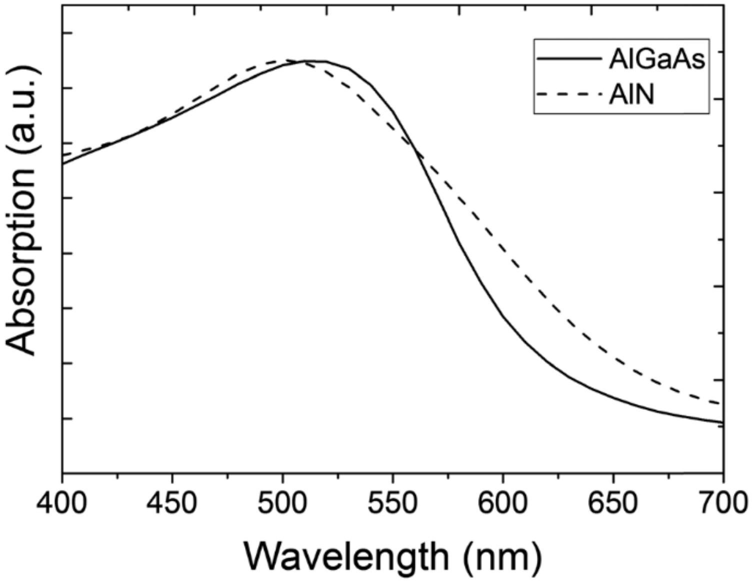

Figure 9.7: Simulated absorption spectra of a gold TERS tip apex when the tip is on top of an AlGaAs island (complete line) and on top of an AlN pit (dashed line).188 © the Owner Societies 2016

While this work has shown that the LSPR shift can be exploited to image changes in refractive index of a material, they also suggested an influence of the topography, which remained unexplained. As topography has previously been demonstrated to provide crucial contributions to the interpretation of scanning probe data e.g. in the case of piezoresponse force microscopy, understanding its effect in refractive index imaging is crucial to avoid any misinterpretation of the results.

To assess this topography influence, we image the LSPR position on chemically homogeneous strontium titanate ($SrTiO_3$) nanostructures deposited on platinized MgO (100) substrate. These measurements are performed using a gold tip via aSNOM in TERS configuration as shown in *Figure 9.8*. We chose $SrTiO_3$ as sample system as its bulk structure is Raman-silent due to its symmetry ($Pm\bar{3}m$).[206] The absence of Raman features ensures that only the LSPR position is measured, while the nanostructures present topography changes strong enough to induce a shift in the enhanced luminescence.

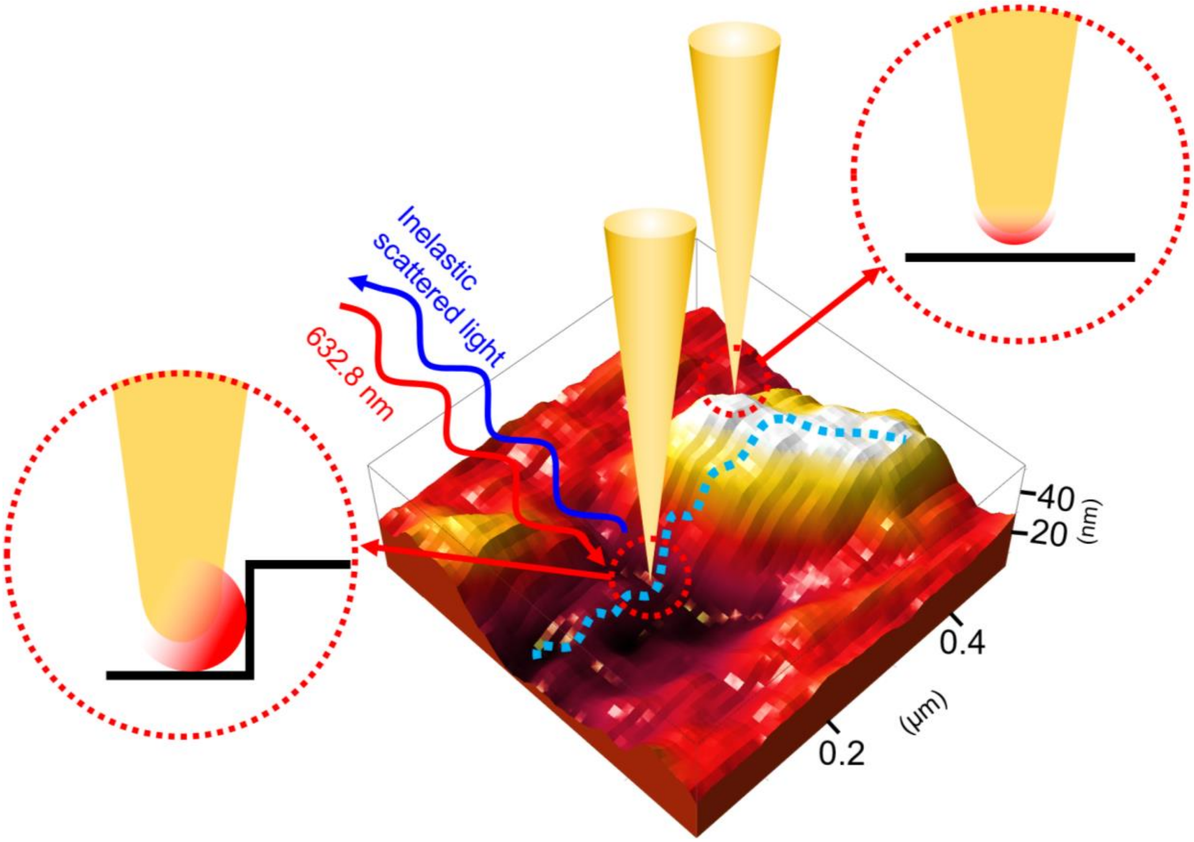

Figure 9.8: 3D representation of the displacement of the gold tip during the mapping of the LSPR position on $SrTiO_3$ nanostructures by aSNOM in TERS configuration.

The 15 nm thick $SrTiO_3$ nanostructures were grown on (100) platinized magnesium oxide substrates (Pt/MgO (100)) by on-axis radio-frequency (RF)-magnetron sputtering (SPT310, *Plasmionique Inc.*) using a polycrystalline $SrTiO_3$ ceramic disc (2.54 cm diameter and 0.317 cm thickness) as the sputtering target. The deposition was performed at 650°C with an optimized process gas of argon (Ar) and oxygen (O_2) [oxygen partial pressure, $P_O = O_2 / (Ar+O_2) = 30\%$] and the operating pressure was maintained at 40 mTorr during the deposition for an RF power of 15 W.

The topography of the studied sample is depicted in Figure 9.9 (a) and monitored simultaneously with the optical properties. It shows the formation of $SrTiO_3$ nanostructures with ellipsoidal shape on platinized MgO substrate. The deposited nanostructures have typical diameters of ~200 nm and layered structures, thus providing steps with variable heights. As for the coverage rate, the nominal film thickness (equivalent thickness if the film was dense) is 15 nm, so that from the topography of up to 50 nm for nanostructures, we estimate a surface coverage fraction of approximately 50%. Figure 9.9 (b) depicts the high resolution map of the

LSPR position of the enhanced gold luminescence of the corresponding surface topography with a spatial resolution in the order of 10 nm, which is way below the diffraction limit. The obtained map is acquired by recording a spectrum of the LSPR enhanced gold luminescence at each pixel and fitting it with a Lorentzian equation. The gold tip exhibits a detectable signal which corresponds to its luminescence enhanced by the LSPR at its apex. The LSPR position corresponds to the wavenumber at which this Lorentzian shaped curve reaches its maximum. The LSPR position is linked to the effective permittivity of the surrounding medium, composed of air and $SrTiO_3$ in our case. Figure 9.9 (c) shows the typical gold tip signal fitted with Lorentzian equation at two different positions of the sample: when the tip moves from a planar surface (dark blue region Pos.1) to a step feature (light blue region, Pos. 2) as illustrated in Figure 9.9 (b). We observe a redshift of the LSPR position when the tip moves from position 1 to position 2 due to the change in the permittivity distribution surrounding the gold tip. In addition, we notice a strong correlation between the sample topography and the LSPR position. These changes cannot be explained by a change in the material composition. The distribution of the LSPR position varies with the topography and is highly dependent on the tip environment and particularly on the air to $SrTiO_3$ volume fraction at the very vicinity of the tip apex.

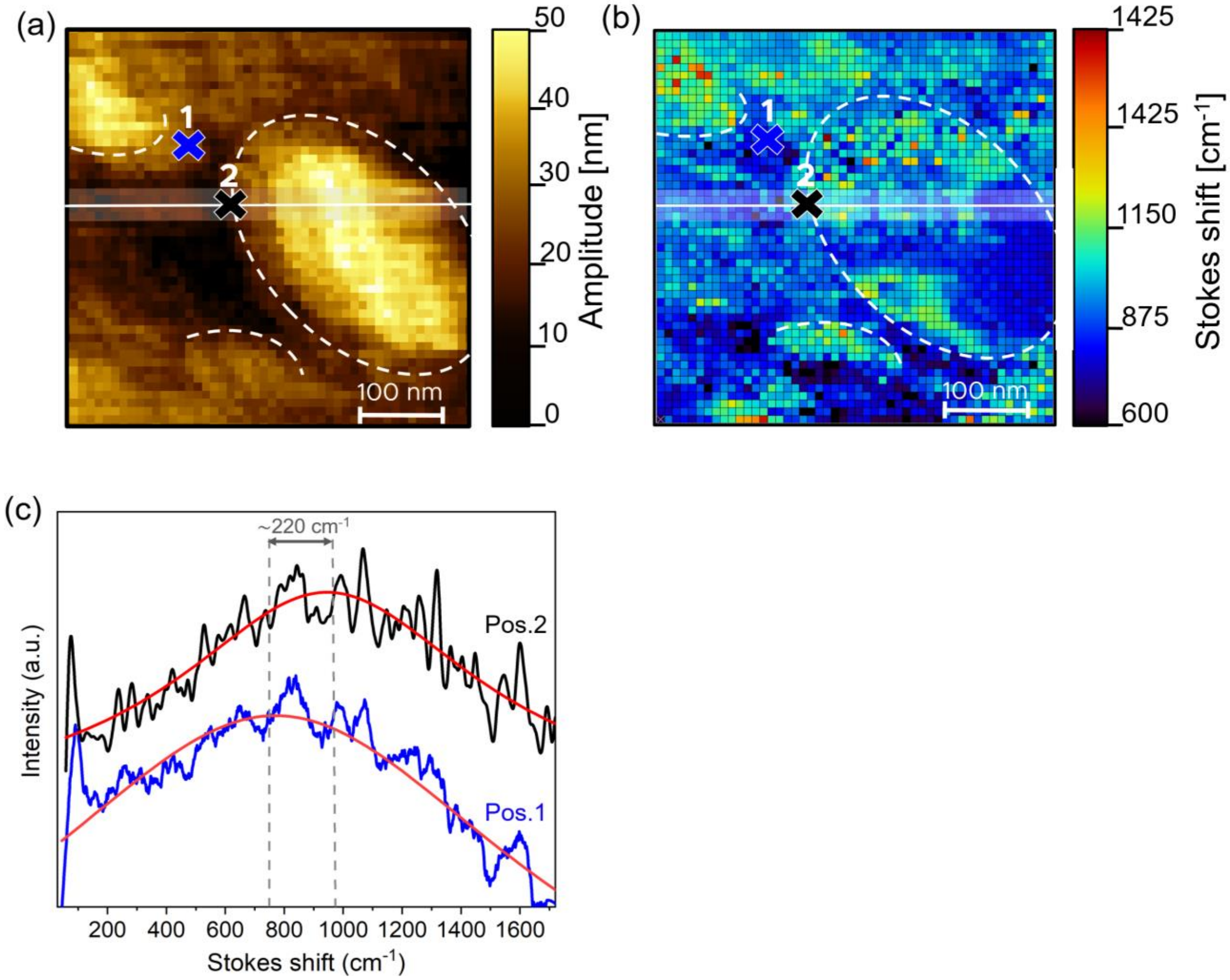

Figure 9.9: (a) 500 × 500 nm^2 topography image of the SrTiO$_3$ nanostructures,(b) High resolution map of LSPR position on SrTiO$_3$ nanostructures deposited on platinized substrate. The white lines correspond to the areas over which the profiles were measured. The exposure time for measuring each spectrum was 1 s and (c) Typical gold tip signal spectra acquired on a planar surface (Pos. 1) and at a step feature (Pos. 2) and fitted with Lorentzian function (red line). The value of 220 cm-1corresponds to the difference in the center positions of the Lorentzian functions obtained by a least-square fit.

Previous work showed that the LSPR position changes with the average refractive index of the surrounding medium. In our experiments, the gold tip is placed above the sample surface with a constant tip-sample distance of ~1 nm. Thus, instead of being completely immersed in the sample (as it is the case for nanoparticles in liquids), the luminescence of the tip apex is affected not only by the material at the apex, but in addition by the surrounding medium, which is air in our case. Consequently, changes in topography will induce changes in the average medium due to a variation of the fraction of $SrTiO_3$ surrounding the gold tip. To confirm our hypothesis, we investigated the changes in topography along a line simultaneously with the shifts in LSPR position (Figure 9.9 (a-b), white lines). This region was chosen as it depicts relatively large step features that also extend vertically, thereby allowing us to average over four horizontal lines and improve the signal to noise ratio (Figure 9.9 (b), white areas surrounding the white lines). We can see from the topography that the $SrTiO_3$ nanostructure depicts some step-terraces features. When the tip reaches a step, the LSPR position shifts to higher wavenumbers. This can be explained in the sense that when the tip is scanning a chemically and structurally homogeneous material depicting some topography features, different positions on the sample surface may yield a different volume fraction of the sample material at the very vicinity of the tip. This variation leads to a change in averaged refractive index surrounding the tip apex, thus leading to shifts that we observe experimentally in Figure 9.10 (a). To highlight the correlation between the topography and the LSPR shift, we compared the LSPR position variations to the second derivative of the height of the analyzed topography as depicted in Figure 9.10 (b). The figure indicates that the concave shaped steps of the topography is governing the variation of the LSPR position, thus enhance it shift to higher wavenumbers.

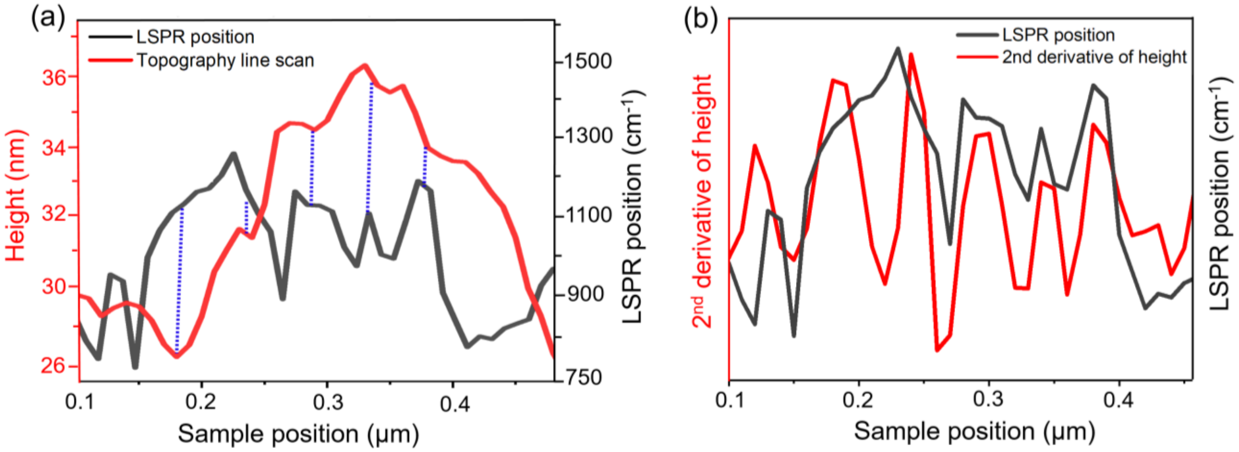

Figure 9.10: (a) Quantitative measurement of the anti-correlation between the variation of the LSPR position and the topography changes. The blue lines show the evolution of the LSPR position when the topography of the $SrTiO_3$ nanostructures shows stepped morphology, (b) Correlation between the variation of the LSPR position and the second derivative of the height.

To further validate the dependence of the LSPR position on the topography, we construct a finite element model of the tip contact area. Using this model, we compute absorption spectra and their respective peak shifts for different topographies. To calculate the absorption spectra, an excitation laser is focused on the tip and varied in wavelength. The calculation is done using the COMSOL Multiphysics electric field solver for the time-harmonic wave equation. A semispherical tip with a diameter of 20 nm and a step height of 10 nm is chosen in accordance to step heights obtained from the experimentally measured topography. The exact shape of the steps remains however unknown due to the tip-surface convolution. In the simulation, we compare shifts of tip absorption peaks, which are indicative of the shift of LSPR position. The absorption at the apex of the gold tip was simulated for three configurations, the tip on top of a planar surface, at a rectangular shaped step and at a concave shaped step. As the $SrTiO_3$ to air volume ratio increases from configuration (a) to (c), the simulation spectra show a shift to higher wavenumber (*Figure 9.11*), consistently with experimental results. The fact that the numerical simulation predicts even larger LSPR shifts than those experimentally determined is attributed to idealized conditions in the simulation, especially with respect to the shape of both tip and surface. These results confirm that the LSPR position shift observed on our $SrTiO_3$ nanostructures is indeed due to a topography effect and not to a change in the material composition. This further shows that the topography of the sample has to be taken into account when performing refractive index mapping. Moreover, it should not be neglected in TERS analysis as changes in topography could induce a change in the Raman peak intensity through a variation in the enhanced spectral range.

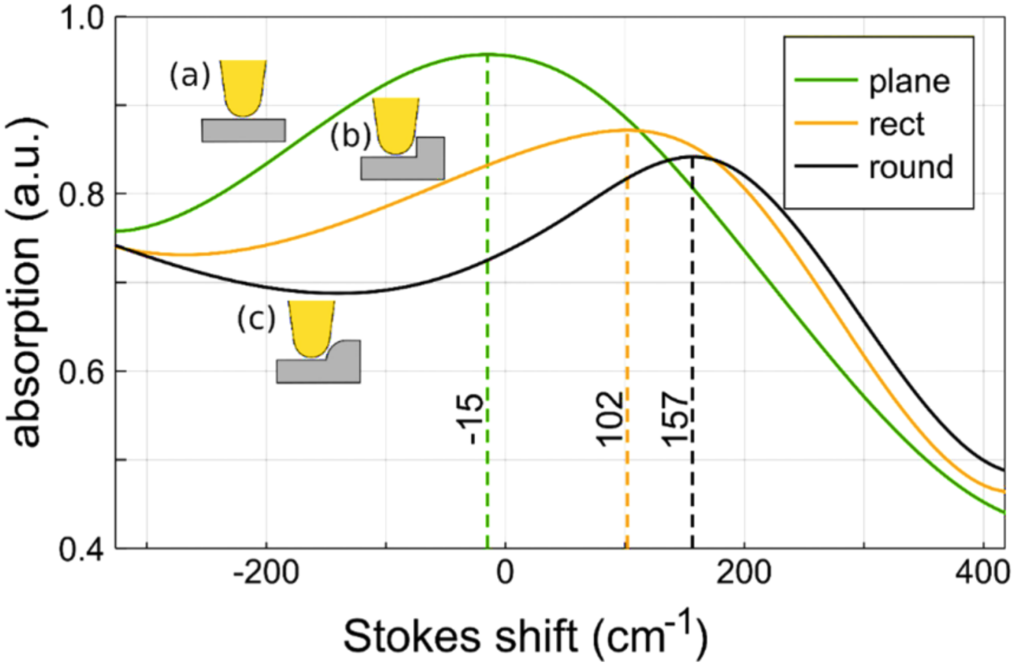

Figure 9.11: Simulated absorption spectrum shifts due to surface profile.

In summary, we report on the effect of topography changes while mapping the LSPR of enhanced gold tip luminescence in TERS configuration across chemically and structurally homogeneous $SrTiO_3$ nanostructures with a high spatial resolution in the order of 10 nm. The obtained LSPR position strongly correlates with the topography of the sample, which we attribute to variations in the volume fraction of material interacting with the optical near field. Numerical simulations provide concurring trends, somewhat overestimating the expected LSPR shifts. Our work highlights the importance of considering the sample topography in the interpretation of optical near field data while performing near-field refractive index mapping and TERS experiments for both qualitative and quantitative purposes.

9.3 LSPR intensity and effective refractive index of tip surrounding environment

Parts of the following section are reproduced from: *J. Zhang, A. H. Youssef , A. Dörfler, G. Kolhatkar, A. Merlen and A. Ruediger, Sample induced intensity variations of localized surface plasmon resonance in tip-enhanced Raman spectroscopy, Opt. Express, 2020,* ***28****, 25998*. My contribution to the manuscript as first author to the manuscript is listed below:

- Conducting near-field mapping in TERS configuration, including fabrication and selection of Au tips via electrochemical etching, tip cutting and gluing, system alignment, tip-laser alignment, system optimization and complete mapping process.
- Identifying a proper substrate (platinum) for sample preparations.
- Identifying the correlation between tip signal intensity and sample topography which resulted in originating the main idea for this paper.
- Manuscript writing, including the main text as well as figures.

One of the key challenges in TERS is the understanding of its relative peak intensity, and it is generally acknowledged that the Raman signal in TERS is mostly enhanced through LSPR of nanostructures at the tip apex whereas vibrational modes appearing at LSPR wavelengths with different scattering strengths may experience different enhancements leading to variations in relative TERS intensity. [207] Thus the understanding of LSPR is the core to correctly interpret TERS near field spectra. Furthermore, in the work of Blum et al. in which an interlaboratory reproducibility and comparison study was carried out, [208] it was noticed that the relative peak intensity ratios vary significantly between different groups, as well as within the same group. Significant variations in the peak intensity ratio were also observed for measurements performed with the same tip. Therefore, there is an urgent need for the understanding and evaluation of LSPR, as its properties are of great importance to the interpretation of TERS signals, especially its resonance position which defines the spectral range of enhancement and its relative intensity which governs the intensity ratio of different Raman modes of the sample.[209,210] The properties of the LSPR, such as its resonance position as well as its intensity are highly sensitive to changes in its surrounding dielectric environment and are directly linked to the effective permittivity of the surrounding dielectric environment interacting with the optical near field at the very tip apex.[211] In previous sections I have introduced the influence of the material composition and topography on the variation of the LSPR position in TERS by monitoring the signal of the gold tip. [186–188,212]

We now extend this work by focusing on identifying the influence of the material composition and topography on the relative intensity of the LSPR through the study of the gold tip signal.

In TERS, the intensity of its signal follows the Raman 4th power rule.[213,214] The overall enhancement factor *(G (ω))* is given by equation 9.3:[178,193] When the tip apex is considered to be spherical, the *g* factor is given by [178,193]

$$g = \frac{\varepsilon_{metal}(\omega,r) - \varepsilon_{environment}}{\varepsilon_{metal}(\omega,r) + 2\ \varepsilon_{environment}} \qquad \textit{9.3.1}$$

where ε_{metal} is the permittivity of the metallic particle and $\varepsilon_{environment}$ the permittivity of the surrounding medium. This permittivity is generally considered homogeneous, which becomes invalid when the tip approaches the surface. Thus, the material permittivity is substituted by an effective value that takes into account the geometric contribution in the dielectric environment surrounding the tip.

Since the intensity of the TERS signal is obtained as the product of the Raman intensity and the enhancement factor, there exists a direct relation between signal and this effective permittivity, which needs to be taken into account during a typical TERS experiment. When distance between tip and sample surface is large, the plasmonic hot spot does not interact with the sample since the dielectric environment is composed only of air. When the tip is placed in feedback with the sample surface, the dielectric environment becomes a combination of both air and sample, the latter typically having a relative permittivity larger than that of the former, thus leading to a change in the effective permittivity surrounding the tip apex and interacting with the optical near field. As the tip scans an inhomogeneous or rough surface, the effective permittivity at the tip's apex vicinity changes due to variations in the material composition or surface topography. The intensity of the LSPR at a given wavenumber varies as a consequence, leading to intensity changes in the observed LSPR enhanced gold tip luminescence. In TERS experiments, such changes are known to affect the TERS signal.[210]

In order to support our model, we image the LSPR enhanced gold tip luminescence above strontium titanate ($SrTiO_3$) nanoislands grown on (100) platinized magnesium oxide substrates

(Pt/MgO (100)). $SrTiO_3$ was chosen as its bulk structure is Raman-silent due to its symmetry ($Pm\bar{3}m$) and with a 1 second acquisition time, $SrTiO_3$ does not present any Raman signature, the second order spectrum being too weak to be detected so that the signal obtained in TERS can be assigned to the tip signal entirely.[206,215] Furthermore, as we have explained in previous sections, gold PL is an intrinsic property that for the same tip under study remains relatively constant. Thus, any intensity variation of the tip signal can be attributed to a change in the LSPR intensity. *Figure 9.12* illustrates the topography of the sample with the corresponding tip signal intensity map. $SrTiO_3$ nanoislands can be identified on the intensity map (indicated by the zone within the white dashed ellipse), and it only depicts the intensity variations of the gold tip signal. Significant variations in intensity at different areas of the sample can be observed. The LSPR intensity variations due to sample material and topography properties are demonstrated individually in the following two sub-sections.

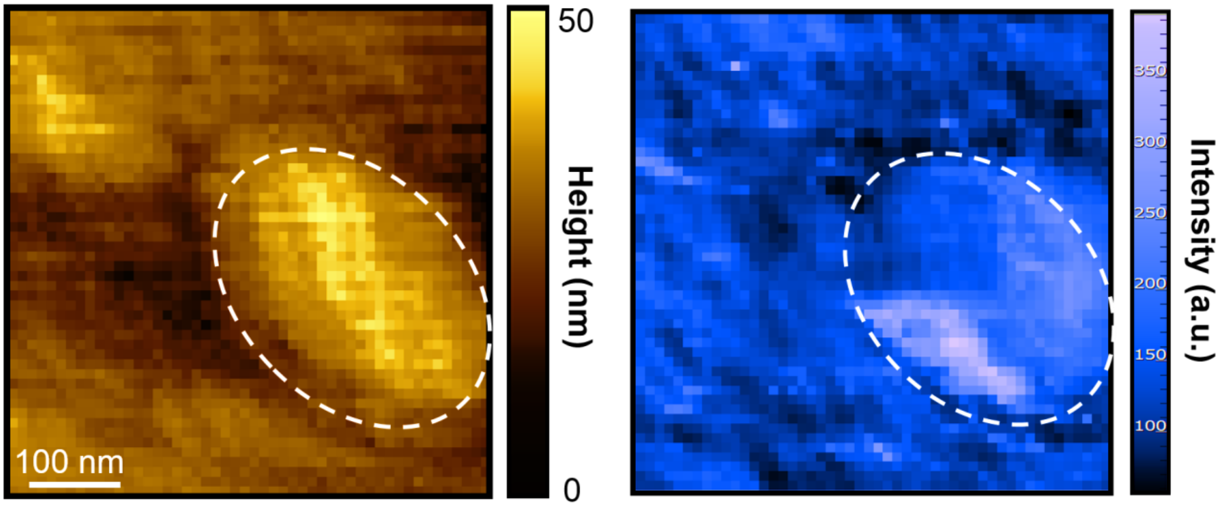

Figure 9.12: Atomic force microscopy topography of $SrTiO_3$ nanoislands grown on polycrystalline Pt (left) and the corresponding spectrally integrated tip signal intensity map (right), the indicated area (dotted line) identifies a $SrTiO_3$ nanoisland. Both images were recorded simultaneously.

9.3.1 Influence of material composition

To verify the material influence of the sample on the LSPR intensity, we investigate the gold tip signal intensity at two different positions on the sample surface as illustrated in *Figure 9.13*: the first is one located on top of the $SrTiO_3$ nanoisland and the second one, on the Pt substrate.

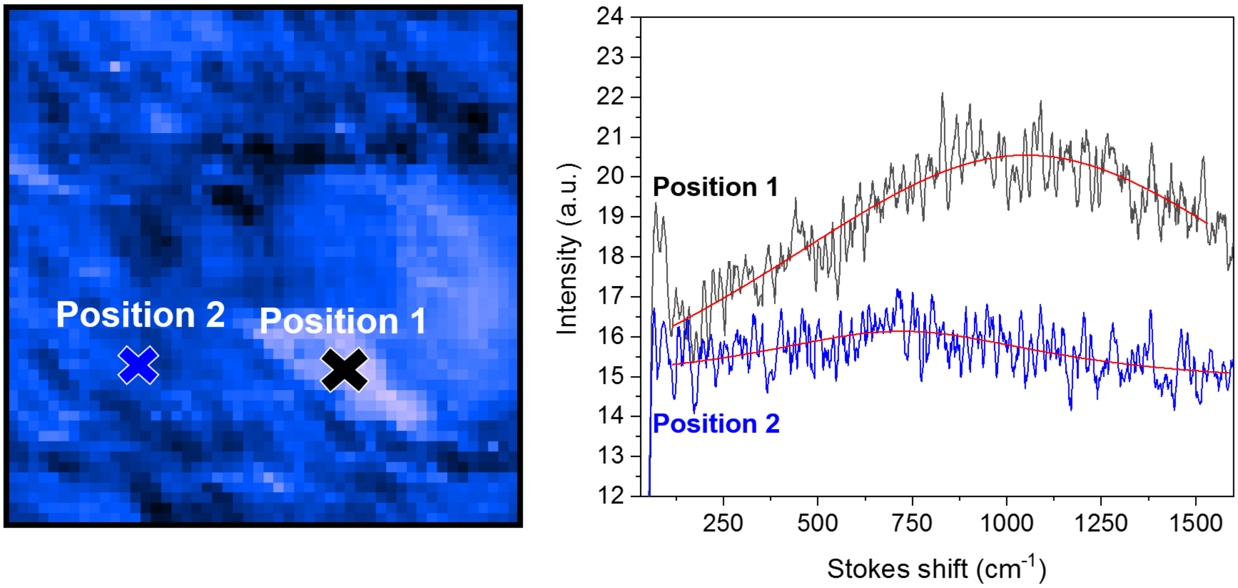

Figure 9.13: Spectrally integrated tip signal intensity map (left), identifying two positions: position 1 (on top of a $SrTiO_3$ nanoisland) and position 2 (on top of Pt substrate). Experimental gold emission (black and blue) and numerical fit with a Lorentzian function (red). Position 1 features a higher intensity and a red shift compared to position 2.

Figure 9.13 reveals that when the tip is on top of the $SrTiO_3$ nanoisland, the tip signal intensity is visibly higher than that obtained when the tip is on the Pt substrate, indicating an increase in the LSPR intensity on the nanostructure. According to equation 9.3 and 9.3.1, this change in LSPR intensity could be due to an increase in effective permittivity when the tip goes from the Pt region to the $SrTiO_3$ nanoisland. Under our experimental conditions, the relative permittivity of Pt is negative, thus much smaller than that of $SrTiO_3$. This difference in relative permittivity leads to the observed changes in the LSPR intensity.

9.3.2 Topography influence

To verify the topography influence of the sample on the variation of LSPR intensity, we focus on the gold tip signals detected on $SrTiO_3$ nanoisland as presented in *Figure 9.14*, where no composition changes are expected.

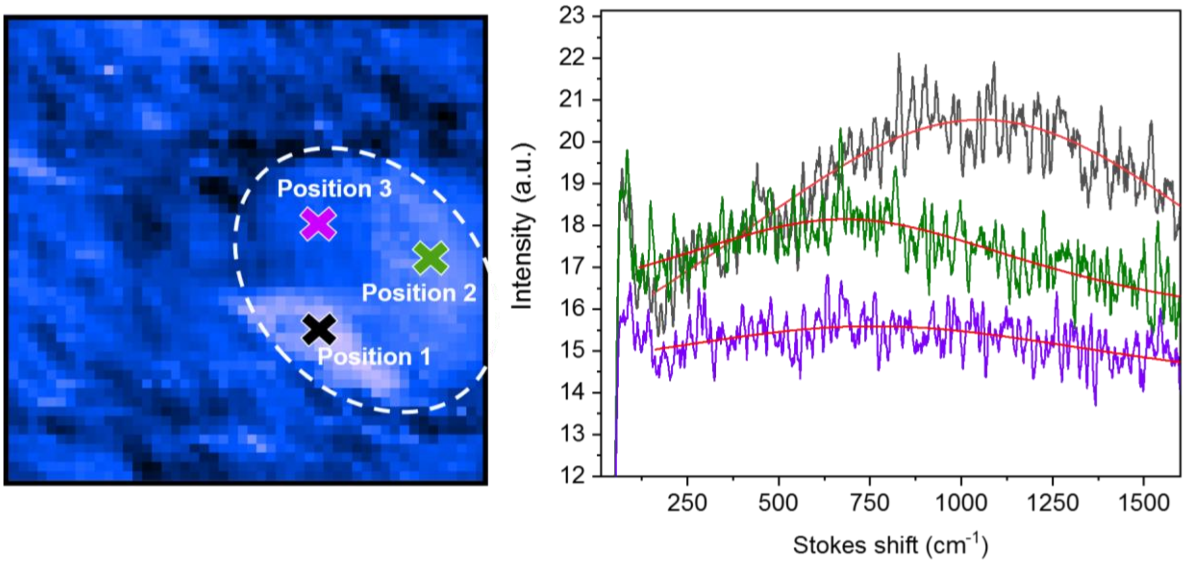

Figure 9.14: Spectrally integrated tip signal intensity map (left), identifying three positions on top of SrTiO$_3$ nanoisland. Experimental gold emission (black, green, and purple) and numerical fit with a Lorentzian function (red).

As we can see from *Figure 9.14*, when the tip is scanning on top of a SrTiO$_3$ nanoisland, significant variations in the tip signal intensity are observed and attributed to a topography influence, given that the three points were chosen from different areas on top of the SrTiO$_3$ nanoisland with varied topography. As the local topography at the vicinity of the tip apex varies, so does the volume ratio between SrTiO$_3$ and air, thus leading to a change in effective permittivity. This translates into a change in the tip signal intensity according to equations 9.3 and 9.3.1. However, it should be noted that during a typical TERS experiment, the exact location of the hot spot on the tip remains unknown. Depending on the exact location of the hot spot, the LSPR intensity reacts differently to the surface features. To be more specific, as seen in *Figure 9.15*, when located at position 2, the LSPR will be more sensitive to positive slopes along the fast scanning direction whereas for position 1 and 3, LSPR will be less responsive to changes in topography such as a step feature. This effect is unrelated to the direction of the incident beam and cannot be controlled experimentally. Because of this, it is very difficult to quantitatively assess the influence of topography on LSPR intensity.

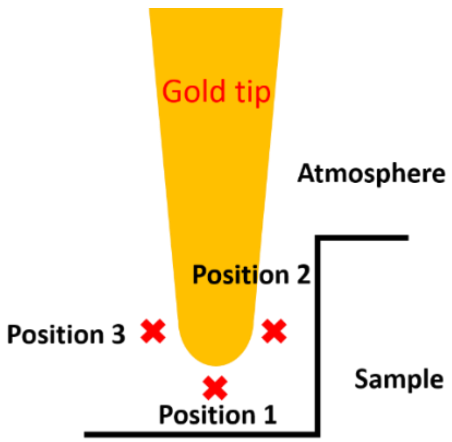

Figure 9.15: Schematic of potential locations of LSPR at the gold tip apex (side view) and their sensitivity to topography changes (indicated as a step feature)

It should be noted that during an actual TERS experiment, the material composition and topography affect the LSPR intensity simultaneously. Thus, our results demonstrate the possibility and the high sensitivity to exploit the amplitude of the optical near field signal of the tip to discriminate materials on the surface based on their high frequency permittivity (refractive index). The impact of this observation extends to TERS experiments: it has since long been reported that the relative intensities in TERS spectra may vary during a scan or for the same molecule on different substrates. Our findings provide one possible explanation as any local change of permittivity interacting with the optical near field, introduced either by the sample itself or by the substrate is prone to affect the spectral distribution of the LSPR. Moreover, this change of permittivity is not limited to a change in the nature of the material but to a relative change of the occupied volume of the optical near field through e.g. changes in local topography.

The following analytical model estimates the effect of amplitude and frequency shift of the gold tip using the close relation between the tip absorption and emission spectrum. Approximating the gold tip as a sphere, and its surrounding environment as a medium of homogeneous permittivity, the following analytical absorption formula for metallic nanoparticles can be applied [216]

$$C_{abs}(\lambda) = \frac{2\pi}{\lambda}\, im\left[\frac{4\pi D^3}{2}\frac{\varepsilon_{tip}(\lambda)-\varepsilon_{env}(\lambda)}{\varepsilon_{tip}(\lambda)+2\varepsilon_{env}(\lambda)}\right] \qquad 9.3.2$$

Using the equation for absorption in a spherical nanoparticle, and linearly weighing the embedding environment permittivity ε_{env} between air and the surface material, we obtain absorptions peaks as shown in *Figure 9.16*. The values of permittivity for $SrTiO_3$ and Pt are taken from [130,217] respectively. The percentages are chosen to visualize the trends of absorption curves;

an analytical relation between percentages and surface geometry is not implied. Detailed calculation results are presented in *Table 9.1*.

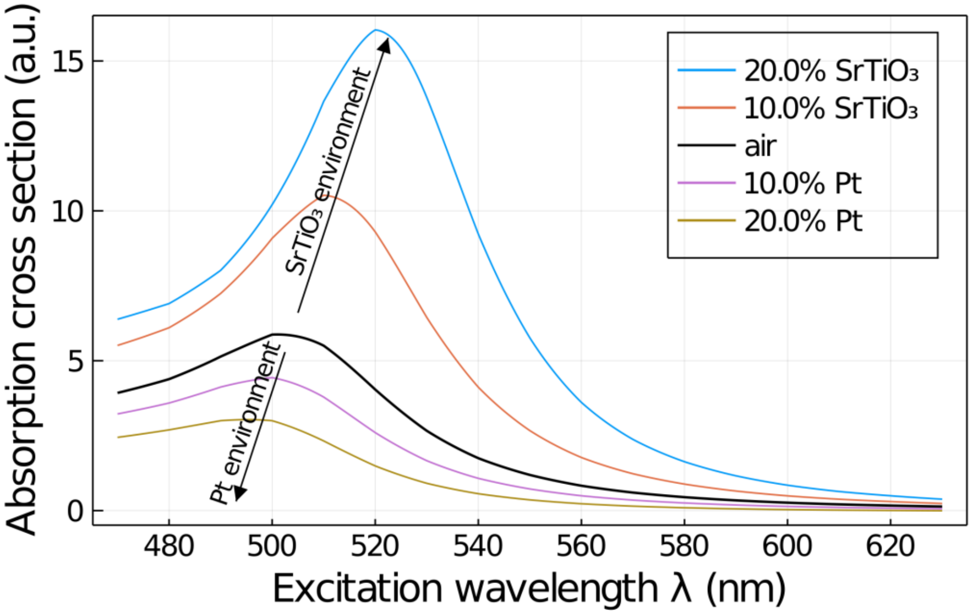

Figure 9.16: Schematic trend of the tip absorption intensity in different scenarios. The tip is approximated by a sphere of 20 nm diameter. Percentages indicate the linear weighing between air and the surface material permittivity. The Pt vicinity lowers absorption peak intensity and position, while $SrTiO_3$ increases both, with a comparatively more pronounced effect.

Table 9.1: Effects of the proximity of Pt and $SrTiO_3$ on the tip absorption as calculated from the analytical model

Material composition	Absorption peak position λ (nm)	Peak shift (nm)	Relative absorption change (%)
20% $SrTiO_3$	520	19	170
10% $SrTiO_3$	510	9	80
air	501	0	0
10% Pt	500	-1	-20
20% Pt	495	-6	-50

The model qualitatively supports our experimental observations. An increase in the intensity of total absorption in case of the $SrTiO_3$ surface is observed, as compared to the Pt surface. The model also confirms the observed wavelength shifts experimentally, where position 1 corresponds to a concave, valley-like $SrTiO_3$ structure, which occupies more of the tip vicinity, thus having a greater effect on the absorption peak shift and intensity as compared to the convex nanoisland of position 2.

To further demonstrate the possibility and the high sensitivity of optical mapping of materials solely based on the tip signal intensity in a TERS-like measurement, the same data from the work of G.K. was used ($Al_{0.1}Ga_{0.9}N_xAs_{1-x}$ alloy).[188] Rather than fitting the tip signal of each pixel and then compute the map with regards to the LSPR position, the intensity of the tip signal was used directly to generate the maps (*Figure 9.17* (a)(c)). The corresponding topography images of the sample obtained simultaneously are shown in *Figure 9.17* (c) and (d). The islands are AlGaAs (n≈4.0) and the pit is AlN (n≈2.2). Very strong correlations and significant variations in intensity at different areas of the sample can be observed. This can be explained with our proposed theory given above, that the tip signal intensity is directly linked to the effective permittivity (refractive index) surrounding the tip apex, which is influenced by both the local topography as well as the material composition.

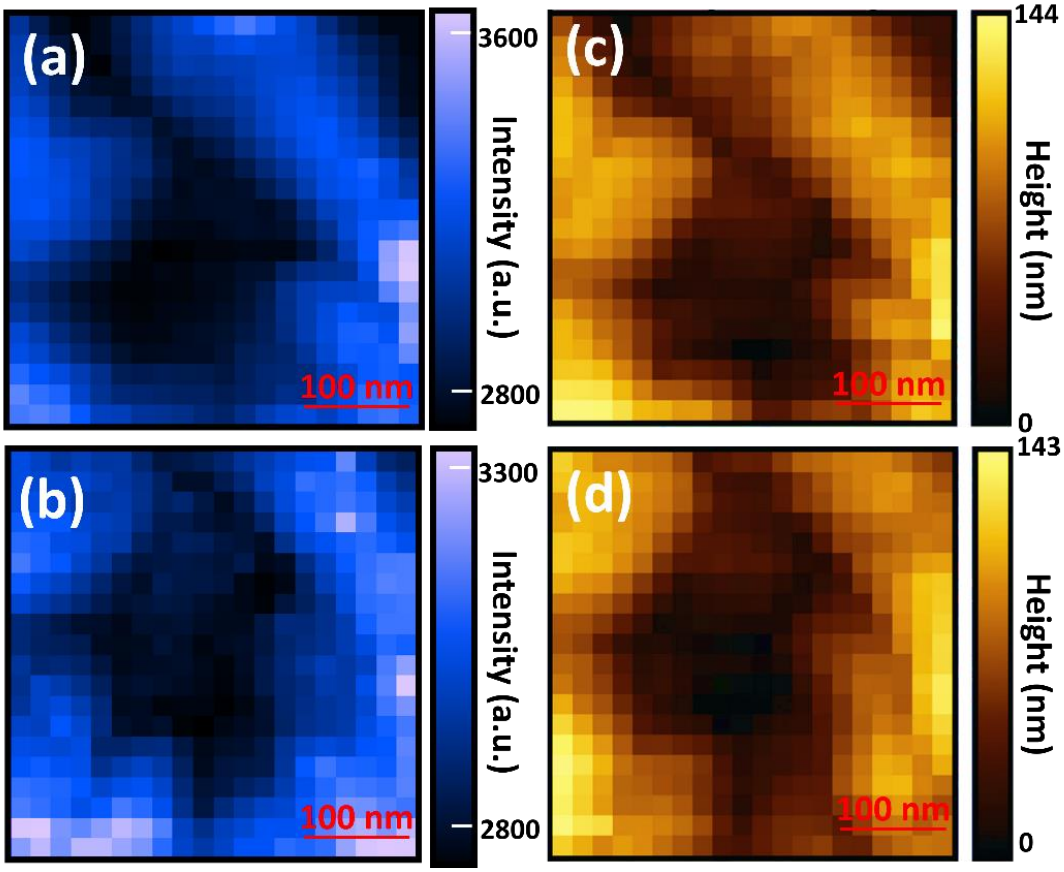

Figure 9.17: (a) (b) 500 nm × 500 nm tip signal intensity mapping of the Al0.1Ga0.9NxAs1-x sample of two regions and the corresponding topography images (c) and (d).

Compared with previous results based on LSPR position (*Figure 9.6*), maps generated via tip signal intensity show a stronger correlation as well as higher resolution. Furthermore, given that the tip signal need not to be fitted individually in each pixel, this new imaging technique is more time-efficient. Moreover, errors due to the fitting process are also avoided.

It should be noted that this cannot be a tip-sample distance artefact due to the fact that an intensity change of around 20% correlates to approximately 2 nm change in tip-sample distance, which is much higher than the precise control and stability in z direction of our system (typically in the range of 10 pm).[196,218]

In conclusion, our findings highlight the importance of taking the surface material and topography properties into consideration for the understanding and interpretation of optical near field data including TERS. Together with our previous works, we provide insight into relative intensity variations between different Raman modes in a TERS spectrum, which has been a key issue in the community for years.

Furthermore, our results demonstrate the possibility and the high sensitivity of optical mapping of materials solely based on the tip signal intensity in a TERS-like measurement. With progressing control of tip shapes and nanoscale feedback, specific chemical information might become accessible without having to rely on the low cross-section of Raman scattering.

10 Conclusion

Following the concept of Au TERS tip fabrication via pulse electrochemical etching, I have adapted the technique to the fabrication of Ag TERS tips. Furthermore, by designing the two step etching process, I have successfully addressed the issue of over-etching, which has been a bottleneck in the field. The current Ag TERS fabrication technique is considerably more simple and cost-efficient which does not rely on any additional devices such as a cut-off circuit to guarantee small tip radii. The tips demonstrate high enhancement factor.

Previous works in our group have established a model for the intrinsic TERS Au tip signal, which can be assigned as the LSPR enhanced Au PL. Based on such model, we can retrieve the approximate LSPR curve. I have developed an in situ technique for the evaluation of Au TERS tip plasmonic property with a simple fitting process. This technique is reliable, efficient and can be readily adopted in any TERS measurements regardless of the system setup or the type of Au tip in use. Given this evaluation process can be completed at a very early stage of a TERS experiment, we can quickly determine whether the tip is very plasmonic, which makes it extremely promising for TERS enhancement on sample under study, or average plasmonic, which makes it a candidate for other types of near-field imaging which does not rely strongly on the TERS enhancement, or non-plasmonic, which signifies the tip needs to be discarded or further treated (cleaning etc).

Furthermore, given that the LSPR curve can be extracted from the tip signal, its position can be used for near-field refractive imaging, as changes in local effective refractive index near the tip apex induce detectable changes to the LSPR position. In my work I have identified a sample topography influence on the LSPR position. Together with previous works from our group, we have demonstrated the dependence of LSPR position and effective refractive index, which varies with both local material composition and topography.

Last but not the least, I have identified that local material composition and topography not only affect the LSPR position but its intensity as well (*Figure 10.1*). The intensity of the LSPR alone can be used for near-field imaging. Given that the intrinsic Au PL is constant; the tip signal intensity can be used directly for near-field imaging. Compared to near-field imaging via LSPR position, no fitting process is needed which reduces errors introduced during the fitting process.

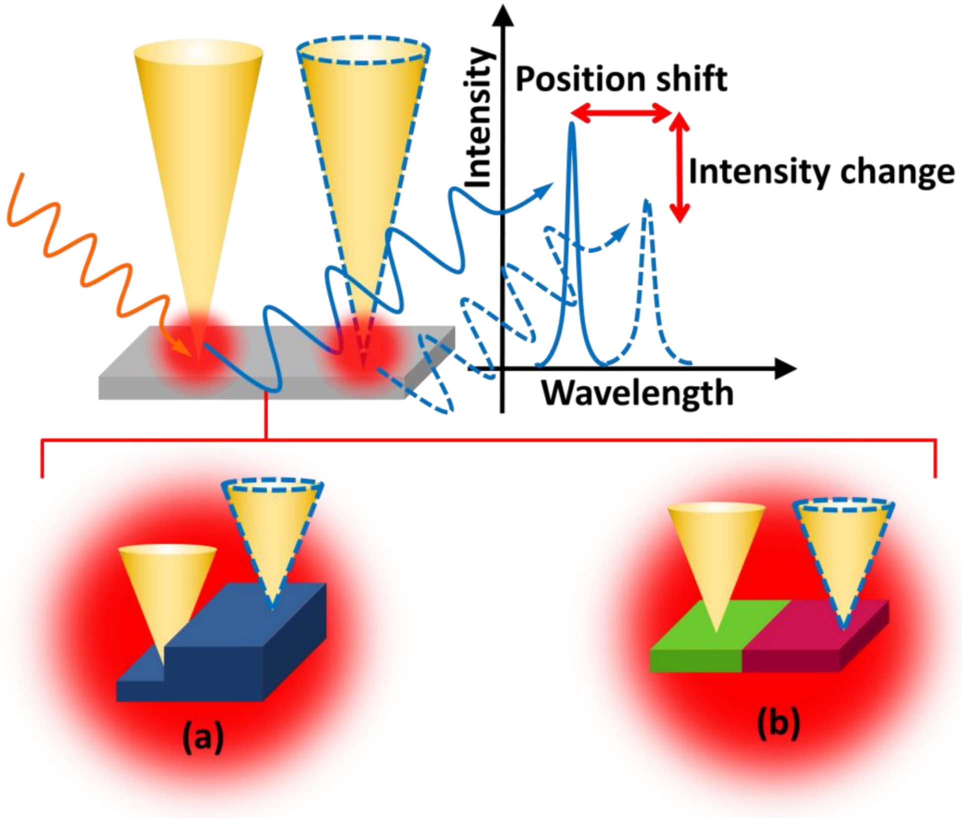

Figure 10.1: Sample (a) local material composition and (b) topography influence on LSPR position and intensity

As a conclusion, my work highlights the importance of taking the local material composition as well as topography into consideration during a typical TERS experiment, and identifies their influence on the plasmonic behavior of the tip. This leads us closer to solving the issue of understanding and correlating relative TERS signal intensities, which has been a key challenge in the community for decades. Furthermore, I have also investigated the intrinsic tip signal in details, identifying it as a valuable tool for the early stage screening of plasmonic TERS tips, as well as establishing near-field imaging via either the extracted LSPR position or its intensity. Thus I have proven the possibility of obtaining valuable and abundant information from the tip signal, which has always been regarded as a parasitic background by the community.

11 Perspectives

Based on the progress reported in this thesis, there are multiple gateways to pursue further studies, related to the fabrication of tips and their chemical stability as well as with respect to the methodology of plasmon-enhanced tip luminescence for gold tips.

Due to the chemically less stable nature of silver as compared to gold, the life span of Ag TERS tips manufactured with the current recipe is relatively short; a protection treatment such as surface coating/passivation needs to be adopted. Ideally the coating should be Raman-inactive and sufficiently thin to not substantially interfere with the plasmon peak position. As mentioned in chapter 6.2, there exist numerous free parameters in our electrochemical etching process, thus there is still ample room for further optimization via tuning of these parameters, in particular with respect to the control of the very apex of the tip.

Currently, the study of the tip signal in TERS is based on a gold emission model. Aside from gold, silver tips are often used given that silver is more plasmonic and capable of stronger enhancement. Future study can be focused on establishing a model for silver emission as well as identifying the silver LSPR curve, similar to what has been achieved in this thesis. Secondly, currently our study of the gold TERS tip signal is mainly qualitative. Even though we can extract the rough position and intensity of the LSPR, its absolute position as well as intensity is influenced by the intrinsic gold PL which at the moment is regarded as constant. However, the exact position and intensity of gold PL varies with tip to tip due to impacts such as crystallinity etc. Future work should focus on identifying a more precise model of the tip signal in which the exact position and intensity of the LSPR can be extracted, thus turning such study from being qualitative to quantitative, allowing for e.g. a map of the absolute rather than relative refractive index across a surface with nanometer resolution. Once the exact LSPR curve of the tip in use can be extracted, the challenge of interpreting relative TERS signal intensity will be tackled. Furthermore, based on the exact location of the LSPR curve, local effective refractive index can also be calculated.

BIBLIOGRAPHY

1 C. V. Raman and K. S. Krishnan, A new type of secondary radiation, *Nature*, 1928, **121**, 501–502.

2 I. P. Herman, Peak temperatures from Raman Stokes/anti-Stokes ratios during laser heating by a Gaussian beam, *J. Appl. Phys.*, 2011, **109**, 016103.

3 M. Malyj and J. E. Griffiths, Stokes/Anti-Stokes Raman Vibrational Temperatures: Reference Materials, Standard Lamps, and Spectrophotometric Calibrations, *Appl. Spectrosc.*, 1983, **37**, 315–333.

4 S. D. Rassat and E. J. Davis, Temperature Measurement of Single Levitated Microparticles Using Stokes/Anti-Stokes Raman Intensity Ratios, *Appl. Spectrosc.*, 1994, **48**, 1498–1505.

5 B. J. Kip and R. J. Meier, Determination of the local temperature at a sample during Raman experiments using Stokes and anti-Stokes Raman bands, *Appl. Spectrosc.*, 1990, **44**, 707–711.

6 M. Lapp and C. M. Penney, Analysis of Raman and Rayleigh Scattered Radiation, *Methods Exp. Phys.*, 1981, **18**, 408–433.

7 T. D. Thangadurai, N. Manjubaashimi, S. Thomas and H. J. Maria, *Nanostructured materials*, Springer Nature Switzerland.

8 E. Abbe, Beiträge zur Theorie des Mikroskops und der mikroskopischen Wahrnehmung: I. Die Construction von Mikroskopen auf Grund der Theorie, *Arch. für mikroskopische Anat.*, 1873, **9**, 413–418.

9 Rayleigh, Investigations in optics, with special reference to the spectroscope, *London, Edinburgh, Dublin Philos. Mag. J. Sci.*, 1879, **8**, 261–274.

10 D. Eschimese, PhD thesis, Universite de Lille, 2019.

11 S. B. Ippolito, B. B. Goldberg and M. S. Ünlü, Theoretical analysis of numerical aperture increasing lens microscopy, *J. Appl. Phys.*, 2005, **97**, 053105.

12 T. Lecklider, The world of the near field, *Eval. Eng.*, 2005, **44**, 52–57.

13 E. H. Synge, XXXVIII. A suggested method for extending microscopic resolution into the ultra-microscopic region, *London, Edinburgh, Dublin Philos. Mag. J. Sci.*, 1928, **6**, 356–362.

14 E. A. Ash and G. Nicholls, Super-resolution aperture scanning microscope, *Nature*, 1972, **237**, 510–512.

15 G. Binning, H. Rohrer, C. Gerber and E. Weibel, Surface studies by scanning tunneling microscopy, *Phys. Rev. Lett.*, 1982, **49**, 57–61.

16 A. Lewis, M. Isaacson, A. Harootunian and A. Muray, Development of a 500 Å spatial resolution light microscope. I. light is efficiently transmitted through λ/16 diameter apertures, *Ultramicroscopy*, 1984, **13**, 227–231.

17 D. W. Pohl, W. Denk and M. Lanz, Optical stethoscopy: Image recording with resolution λ/20, *Appl. Phys. Lett.*, 1984, **44**, 651–653.

18 B. Hecht, B. Sick, U. P. Wild, V. Deckert, R. Zenobi, O. J. F. Martin and D. W. Pohl, Scanning near-field optical microscopy with aperture probes: Fundamentals and applications, *J. Chem. Phys.*, 2000, **112**, 7761–7774.

19 P. Bazylewski, S. Ezugwu and G. Fanchini, A review of three-dimensional scanning near-field optical microscopy (3D-SNOM) and its applications in nanoscale light management, *Appl. Sci.*, 2017, **7**, 973.

20 W. Adams, M. Sadatgol and D. Güney, Review of near-field optics and superlenses for sub-diffraction-limited nano-imaging, *AIP Adv.*, 2016, **6**, 7761.

21 B. Bhushan, in *Encyclopedia of Nanotechnology*, Springer Netherlands, Dordrecht, 2012, pp. 2280–2292.

22 H. Lee, D. Y. Lee, M. G. Kang, Y. Koo, T. Kim and K. D. Park, Tip-enhanced photoluminescence nano-spectroscopy and nano-imaging, *Nanophotonics*, 2020, **9**, 3089–3110.

23 H. A. Bethe, Theory of diffraction by small holes, *Phys. Rev.*, 1944, **66**, 163–182.

24 D. Van Labeke, D. Barchiesi and F. Baida, Optical characterization of nanosources used in scanning near-field optical microscopy, *J. Opt. Soc. Am. A*, 1995, **12**, 695.

25 L. Novotny, D. W. Pohl and B. Hecht, Scanning near-field optical probe with ultrasmall spot size, *Opt. Lett.*, 1995, **20**, 970.

26 F. Keilmann, Scattering-type near-field optical microscopy, *J. Electron Microsc. (Tokyo).*, 2004, **53**, 187–192.

27 X. Chen, D. Hu, R. Mescall, G. You, D. N. Basov, Q. Dai and M. Liu, Modern Scattering-Type Scanning Near-Field Optical Microscopy for Advanced Material Research, *Adv. Mater.*, 2019, **31**, 1804774.

28 G. Dai, Z. Yang, G. Geng, M. Li, T. Chang, D. Wei, C. Du, H. L. Cui and H. Wang, Signal detection techniques for scattering-type scanning near-field optical microscopy, *Appl. Spectrosc. Rev.*, 2018, **53**, 806–835.

29 C. Wang, W. Zhang, Z. Zhao, Y. Wang, P. Gao, Y. Luo and X. Luo, Plasmonic structures, materials and lenses for optical lithography beyond the diffraction limit: A review, *Micromachines*, 2016, **7**, 118.

30 S. Molesky, Z. Lin, A. Y. Piggott, W. Jin, J. Vucković and A. W. Rodriguez, Inverse design in nanophotonics, *Nat. Photonics*, 2018, **12**, 659–670.

31 S. V. Boriskina, T. A. Cooper, L. Zeng, G. Ni, J. K. Tong, Y. Tsurimaki, Y. Huang, L. Meroueh, G. Mahan and G. Chen, Losses in plasmonics: from mitigating energy dissipation to embracing loss-enabled functionalities, *Adv. Opt. Photonics*, 2017, **9**, 775.

32 J. Zhang, L. Zhang and W. Xu, Surface plasmon polaritons: Physics and applications, *J. Phys. D. Appl. Phys.*, 2012, **45**, 113001.

33 N. Kroo, G. Farkas, P. Dombi and S. Varró, Nonlinear processes induced by the enhanced, evanescent field of surface plasmons excited by femtosecond laser pulses, *Opt. Express*, 2008, **16**, 21656.

34 A. V Zayats and I. I. Smolyaninov, Near-field photonics: Surface plasmon polaritons and localized surface plasmons, *J. Opt. A Pure Appl. Opt.*, 2003, **5**, S16–S50.

35 Vandana Sharma, Shrishti Sharma and Roshan Jain, Plasmonics Technology-A Review, *World J. Res. Rev.*, 2015, **1**, 06–08.

36 I. Freestone, N. Meeks, M. Sax and C. Higgitt, The Lycurgus Cup - A Roman nanotechnology, *Gold Bull.*, 2008, **40**, 270–277.

37 N. Jiang, X. Zhuo and J. Wang, Active Plasmonics: Principles, Structures, and Applications, *Chem. Rev.*, 2018, **118**, 3054–3099.

38 P. B. Johnson and R. W. Christy, Optical constants of the noble metals, *Phys. Rev. B*, 1972, **6**, 4370–4379.

39 R. S. Anwar, H. Ning and L. Mao, Recent advancements in surface plasmon polaritons-plasmonics in subwavelength structures in microwave and terahertz regimes, *Digit. Commun. Networks*, 2018, **4**, 244–257.

40 P. Drude, Zur Elektronentheorie der Metalle, *Ann. Phys.*, 1900, **306**, 566–613.

41 S. J. Youn, T. H. Rho, B. I. Min and K. S. Kim, Extended Drude model analysis of noble metals, *Phys. Status Solidi Basic Res.*, 2007, **244**, 1354–1362.

42 J. J. Quinn, K.-S. Yi, J. J. Quinn and K.-S. Yi, in *Solid State Physics*, Springer Berlin Heidelberg, Berlin, Heidelberg, 2009, pp. 79–107.

43 A. Pinchuk, U. Kreibig and A. Hilger, Optical properties of metallic nanoparticles: Influence of interface effects and interband transitions, *Surf. Sci.*, 2004, **557**, 269–280.

44 D. Shelton, in *Metallic Films for Electronic, Optical and Magnetic Applications: Structure, Processing and Properties*, Elsevier Ltd., 2013, pp. 547–589.

45 Z. L. Zhang, Y. R. Fang, W. H. Wang, L. Chen and M. T. Sun, Propagating surface plasmon polaritons: Towards applications for remote-excitation surface catalytic reactions, *Adv. Sci.*,

2016, **3**, 1500215.

46 J. M. Brockman, B. P. Nelson and R. M. Corn, Surface plasmon resonance imaging measurements of ultrathin organic films, *Annu. Rev. Phys. Chem.*, 2000, **51**, 41–63.

47 H. Raether, *Surface plasmons on smooth surfaces*, Springer, Berlin, Heidelberg, 1988.

48 S. Kaya, Université de Bourgogne Franche, 2016.

49 E. Kretschmann and H. Raether, *Zeitschrift fur Naturforsch. - Sect. A J. Phys. Sci.*, 1968, 23, 2135–2136.

50 A. Otto, Excitation of nonradiative surface plasma waves in silver by the method of frustrated total reflection, *Zeitschrift für Phys.*, 1968, **216**, 398–410.

51 J. R. Sambles, G. W. Bradbery and F. Yang, Optical excitation of surface plasmons: An introduction, *Contemp. Phys.*, 1991, **32**, 173–183.

52 R. W. Wood, XLII. On a remarkable case of uneven distribution of light in a diffraction grating spectrum , *London, Edinburgh, Dublin Philos. Mag. J. Sci.*, 1902, **4**, 396–402.

53 C. Deeb, C. Ecoffet, R. Bachelot, J. Plain, A. Bouhelier and O. Soppera, Plasmon-based free-radical photopolymerization: Effect of diffusion on nanolithography processes, *J. Am. Chem. Soc.*, 2011, **133**, 10535–10542.

54 R. H. Ritchie, Plasma Losses by Fast Electrons in Thin Films, *Phys. Rev.*, 1957, **106**, 874–881.

55 P. Bharadwaj, B. Deutsch and L. Novotny, Optical Antennas, *Adv. Opt. Photonics*, 2009, **1**, 438.

56 A. Sihvola, Dielectric polarization and particle shape effects, *J. Nanomater.*, 2007, **2007**, 45090.

57 T. Perova, I. Shaganov and K. Berwick, Accounting for the local field when determining the dielectric loss spectra of metals in the region of the frequencies of volume, surface and localized plasmon oscillations, *Materials (Basel).*, 2020, **13**, 631.

58 C. F. Bohren, *Absorption and scattering of light by small particles*, New York: Wiley, 1983.

59 B. Sepúlveda, P. C. Angelomé, L. M. Lechuga and L. M. Liz-Marzán, LSPR-based nanobiosensors, *Nano Today*, 2009, **4**, 244–251.

60 K. A. Willets and R. P. Van Duyne, Localized surface plasmon resonance spectroscopy and sensing, *Annu. Rev. Phys. Chem.*, 2007, **58**, 267–297.

61 M. Sui, S. Kunwar, P. Pandey and J. Lee, Strongly confined localized surface plasmon resonance (LSPR) bands of Pt, AgPt, AgAuPt nanoparticles, *Sci. Rep.*, 2019, **9**, 1–14.

62 S. Szunerits and R. Boukherroub, Sensing using localised surface plasmon resonance sensors, *Chem. Commun.*, 2012, **48**, 8999–9010.

63 M. El barghouti, A. Akjouj and A. Mir, Design of silver nanoparticles with graphene coatings layers used for LSPR biosensor applications, *Vacuum*, 2020, **180**, 109497.

64 C. Wang, X. Feng and P. Chen, LSPR Biosensor Based on Au@Ag Core-Shell Nanobipyramids, *ECS Meet. Abstr.*, 2019, **MA2019-02**, 2291.

65 C. Li, Z. Li, S. Li, Y. Zhang, B. Sun, Y. Yu, H. Ren, S. Jiang and W. Yue, LSPR optical fiber biosensor based on a 3D composite structure of gold nanoparticles and multilayer graphene films, *Opt. Express*, 2020, **28**, 6071.

66 K. Saha, S. S. Agasti, C. Kim, X. Li and V. M. Rotello, Gold nanoparticles in chemical and biological sensing, *Chem. Rev.*, 2012, **112**, 2739–2779.

67 J. S. Sekhon and S. S. Verma, Refractive Index Sensitivity Analysis of Ag, Au, and Cu Nanoparticles, *Plasmonics*, 2011, **6**, 311–317.

68 H. Chen, X. Kou, Z. Yang, W. Ni and J. Wang, Shape- and size-dependent refractive index sensitivity of gold nanoparticles, *Langmuir*, 2008, **24**, 5233–5237.

69 C. Noguez, Surface plasmons on metal nanoparticles: The influence of shape and physical environment, *J. Phys. Chem. C*, 2007, **111**, 3606–3619.

70 S. Link, M. B. Mohamed and M. A. El-Sayed, Simulation of the Optical Absorption Spectra of Gold Nanorods as a Function of Their Aspect Ratio and the Effect of the Medium Dielectric Constant, *J. Phys. Chem. B*, 1999, **103**, 3073–3077.

71 K. S. Lee and M. A. El-Sayed, Gold and silver nanoparticles in sensing and imaging: Sensitivity of plasmon response to size, shape, and metal composition, *J. Phys. Chem. B*, 2006, **110**, 19220–19225.

72 J. L. Hammond, N. Bhalla, S. D. Rafiee and P. Estrela, Localized surface plasmon resonance as a biosensing platform for developing countries, *Biosensors*, 2014, **4**, 172–188.

73 L. S. Jung, C. T. Campbell, T. M. Chinowsky, M. N. Mar and S. S. Yee, Quantitative interpretation of the response of surface plasmon resonance sensors to adsorbed films, *Langmuir*, 1998, **14**, 5636–5648.

74 A. Mooradian, Photoluminescence of metals, *Phys. Rev. Lett.*, 1969, **22**, 185–187.

75 J. Olesiak-Banska, M. Waszkielewicz, P. Obstarczyk and M. Samoc, Two-photon absorption and photoluminescence of colloidal gold nanoparticles and nanoclusters, *Chem. Soc. Rev.*, 2019, **48**, 4087–4117.

76 G. T. Boyd, Z. H. Yu and Y. R. Shen, Photoinduced luminescence from the noble metals and its enhancement on roughened surfaces, *Phys. Rev. B*, 1986, **33**, 7923–7936.

77 Y. Y. Cai, J. G. Liu, L. J. Tauzin, D. Huang, E. Sung, H. Zhang, A. Joplin, W. S. Chang, P.

Nordlander and S. Link, Photoluminescence of Gold Nanorods: Purcell Effect Enhanced Emission from Hot Carriers, *ACS Nano*, 2018, **12**, 976–985.

78 Y. Fang, W. S. Chang, B. Willingham, P. Swanglap, S. Dominguez-Medina and S. Link, Plasmon emission quantum yield of single gold nanorods as a function of aspect ratio, *ACS Nano*, 2012, **6**, 7177–7184.

79 A. Tcherniak, S. Dominguez-Medina, W. S. Chang, P. Swanglap, L. S. Slaughter, C. F. Landes and S. Link, One-photon plasmon luminescence and its application to correlation spectroscopy as a probe for rotational and translational dynamics of gold nanorods, *J. Phys. Chem. C*, 2012, **116**, 13463.

80 G. Lu, L. Hou, T. Zhang, J. Liu, H. Shen, C. Luo and Q. Gong, Plasmonic sensing via photoluminescence of individual gold nanorod, *J. Phys. Chem. C*, 2012, **116**, 25509–25516.

81 M. Fleischmann, P. J. Hendra and A. J. McQuillan, Raman spectra of pyridine adsorbed at a silver electrode, *Chem. Phys. Lett.*, 1974, **26**, 163–166.

82 D. L. Jeanmaire and R. P. Van Duyne, Surface raman spectroelectrochemistry. Part I. Heterocyclic, aromatic, and aliphatic amines adsorbed on the anodized silver electrode, *J. Electroanal. Chem.*, 1977, **84**, 1–20.

83 M. G. Albrecht and J. A. Creighton, Anomalously Intense Raman Spectra of Pyridine at a Silver Electrode, *J. Am. Chem. Soc.*, 1977, **99**, 5215–5217.

84 P. A. Mosier-Boss, Review of SERS substrates for chemical sensing, *Nanomaterials*, 2017, **7**, 142.

85 H. Z. Yu, J. Zhang, H. L. Zhang and Z. F. Liu, Surface-enhanced Raman scattering (SERS) from azobenzene self-assembled “sandwiches,” *Langmuir*, 1999, **15**, 16–19.

86 I. Delfino, A. R. Bizzarri and S. Cannistraro, Time-dependent study of single-molecule SERS signal from yeast cytochrome c, *Chem. Phys.*, 2006, **326**, 356–362.

87 B. Sharma, R. R. Frontiera, A. I. Henry, E. Ringe and R. P. Van Duyne, SERS: Materials, applications, and the future, *Mater. Today*, 2012, **15**, 16–25.

88 G. Mcnay, D. Eustace, W. E. Smith, K. Faulds and D. Graham, Surface-enhanced Raman scattering (SERS) and surface-enhanced resonance raman scattering (SERRS): A review of applications, *Appl. Spectrosc.*, 2011, **65**, 825–837.

89 G. C. Schatz, M. A. Young and R. P. Duyne, in *Surface-Enhanced Raman Scattering*, Springer Berlin Heidelberg, 2006, pp. 19–45.

90 L. Xia, M. Chen, X. Zhao, Z. Zhang, J. Xia, H. Xu and M. Sun, Visualized method of chemical enhancement mechanism on SERS and TERS, *J. Raman Spectrosc.*, 2014, **45**,

533–540.

91 Y. S. Yamamoto and T. Itoh, Why and how do the shapes of surface-enhanced Raman scattering spectra change? Recent progress from mechanistic studies, *J. Raman Spectrosc.*, 2016, **47**, 78–88.

92 L. Jensen, C. M. Aikens and G. C. Schatz, Electronic structure methods for studying surface-enhanced Raman scattering, *Chem. Soc. Rev.*, 2008, **37**, 1061–1073.

93 L. Chen, Y. Gao, Y. Cheng, H. Li, Z. Wang, Z. Li and R. Q. Zhang, Nonresonant chemical mechanism in surface-enhanced Raman scattering of pyridine on M@Au12 clusters, *Nanoscale*, 2016, **8**, 4086–4093.

94 R. Pilot, R. Signorini, C. Durante, L. Orian, M. Bhamidipati and L. Fabris, A review on surface-enhanced Raman scattering, *Biosensors*, 2019, **9**, 57.

95 J. F. Arenas, J. Soto, I. L. Tocón, D. J. Fernández, J. C. Otero and J. I. Marcos, The role of charge-transfer states of the metal-adsorbate complex in surface-enhanced Raman scattering, *J. Chem. Phys.*, 2002, **116**, 7207–7216.

96 S. M. Morton, E. Ewusi-Annan and L. Jensen, Controlling the non-resonant chemical mechanism of SERS using a molecular photoswitch, *Phys. Chem. Chem. Phys.*, 2009, **11**, 7424–7429.

97 V. Amendola, R. Pilot, M. Frasconi, O. M. Maragò and M. A. Iatì, Surface plasmon resonance in gold nanoparticles: A review, *J. Phys. Condens. Matter*, 2017, **29**, 203002.

98 S. Schlücker, Surface-enhanced raman spectroscopy: Concepts and chemical applications, *Angew. Chemie - Int. Ed.*, 2014, **53**, 4756–4795.

99 J. F. Li, Y. J. Zhang, S. Y. Ding, R. Panneerselvam and Z. Q. Tian, Core-shell nanoparticle-enhanced raman spectroscopy, *Chem. Rev.*, 2017, **117**, 5002–5069.

100 S. Y. Ding, E. M. You, Z. Q. Tian and M. Moskovits, Electromagnetic theories of surface-enhanced Raman spectroscopy, *Chem. Soc. Rev.*, 2017, **46**, 4042–4076.

101 P. L. Stiles, J. A. Dieringer, N. C. Shah and R. P. Van Duyne, Surface-Enhanced Raman Spectroscopy, *Annu. Rev. Anal. Chem.*, 2008, **1**, 601–626.

102 H. Zhang, X.-G. Zhang, J. Wei, C. Wang, S. Chen, H.-L. Sun, Y.-H. Wang, B.-H. Chen, Z.-L. Yang, D.-Y. Wu, J.-F. Li and Z.-Q. Tian, Revealing the role of interfacial properties on catalytic behaviors by *in-situ* surface-enhanced Raman spectroscopy, *J. Am. Chem. Soc.*, 2017, jacs.7b04011.

103 H. Wei and H. Xu, Hot spots in different metal nanostructures for plasmon-enhanced Raman spectroscopy, *Nanoscale*, 2013, **5**, 10794–10805.

104 A. B. Zrimsek, N. Chiang, M. Mattei, S. Zaleski, M. O. McAnally, C. T. Chapman, A. I.

Henry, G. C. Schatz and R. P. Van Duyne, Single-Molecule Chemistry with Surface- and Tip-Enhanced Raman Spectroscopy, *Chem. Rev.*, 2017, **117**, 7583–7613.

105 P. H. C. Camargo, L. Au, M. Rycenga, W. Li and Y. Xia, Measuring the SERS enhancement factors of dimers with different structures constructed from silver nanocubes, *Chem. Phys. Lett.*, 2010, **484**, 304–308.

106 P. Verma, Tip-Enhanced Raman Spectroscopy: Technique and Recent Advances, *Chem. Rev.*, 2017, **117**, 6447–6466.

107 J. Wessel, Surface-enhanced optical microscopy, *J. Opt. Soc. Am. B*, 1985, **2**, 1538.

108 J. F. Schultz, S. Mahapatra, L. Li and N. Jiang, The Expanding Frontiers of Tip-Enhanced Raman Spectroscopy, *Appl. Spectrosc.*, 2020, **0**, 1–28.

109 R. M. Stockle, Y. D. Suh, V. Deckert and R. Zenobi, Nanoscale chemical analysis by tip-enhanced Raman spectroscopy, *Chem. Phys. Lett.*, 2000, **318**, 131–136.

110 N. Hayazawa, Y. Inouye, Z. Sekkat and S. Kawata, Metallized tip amplification of near-field Raman scattering, *Opt. Commun.*, 2000, **183**, 333–336.

111 M. S. Anderson, Locally enhanced Raman spectroscopy with an atomic force microscope, *Appl. Phys. Lett.*, 2000, **76**, 3130–3132.

112 B. Pettinger, G. Picardi, R. Schuster and G. Ertl, Surface Enhanced Raman Spectroscopy: Towards Single Molecule Spectroscopy, *Electrochemistry*, 2000, **68**, 912–949.

113 J. Stadler, T. Schmid and R. Zenobi, Developments in and practical guidelines for tip-enhanced Raman spectroscopy, *Nanoscale*, 2012, **4**, 1856–1870.

114 L. T. Nieman, G. M. Krampert and R. E. Martinez, An apertureless near-field scanning optical microscope and its application to surface-enhanced Raman spectroscopy and multiphoton fluorescence imaging, *Rev. Sci. Instrum.*, 2001, **72**, 1691–1699.

115 K. L. A. Chan and S. G. Kazarian, Tip-enhanced Raman mapping with top-illumination AFM, *Nanotechnology*, 2011, **22**, 175701.

116 M. Tang, F. Xianguang, X. Wang, J. He, H. He and X. Hu, Compact integrated optical system for a tip-enhanced Raman spectrometer, *Appl. Opt.*, 2017, **56**, 3639.

117 F. Shao, PhD thesis, ETH Zurich, 2018.

118 W. X. Sun and Z. X. Shen, A Practical Nanoscopic Raman Imaging Technique Realized by Near-Field Enhancement, *Mater. Phys. Mech.*, 2001, **4**, 17–21.

119 C. Debus, M. A. Lieb, A. Drechsler and A. J. Meixner, Probing highly confined optical fields in the focal region of a high NA parabolic mirror with subwavelength spatial resolution, *J. Microsc.*, 2003, **210**, 203–208.

120 M. A. Lieb and A. J. Meixner, A high numerical aperture parabolic mirror as imaging device

for confocal microscopy, *Opt. Express*, 2001, **8**, 458.

121 M. A. Poggi, E. D. Gadsby, L. A. Bottomley, W. P. King, E. Oroudjev and H. Hansma, Scanning probe microscopy, *Anal. Chem.*, 2004, **76**, 3429–3444.

122 G. Seine, R. Coratger, A. Carladous, F. Ajustron, R. Pechou and J. Beauvillain, Tip-to-surface distance variations vs voltage in scanning tunneling microscopy, *Phys. Rev. B - Condens. Matter Mater. Phys.*, 1999, **60**, 11045–11050.

123 C. C. Neacsu, S. Berweger and M. B. Raschke, Tip-enhanced raman imaging and nanospectroscopy: Sensitivity, symmetry, and selection rules, *Nanobiotechnology*, 2007, **3**, 172–196.

124 S. S. Kharintsev, G. G. Hoffmann, P. S. Dorozhkin, G. De With and J. Loos, Atomic force and shear force based tip-enhanced Raman spectroscopy and imaging, *Nanotechnology*, 2007, **18**, 315502.

125 L. Novotny and B. Hecht, *Principles of Nano-Optics*, Cambridge University Press, 2012.

126 T. L. Vasconcelos, B. S. Archanjo, B. S. Oliveira, W. F. Silva, R. S. Alencar, C. Rabelo, C. A. Achete, A. Jorio and L. G. Cancado, Optical Nanoantennas for Tip-Enhanced Raman Spectroscopy, *IEEE J. Sel. Top. Quantum Electron.*, 2021, **27**, 4600411.

127 H. Ehrenreich, H. R. Philipp and B. Segall, Optical properties of aluminum, *Phys. Rev.*, 1963, **132**, 1918–1928.

128 A. D. Rakić, A. B. Djurišić, J. M. Elazar and M. L. Majewski, Optical properties of metallic films for vertical-cavity optoelectronic devices, *Appl. Opt.*, 1998, **37**, 5271.

129 T. X. Huang, S. C. Huang, M. H. Li, Z. C. Zeng, X. Wang and B. Ren, Tip-enhanced Raman spectroscopy: Tip-related issues, *Anal. Bioanal. Chem.*, 2015, **407**, 8177–8195.

130 M. J. Weber, *Handbook of Optical Materials*, CRC Press, 2003.

131 I. Martina, R. Wiesinger and M. Schreiner, Micro-Raman Characterisation of Silver Corrosion Products : Instrumental Set Up and Reference, *e-Preservation Sci.*, 2012, **9**, 1–8.

132 J. D. Scherger, PhD thesis, University of Akron, 2017.

133 J. D. Scherger, E. A. Evans, J. A. Dura and M. D. Foster, Extending nanoscale spectroscopy with titanium nitride probes, *J. Raman Spectrosc.*, 2016, **47**, 1332–1336.

134 J. D. Scherger and M. D. Foster, Tunable, Liquid Resistant Tip Enhanced Raman Spectroscopy Probes: Toward Label-Free Nano-Resolved Imaging of Biological Systems, *Langmuir*, 2017, **33**, 7818–7825.

135 A. Kharitonov and S. Kharintsev, Tunable optical materials for multi-resonant plasmonics: from TiN to TiON [Invited], *Opt. Mater. Express*, 2020, **10**, 513.

136 A. Foti, F. Barreca, E. Fazio, C. D'Andrea, P. Matteini, O. M. Maragò and P. G. Gucciardi, Low cost tips for tip-enhanced Raman spectroscopy fabricated by two-step electrochemical etching of 125 µm diameter gold wires, *Beilstein J. Nanotechnol.*, 2018, **9**, 2718–2729.

137 P. J. Bryant, H. S. Kim, Y. C. Zheng and R. Yang, Technique for shaping scanning tunneling microscope tips, *Rev. Sci. Instrum.*, 1987, **58**, 1115.

138 A. J. Melmed, The art and science and other aspects of making sharp tips, *J. Vac. Sci. Technol. B Microelectron. Nanom. Struct.*, 1991, **9**, 601.

139 J. Plathier, A. Pignolet and A. Ruediger, Note: Controlling the length of plasmonic tips obtained by pulsed electrochemical etching, *Rev. Sci. Instrum.*, 2018, **89**, 096107.

140 A. Amjad, M. Salih and A. S. Sadiq Mayi, Electrochemical Etching Gold Tips, *Tech. Rom. J. Appl. Sci. Technol.*, 2020, **2**, 182–186.

141 M. Li, R. Lv, S. Huang, Y. Dai, Z. Zeng, L. Wang and B. Ren, Electrochemical fabrication of silver tips for tip-enhanced Raman spectroscopy assisted by a machine vision system, *J. Raman Spectrosc.*, 2016, **47**, 808–812.

142 J. S. Lloyd, A. Williams, R. H. Rickman, A. McCowen and P. R. Dunstan, Reproducible electrochemical etching of silver probes with a radius of curvature of 20 nm for tip-enhanced Raman applications, *Appl. Phys. Lett.*, 2011, **99**, 143108.

143 C. Ropers, C. C. Neacsu, T. Elsaesser, M. Albrechty, M. B. Raschke and C. Lienau, Grating-coupling of surface plasmons onto metallic tips: A nanoconfined light source, *Nano Lett.*, 2007, **7**, 2784–2788.

144 M. Asghari-Khiavi, B. R. Wood, P. Hojati-Talemi, A. Downes, D. McNaughton and A. Mechler, Exploring the origin of tip-enhanced Raman scattering; Preparation of efficient TERS probes with high yield, *J. Raman Spectrosc.*, 2012, **43**, 173–180.

145 N. Kumar, B. M. Weckhuysen, A. J. Wain and A. J. Pollard, Nanoscale chemical imaging using tip-enhanced Raman spectroscopy, *Nat. Protoc.*, 2019, **14**, 1169–1193.

146 P. R. Brejna and P. R. Griffiths, Electroless deposition of silver onto silicon as a method of preparation of reproducible surface-enhanced Raman spectroscopy substrates and tip-enhanced raman spectroscopy tips, *Appl. Spectrosc.*, 2010, **64**, 493–499.

147 L. Meng, T. Huang, X. Wang, S. Chen, Z. Yang and B. Ren, Gold-coated AFM tips for tip-enhanced Raman spectroscopy: theoretical calculation and experimental demonstration, *Opt. Express*, 2015, **23**, 13804.

148 I. Maouli, A. Taguchi, Y. Saito, S. Kawata and P. Verma, Optical antennas for tunable enhancement in tip-enhansed Raman spectroscopy imaging, *Appl. Phys. Express*, 2015, **8**, 32401.

149 L. Opilik, Ü. Dogan, J. Szczerbiński and R. Zenobi, Degradation of silver near-field optical probes and its electrochemical reversal, *Appl. Phys. Lett.*, 2015, **107**, 091109.

150 N. Kumar, S. J. Spencer, D. Imbraguglio, A. M. Rossi, A. J. Wain, B. M. Weckhuysen and D. Roy, Extending the plasmonic lifetime of tip-enhanced Raman spectroscopy probes, *Phys. Chem. Chem. Phys.*, 2016, **18**, 13710–13716.

151 L. Opilik, Ü. Dogan, C. Y. Li, B. Stephanidis, J. F. Li and R. Zenobi, Chemical Production of Thin Protective Coatings on Optical Nanotips for Tip-Enhanced Raman Spectroscopy, *J. Phys. Chem. C*, 2016, **120**, 20828–20832.

152 X. Wang, S. C. Huang, T. X. Huang, H. S. Su, J. H. Zhong, Z. C. Zeng, M. H. Li and B. Ren, Tip-enhanced Raman spectroscopy for surfaces and interfaces, *Chem. Soc. Rev.*, 2017, **46**, 4020–4041.

153 N. P. W. Pieczonka and R. F. Aroca, Inherent complexities of trace detection by surface-enhanced Raman scattering, *ChemPhysChem*, 2005, **6**, 2473–2484.

154 G. I. N. Waterhouse, G. A. Bowmaker and J. B. Metson, Oxygen chemisorption on an electrolytic silver catalyst: A combined TPD and Raman spectroscopic study, *Appl. Surf. Sci.*, 2003, **214**, 36–51.

155 I. Martina, R. Wiesinger and M. Schreiner, Micro-Raman investigations of early stage silver corrosion products occurring in sulfur containing atmospheres, *J. Raman Spectrosc.*, 2013, **44**, 770–775.

156 F. Shao and R. Zenobi, Tip-enhanced Raman spectroscopy: principles, practice, and applications to nanospectroscopic imaging of 2D materials, *Anal. Bioanal. Chem.*, 2019, **411**, 37–61.

157 T. Schmid, B. S. Yeo, G. Leong, J. Stadler and R. Zenobi, Performing tip-enhanced Raman spectroscopy in liquids, *J. Raman Spectrosc.*, 2009, **40**, 1392–1399.

158 J. Kalbacova, R. D. Rodriguez, V. Desale, M. Schneider, I. Amin, R. Jordan and D. R. T. Zahn, Chemical stability of plasmon-active silver tips for tip-enhanced Raman spectroscopy, *Nanospectroscopy*, 2015, **1**, 12–18.

159 C. A. Barrios, A. V. Malkovskiy, R. D. Hartschuh, A. M. Kisliuk, A. P. Sokolov and M. D. Foster, in *Chemical, Biological, Radiological, Nuclear, and Explosives (CBRNE) Sensing IX*, eds. A. W. Fountain III and P. J. Gardner, SPIE, 2008, vol. 6954, p. 69540C.

160 J. Szczerbiński, H. Yin, Y.-J. Zhang, F.-L. Zhang, J.-F. Li and R. Zenobi, Preserving Plasmonic Nanostructures from Laser-Induced Deactivation by a Protective Dielectric Shell, *J. Phys. Chem. C*, 2020, **124**, 6385–6394.

161 C. A. Barrios, A. V. Malkovskiy, A. M. Kisliuk, A. P. Sokolov and M. D. Foster, Highly stable,

protected plasmonic nanostructures for tip enhanced Raman spectroscopy, *J. Phys. Chem. C*, 2009, **113**, 8158–8161.

162 R. L. Agapov, A. P. Sokolov and M. D. Foster, Protecting TERS probes from degradation: Extending mechanical and chemical stability, *J. Raman Spectrosc.*, 2013, **44**, 710–716.

163 N. Chiang, X. Chen, G. Goubert, D. V. Chulhai, X. Chen, E. A. Pozzi, N. Jiang, M. C. Hersam, T. Seideman, L. Jensen and R. P. Van Duyne, Conformational Contrast of Surface-Mediated Molecular Switches Yields Ångstrom-Scale Spatial Resolution in Ultrahigh Vacuum Tip-Enhanced Raman Spectroscopy, *Nano Lett.*, 2016, **16**, 7774–7778.

164 E. A. Pozzi, G. Goubert, N. Chiang, N. Jiang, C. T. Chapman, M. O. McAnally, A. I. Henry, T. Seideman, G. C. Schatz, M. C. Hersam and R. P. Van Duyne, Ultrahigh-vacuum tip-enhanced Raman spectroscopy, *Chem. Rev.*, 2017, **117**, 4961–4982.

165 E. A. Pozzi, M. D. Sonntag, N. Jiang, N. Chiang, T. Seideman, M. C. Hersam and R. P. Van Duyne, Ultrahigh vacuum tip-enhanced raman spectroscopy with picosecond excitation, *J. Phys. Chem. Lett.*, 2014, **5**, 2657–2661.

166 K. Fiederling, M. Abasifard, M. Richter, V. Deckert, S. Gräfe and S. Kupfer, The chemical effect goes resonant-a full quantum mechanical approach on TERS, *Nanoscale*, 2020, **12**, 6346–6359.

167 F. Latorre, S. Kupfer, T. Bocklitz, D. Kinzel, S. Trautmann, S. Gräfe and V. Deckert, Spatial resolution of tip-enhanced Raman spectroscopy-DFT assessment of the chemical effect, *Nanoscale*, 2016, **8**, 10229–10239.

168 Y. T. Chen, L. Pan, A. Horneber, M. Van Den Berg, P. Miao, P. Xu, P. M. Adam, A. J. Meixner and D. Zhang, Charge transfer and electromagnetic enhancement processes revealed in the SERS and TERS of a CoPc thin film, *Nanophotonics*, 2019, **8**, 1533–1546.

169 M. Sun, Y. Fang, Z. Yang and H. Xu, Chemical and electromagnetic mechanisms of tip-enhanced Raman scattering, *Phys. Chem. Chem. Phys.*, 2009, **11**, 9412–9419.

170 A. Hartschuh, Tip-enhanced near-field optical microscopy, *Angew. Chemie - Int. Ed.*, 2008, **47**, 8178–8191.

171 P. F. Liao and A. Wokaun, Lightning rod effect in surface enhanced Raman scattering, *J. Chem. Phys.*, 1982, **76**, 751–752.

172 X. Shi, N. Coca-López, J. Janik and A. Hartschuh, Advances in tip-enhanced near-field raman microscopy using nanoantennas, *Chem. Rev.*, 2017, **117**, 4945–4960.

173 Z. Zhang, S. Sheng, R. Wang and M. Sun, Tip-Enhanced Raman Spectroscopy, *Anal. Chem.*, 2016, **88**, 9328–9346.

174 J. Stadler, B. Oswald, T. Schmid and R. Zenobi, Characterizing unusual metal substrates

for gap-mode tip-enhanced Raman spectroscopy, *J. Raman Spectrosc.*, 2013, **44**, 227–233.

175 P. A. Hodgson, Y. Wang, A. A. Mohammad and P. Kruse, Note: Electrochemical etching of silver tips in concentrated sulfuric acid, *Rev. Sci. Instrum.*, 2013, **84**, 026109.

176 M. Li, R. Lv, S. Huang, Y. Dai, Z. Zeng, L. Wang and B. Ren, Electrochemical fabrication of silver tips for tip-enhanced Raman spectroscopy assisted by a machine vision system, *J. Raman Spectrosc.*, 2016, **47**, 808–812.

177 J. Wu and C. C. Lee, Low-pressure solid-state bonding technology using fine-grained silver foils for high-temperature electronics, *J. Mater. Sci.*, 2018, **53**, 2618–2630.

178 G. Kolhatkar, J. Plathier, A. Pignolet and A. Ruediger, Effect of the gold crystallinity on the enhanced luminescence signal of scanning probe tips in apertureless near-field optical microscopy, *Opt. Express*, 2017, **25**, 25929.

179 Y. Wang and X. Chen, Erratum to “Carbon nanotubes: A promising standard for quantitative evaluation of AFM tip apex geometry,” *Ultramicroscopy*, 2012, **115**, 120.

180 F. Zenhausern and B. T. E. N. Heggeler-border, DNA and RNA PolymeraseDNA Complex Imaged by Scanning Force Microscopy : Influence of Molecular-Scale Friction, 1992, **14**, 212–217.

181 B. J. Wiley, Y. Chen, J. M. McLellan, Y. Xiong, Z. Y. Li, D. Ginger and Y. Xia, Synthesis and optical properties of silver nanobars and nanorice, *Nano Lett.*, 2007, **7**, 1032–1036.

182 Y. Fan, D. Jin, X. Wu, H. Fang and X. Yuan, Facilitating hotspot alignment in tip-enhanced raman spectroscopy via the silver photoluminescence of the probe, *Sensors (Switzerland)*, 2020, **20**, 1–13.

183 B. O. Skadtchenko and R. Aroca, Surface-enhanced Raman scattering of p-nitrothiophenol: Molecular vibrations of its silver salt and the surface complex formed on silver islands and colloids, *Spectrochim. Acta - Part A Mol. Biomol. Spectrosc.*, 2001, **57**, 1009–1016.

184 L. K. Yang, Y. Q. Su, X. Y. Wu, D. X. Zhang, Y. L. Chen, F. Z. Yang, D. Y. Wu and Z. Q. Tian, White-light induced grafting of 3-MPA on the Si(111)-H surface for catalyzing Au nanoparticles’ in situ growth, *Nanoscale*, 2015, **7**, 9563–9569.

185 S. S. Kharintsev, G. G. Hoffmann, A. I. Fishman and M. K. Salakhov, Plasmonic optical antenna design for performing tip-enhanced Raman spectroscopy and microscopy, *J. Phys. D. Appl. Phys.*, 2013, **46**, 145501.

186 A. H. Youssef, J. Zhang, A. Dörfler, G. Kolhatkar, A. Merlen and A. Ruediger, Topography-induced variations of localized surface plasmon resonance in tip-enhanced Raman

configuration, *Opt. Express*, 2020, **28**, 14161.

187 M. Nicklaus, G. Kolhatkar, J. Plathier, C. Dab and A. Ruediger, Direct Observation of Core–Shell Structures in Individual Lead Titanate Ferroelectric Nanostructures by Tip-Enhanced Refractive Index Mapping, *Adv. Funct. Mater.*, 2019, **29**, 1806770.

188 G. Kolhatkar, A. Boucherif, C. Dab, S. Fafard, V. Aimez, R. Arès and A. Ruediger, Composition variation in Al-based dilute nitride alloys using apertureless scanning near-field optical microscopy, *Phys. Chem. Chem. Phys.*, 2016, **18**, 30546–30553.

189 B. Pettinger, K. F. Domke, D. Zhang, G. Picardi and R. Schuster, Tip-enhanced Raman scattering: Influence of the tip-surface geometry on optical resonance and enhancement, *Surf. Sci.*, 2009, **603**, 1335–1341.

190 P. Apell, R. Monreal and S. Lundqvist, Photoluminescence of noble metals, *Phys. Scr.*, 1988, **38**, 174–179.

191 M. B. Mohamed, V. Volkov, S. Link and M. A. El-Sayed, The “lightning” gold nanorods: Fluorescence enhancement of over a million compared to the gold metal, *Chem. Phys. Lett.*, 2000, **317**, 517–523.

192 J. Zheng, C. Zhou, M. Yu and J. Liu, Different sized luminescent gold nanoparticles, *Nanoscale*, 2012, **4**, 4073–4083.

193 J. Zhao, A. O. Pinchuk, J. M. McMahon, S. Li, L. K. Ausman, A. L. Atkinson and G. C. Schatz, Methods for describing the electromagnetic properties of silver and gold nanoparticles, *Acc. Chem. Res.*, 2008, **41**, 1710–1720.

194 L. B. Scaffardi and J. O. Tocho, Size dependence of refractive index of gold nanoparticles Related content Size dependence of refractive index of gold nanoparticles, *Nanotechnology*, 2006, **17**, 1309–1315.

195 G. Kolhatkar, J. Plathier and A. Ruediger, Nanoscale investigation of materials, chemical reactions, and biological systems by tip enhanced Raman spectroscopy-a review, *J. Mater. Chem. C*, 2018, **6**, 1307–1319.

196 K. F. Domke, PhD thesis, Fritz Haber Institute of the Max Planck Society, 2006.

197 A. Sacco, D. Imbraguglio, A. M. Giovannozzi, C. Portesi and A. M. Rossi, Development of a candidate reference sample for the characterization of tip-enhanced Raman spectroscopy spatial resolution, *RSC Adv.*, 2018, **8**, 27863–27869.

198 P. R. West, S. Ishii, G. V Naik, N. K. Emani, V. M. Shalaev and A. Boltasseva, Searching for better plasmonic materials, *Laser Photon. Rev.*, 2010, **4**, 795–808.

199 J. A. Faucheaux, A. L. D. Stanton and P. K. Jain, Plasmon resonances of semiconductor nanocrystals: Physical principles and new opportunities, *J. Phys. Chem. Lett.*, 2014, **5**,

976–985.

200 B. S. Yeo, T. Schmid, W. Zhang and R. Zenobi, Towards rapid nanoscale chemical analysis using tip-enhanced Raman spectroscopy with Ag-coated dielectric tips, *Anal. Bioanal. Chem.*, 2007, **387**, 2655–2662.

201 X. Cui, W. Zhang, B.-S. Yeo, R. Zenobi, C. Hafner and D. Erni, Tuning the resonance frequency of Ag-coated dielectric tips, *Opt. Express*, 2007, **15**, 8309.

202 R. J. Hermann and M. J. Gordon, Quantitative comparison of plasmon resonances and field enhancements of near-field optical antennae using FDTD simulations, *Opt. Express*, 2018, **26**, 27668.

203 A. Taguchi, N. Hayazawa, Y. Saito, H. Ishitobi, A. Tarun and S. Kawata, Controlling the plasmon resonance wavelength in metal-coated probe using refractive index modification, *Opt. Express*, 2009, **17**, 6509.

204 T. Skauli, P. S. Kuo, K. L. Vodopyanov, T. J. Pinguet, O. Levi, L. A. Eyres, J. S. Harris, M. M. Fejer, B. Gerard, L. Becouarn and E. Lallier, Improved dispersion relations for GaAs and applications to nonlinear optics, *J. Appl. Phys.*, 2003, **94**, 6447–6455.

205 J. Pastrňák and L. Roskovcová, Refraction Index Measurements on AlN Single Crystals, *Phys. status solidi*, 1966, **14**, K5–K8.

206 W. G. Nilsen and J. G. Skinner, Raman spectrum of strontium titanate, *J. Chem. Phys.*, 1968, **48**, 2240–2248.

207 X. Wang, S. C. Huang, S. Hu, S. Yan and B. Ren, Fundamental understanding and applications of plasmon-enhanced Raman spectroscopy, *Nat. Rev. Phys.*, 2020, **2**, 253–271.

208 C. Blum, L. Opilik, J. M. Atkin, K. Braun, S. B. Kämmer, V. Kravtsov, N. Kumar, S. Lemeshko, J.-F. F. Li, K. Luszcz, T. Maleki, A. J. Meixner, S. Minne, M. B. Raschke, B. Ren, J. Rogalski, D. Roy, B. Stephanidis, X. Wang, D. Zhang, J.-H. H. Zhong and R. Zenobi, Tip-enhanced Raman spectroscopy - An interlaboratory reproducibility and comparison study, *J. Raman Spectrosc.*, 2014, **45**, 22–31.

209 M. Richard-Lacroix, Y. Zhang, Z. Dong and V. Deckert, Mastering high resolution tip-enhanced Raman spectroscopy: towards a shift of perception, *Chem. Soc. Rev.*, 2017, **46**, 3922–3944.

210 J. Plathier, A. Merlen, A. Pignolet and A. Ruediger, Relation between plasmonic tip emission and electromagnetic enhancement evidenced in tip-enhanced Raman spectroscopy, *J. Raman Spectrosc.*, 2017, **48**, 1863–1870.

211 F. Wackenhut, L. A. Jakob, O. Hauler, A. Stuhl, F. Laible, M. Fleischer, K. Braun and A. J.

Meixner, Nanoscale plasmonic phase sensor, *Anal. Bioanal. Chem.*, 2020, **412**, 3405–3411.

212 A. Merlen, J. Plathier and A. Ruediger, A near field optical image of a gold surface: A luminescence study, *Phys. Chem. Chem. Phys.*, 2014, **17**, 21176–21181.

213 M. Nicklaus, PhD thesis, 2013.

214 L. Novotny, in *Progress in Optics*, Elsevier, 2007, vol. 50, pp. 137–184.

215 D. Chapron, F. Cordero and M. D. Fontana, Characterization of oxygen vacancies in $SrTiO_3$ by means of anelastic and Raman spectroscopy, *J. Appl. Phys.*, 2019, **126**, 154101.

216 S. Vedraine, R. Hou, P. R. Norton and F. Lagugné-Labarthet, On the absorption and electromagnetic field spectral shifts in plasmonic nanotriangle arrays, *Opt. Express*, 2014, **22**, 13308.

217 W. S. M. Werner, K. Glantschnig and C. Ambrosch-Draxl, Optical constants and inelastic electron-scattering data for 17 elemental metals, *J. Phys. Chem. Ref. Data*, 2009, **38**, 1013–1092.

218 S. S. Kharintsev, Plasmonic optical antenna design for performing tip-enhanced Raman spectroscopy and microscopy, *J. Phys. D Appl. Phys*, 2013, **46**, 145501.

PUBLICATIONS AND CONFERENCE CONTRIBUTIONS

Publications:

1 **J. Zhang** and A. Ruediger, *In-situ* evaluation of plasmonic enhancement of gold tips for plasmon-enhanced imaging techniques, *Rev. Sci. Instrum.*, 2021, **92**, 053004.

2 **J. Zhang**, G. Kolhatkar and A. Ruediger, Localized surface plasmon resonance shift and its application in scanning near-field optical microscopy, *J. Mater. Chem. C*, 2021, **9**, 6960.

3 **J. Zhang**, A. H. Youssef, A. Dörfler, G. Kolhatkar, A. Merlen and A. Ruediger, Sample induced intensity variations of localized surface plasmon resonance in tip-enhanced Raman spectroscopy, *Opt. Express*, 2020, **28**, 25998.

4 A. H. Youssef, **J. Zhang (co-first)**, A. Dörfler, G. Kolhatkar, A. Merlen and A. Ruediger, Topography- induced variations of localized surface plasmon resonance in tip-enhanced Raman configuration, *Opt. Express*, 2020, **28**, 14161.

5 **J. Zhang**, Y. Gonzalez, R. Sany and A. Ruediger, A facile fabrication procedure for platinum nanoprobes with high-aspect-ratio and low tip radii via electrochemical etching, *Rev. Sci. Instrum.*, 2020, 91, 033702.

6 A. Hadj Youssef, **J. Zhang**, A. Ehteshami, G. Kolhatkar, C. Dab, D. Berthomieu, A. Merlen, F. Légaré and A. Ruediger, Symmetry-Forbidden-Mode Detection in $SrTiO_3$ Nanoislands with Tip-Enhanced Raman Spectroscopy, *J. Phys. Chem. C*, 2021, **125**, 6200–6208.

7 E. Sokullu, M. Pinsard, **J. Zhang**, J. Plathier, G. Kolhatkar, A. S. Blum, F. Légaré, A. Ruediger, T. Ozaki and M. A. Gauthier, Plasmonic Enhancement of Two-Photon Excitation Fluorescence by Colloidal Assemblies of Very Small AuNPs Templated on M13 Phage, *Biomacromolecules*, 2020, **21**, 2705–2713.

8 C. Awada, C. Dab, **J. Zhang** and A. Ruediger, Observation of propagating surface plasmon polaritons by using functionalized tip-enhanced Raman spectroscopy, *J. Raman Spectrosc.*, 2020, **51**, 1270–1277.

9 G. Kolhatkar, A. Merlen, **J. Zhang**, C. Dab, G. Q. Wallace, F. Lagugné-Labarthet and A. Ruediger, Optical near-field mapping of plasmonic nanostructures prepared by nanosphere lithography, *Beilstein J. Nanotechnol.*, 2018, **9**, 1536–1543.

Conference contributions:

1 **J. Zhang**, A. H. Youssef and A. Ruediger. *Tip-Enhanced Refractive Index Mapping of* $SrTiO_3$ *nanostructures*, 7th International Conference on Tip-Enhanced Raman Spectroscopy, 9-12 November 2019, Xiamen, China. (Oral presentation, poster session.)

2 A. H. Youssef, C. Dab, **J. Zhang**, G. Kolhatkar, A. Merlen and A. Ruediger. *IR-active modes detected by tip-enhanced Raman spectroscopy in* $SrTiO_3$ *hetero-epitaxial nanostructures: field gradient or strain gradient contribution?* MRS Fall Meeting, 25-30 November 2018, Boston, Massachusetts.

3 **J. Zhang**, J. Plathier, G. Kolhatkar and A. Ruediger, *Tip-Enhanced Raman Spectroscopy (TERS): Silver Tip Manufacturing*, BIT'S 6th Annual World Congress of Advanced Materials, 14-16 June 2017, Xi'an, China. (Oral presentation, poster session.)

4 **J. Zhang**, J. Plathier, G. Kolhatkar and A. Ruediger, *Silver Tip Manufacturing for Tip-Enhanced Raman Spectroscopy via Electrochemical Etching*, Colloque LN2, 10-13 July 2016, Bromont, Canada. (Poster session.)

5 **J. Zhang**, J. Plathier, G. Kolhatkar and A. Ruediger, *Silver Tip Manufacturing for Tip-Enhanced Raman Spectroscopy via Electrochemical Etching*, Colloque Plasma Québec, 4-6 June 2016, Montréal, Canada. (Poster session.)